Raman Characterization and Applications of Vertical Semiconductor Nanowires

by

Jaspreet Walia

A thesis
presented to the University Of Waterloo
in fulfillment of the
thesis requirement for the degree of
Doctor of Philosophy
In
Electrical and Computer Engineering (Nanotechnology)

Waterloo, Ontario, Canada, 2016

I hereby declare that I am the sole author of this thesis. This is a true copy of the thesis, including any required final revisions, as accepted by my examiners.

Jaspreet

Jaspreet Walia

I understand that my thesis may be made electronically available to the public.

Jaspreet

Jaspreet Walia

Abstract

Vertically oriented nanowires are gaining a considerable amount of attention for a wide variety of applications ranging from lasers to solar cells. Raman spectroscopy has also been developed into a powerful tool which has been used to effectively measure the physical properties of nanowires including crystalline quality, and thermal properties. However, Raman spectroscopy has not widely been applied to study vertically oriented nanowires. In this thesis, it is shown that Raman spectra from vertically oriented nanowires can be used to understand the crystalline quality of the samples, and can also be used to identify the diameter for which the HE_{11} mode is resonantly excited for an incident wavelength of light. In addition to this, Raman spectroscopy was used to estimate the refractive index of the amorphous silicon nanowire samples.

Secondly, enhanced photo-thermal conversion in vertically oriented nanowires is demonstrated. The temperatures are measured using Raman spectroscopy. It is shown that by exciting the HE_{11} mode that temperature increases of 300 K can be achieved for an irradiance of only 10 W/mm^2. Furthermore it is shown that when higher irradiances are used, that GaAs nanowires begin to decompose, resulting in a shell morphology. The concept of photo-thermal heating due to waveguiding was also used to examine how the crystallization process of a-Si nanowires is affected. It was found that depending on the diameter of the nanowire, the crystallization is process is limited. Initial excitation of the HE_{11} mode does not lead to total crystallization due to a rapid loss in the resonance condition.

Lastly, structural colours were observed from nanowire arrays. The colours are used to demonstrate a diffraction based method for measuring nanowire spacing, a linear refractive index sensor, and photo-thermal printing.

Acknowledgements

Firstly, I would like to thank my supervisor, Simarjeet Saini for his support during my studies. I learned many valuable lessons in both engineering and life in general from Professor Saini.

Secondly, I would like to thank Navneet Dhindsa, whom I personally consider a nanowire fabrication expert, for providing me with the vertical nanowire samples. I look forward to enjoying many more collaborations together.

I would also like to very much thank Professor Xiawou (Shirley) Tang for allowing me to use the high resolution Raman spectrometer throughout the course of this thesis.

...to Arjun

For always believing in me

Table of Contents

List of Figures....viii

List of Tables....xvii

List of Abbreviations....xviii

CHAPTER 1: Introduction....1

CHAPTER 2: Raman Scattering in Solids....9

- 2.1 Raman Scattering....11
- 2.2 Semiconductor Crystal Structure....14
- 2.3 Phonons....16
  - 2.3.1 Surface Phonons....21
- 2.4 Selection Rules....24

CHAPTER 3: Experimental Section....30

- 3.1 Nanowire Samples....30
- 3.2 Raman Spectroscopy....33
  - 3.3.1 Confocal Setup....34
  - 3.3.2 Raman Measurements....36

CHAPTER 4: Raman Scattering from Vertical Nanowire Arrays....38

- 4.1 Silicon Nanowires....39
- 4.2 Gallium Arsenide Nanowires....45
- 4.3 Amorphous Silicon Nanowires....58

CHAPTER 5: Photo-Thermal Properties of Vertical GaAs Nanowires....67

- 5.1 Enhanced Photothermal Conversion....68
- 5.2 Photo-Thermal Modification....73
- 5.3 Optimizing Photo-Thermal Conversion....84
  - 5.3.1 Background Physics of Heat Simulations....85
  - 5.3.2 Estimating Thermal Conductivity of GaAs Nanowires....87

5.3.3 Computation Temperature Profiles……………………………………………...90

CHAPTER 6: Laser crystallization of Amorphous Silicon Nanowires.................................99

6.1 Raman Analysis of Materials Consisting of a-Si and c-Si..101

6.1.1 Estimating Crystalline Volume Fraction..101

6.1.2 Estimating Crystallite Size……………………………………………..102

6.2 Raman Spectra of Laser Irradiated a-Si Nanowires……………………………...103

CHAPTER 7: Applications of Structural Color Generation from Nanowire Arrays…….114

7.1 Measurement of Nanowire Pitch and Refractive Index Sensing using Diffraction...115

7.1.1 Diffraction from Periodic Structures……………………………………..116

7.1.2 Experiment Setup for Diffraction Measurements………………………...117

7.1.3 Colour Generation and Measurement of Nanowire Pitch………………...119

7.1.4 Linear Refractive Index Sensing…………………………………………127

7.2 Nanowire Colour Printing……………………..………………………...........134

CHAPTER 8: Summary and Future Work…………………………………………………139

Bibliography……………………………………………………………………………...141

List of Figures

Figure 2.1: Schematic energy level diagram illustrating the transitions involved in the Stokes and anti-Stokes Raman processes……………………………………………………………………12

Figure 2.2: Views of the tetrahedral bonding arrangement in both diamond (left) and zincblende (right) lattices. The diamond lattice can be thought of as a face-centered cubic lattice with a two point basis occupied by identical atoms, whereas the basis is occupied by two different atoms in a zincblende structure…………………………………………………………………...15

Figure 2.3: (a) View of zincblende structure along the <100> directions. The same symmetries apply to the diamond lattice as well. **(b)** View of diamond and zincblende along the [111] and [-1 -11] directions…………………………………………………………………………17

Figure 2.4: Dispersion relation for a monatomic chain with spacing *a*. The group velocity $\partial \omega/\partial k$ vanishes at the boundaries of the zone……………………………………………………………19

Figure 2.5: Phonon dispersion relation for linear chain with a diatomic basis. The effect of two different atoms is that an optical branch is now seen in the dispersion relation. This branch is responsible for the optical behaviour of crystals……………………………………………….21

Figure 2.6: Zincblende GaAs lattice showing the planes which lie perpendicular to the [111] direction. An additional Coulomb restoring force is created during a LO vibration and therefore has a higher energy than the TO vibration. The bonds between the atoms have been removed for clarity……………………………………………………………………………………….26

Figure 2.7: Spectral deconvolution of the Raman spectrum for the 50 nm diameter sample showing both TO and LO scattering centered at 267 cm^{-1} and 291 cm^{-1} respectively. A third peak

corresponding to the surface phonon mode also appears between the TO and LO phonon modes, as discussed in the first chapter. b.) Raman scattering from a bulk [100] GaAs wafer where only LO scattering is allowed and TO scattering is forbidden as expected from the selection rules……28

Figure 3.1: Representative SEM image of an etched Si nanowire array, showing a regular arrangement of vertical 135 nm diameter Si pillars. The scale bar is 1 μm………………………..32

Figure 3.2: SEM image of a square array of 125 nm diameter, 1 μm long GaAs nanowires. The uniform pitch and vertical nature of nanowires are clearly seen. The scale bar is 1 μm…………32

Figure 3.3: SEM image of a-Si nanowires. Since the nanowires are on a glass substrate, charging effects make imaging the array quite difficult. However vertically oriented nanowires can still be made out in the image……………………………………………………………………………33

Figure 3.4: Typical confocal Raman setup. The purpose of the pinhole is to reject scattered light which does not originate from the focal spot of the objective, further reducing stray light. Additionally, a confocal setup can be used to create a Raman image of sample in both the horizontal (x,y) and vertical directions (z)…………………………………………………………..35

Figure 4.1: First order Raman scattering from arrays of vertically etched nanowire arrays. Each sample has a spectrum that is well to fit to Lorentzian line (solid line) with a FWHM of 3.4-3.5 cm^{-1}………………………………………………………………………………………………40

Figure 4.2: Multi-phonon Raman spectrum of etched SiNW for diameters of 30, 33, 39, 42, 47, 56, 60, and 135 nm. The Raman scattering intensity increases monotonically with NW diameter, and the results are plotted on a logarithmic scale for ease of visualization……………………………42

Figure 4.3: Raman spectrum from 135 nm diameter SiNWs (black trace) covering the 50 cm^{-1} to 1150 cm^{1} spectral range. The bulk silicon spectrum (gray) is shown for reference. New spectral features are observed in the low wavenumber region (100 cm^{-1} – 150 cm^{-1}) as well as in the ~ 850 cm^{-1} region…………………………………………………………………………......45

Figure 4.4: Raman spectra covering the 220 cm^{-1} to 305 cm^{-1} spectral range for eight different diameters of GaAs nanowires ranging from 50 to 155 nm. The Raman spectrum from the bulk starting wafer is also shown. For all nanowires, scattering from the LO mode at 291 cm^{-1} and the TO mode centered at 267 cm^{-1} are observed, which are consistent with scattering from the zincblende crystal structure. The SO mode centered at 286 cm^{-1} is also present in all nanowire samples…………………………………………………………………………………...47

Figure 4.5: Spectral deconvolution of the Raman spectrum (dark grey trace) for the 50 nm diameter sample. A good fit (solid black line) is achieved by modeling the LO, TO, and SO modes as independent Lorentzian functions (solid grey lines)……………………………………………...49

Figure 4.6: Peak intensities for LO, TO and SO phonons as the nanowire diameter is changed. A maximum in Raman scattering intensity occurs for the 95 nm diameter sample…………………50

Figure 4.7: TO (a) and LO (b) phonon frequencies versus GaAs nanowire diameter……………..51

Figure 4.8: FWHM for LO and TO phonon Raman lines with changing diameter of nanowires. FWHM of SO phonon was consistently found to be ~ 10 cm^{-1} over the diameters studied……….52

Figure 4.9. Irradiance distribution for three different nanowire diameters of (a) 50 nm, (b) 100 nm, and (c) 150 nm. The distributions were taken at a cross-section 100 nm into the nanowire. (d) Absorptance at a wavelength of 532 nm in nanowires of different diameters. The black squares

represent absorption over a length of 1 μm, while the circles represent absorption within the first 500 nm of the nanowire……………………………………………………………………..54

Figure 4.10: Simulated absorptance for 1 μm long nanowires for different incident wavelengths and diameters. The nanowires were arranged in a square lattice with a pitch of 400 nm. From the contour plot it is seen that larger diameter nanowires (> 150 nm) are more effective at absorbing wavelengths below 500 nm, whereas smaller diameter nanowires are more effective for absorbing wavelengths above 500 nm……………………………………………………………………….55

Figure 4.11: Peak intensities for LO, TO and SO phonons as the nanowire diameter is changed. A maximum in Raman scattering intensity occurs for the 125 nm diameter sample………………...57

Figure 4.12: Raman spectra (gray circles) from a-Si nanowire arrays for diameters ranging from 75 nm to 125 nm and the thin-film starting layer. All spectra are well fit (solid black line) to three peaks representing scattering from the TO (red), LO (green), and LA (blue) phonon modes………………………………………………..……………………………………...59

Figure 4.13: TO phonon intensity per unit volume from a-Si nanowires with diameters ranging from 75 nm to 125 nm. A clear resonant effect is observed for the 85 nm and 120 nm diameter samples. In keeping with the results of our previous studies, these behaviour is the result of resonant excitation of the HE$_{11}$ mode…………………………………………………………….63

Figure 4.14: Resonant diameter which produces the highest optical confinement versus refractive index for incident wavelengths of 533 nm (blue) and 633 nm (black)…………………………….65

Figure 5.1: Measured temperature of the nanowire sidewalls and top facets versus diameter for an input power density of 20 W/mm^2. The temperature was calculated using equation 5.1…………71

Figure 5.2: Time evolution Raman spectra recorded every 5s from vertically oriented, 125 nm diameter GaAs nanowires for an input power density of 20 W/mm^2……………………………..76

Figure 5.3: Time evolution Raman spectra recorded every 5s from vertically oriented, 125 nm diameter GaAs nanowires for an input power density of 40 W/mm^2……………………………77

Figure 5.4: Time evolution Raman spectra recorded every 5s from vertically oriented, 125 nm diameter GaAs nanowires for an input power density of 80 W/mm^2……………………………78

Figure 5.5: Time evolution of the LO phonon peak of c-As. The intensity begins to plateau after ~70 s, with a time constant of ~ 17.2 seconds……………………………………………………..80

Figure 5.6: Raman spectrum taken at a power density of 0.8 W/mm^2 after the sample was exposed to elevated temperatures. Three new peaks corresponding to the TO phonon of c-As at 200 cm^{-1}, the LO phonon of c-As at 258 cm^{-1}, and scattering from a-As centered at 226 cm^{-1} are observed…………………………………………………………………………………….81

Figure 5.7: HAADF image of the FIB-prepared nanowire cross-section. The nanowires are coated in a protective carbon layer as part of the FIB preparation process. Axial and radial EDX line scans, showing the distribution of Ga and As elements, are also shown in the image for one of the altered nanowires. The decomposed structure consists of a hollow Ga-rich nanotube, and an As-rich region. The lower portion of the nanowire remains intact. The nanowire on the far right of the image was outside of the heated area. The scale bar is 125 nm……………………………………83

Figure 5.8: Nanowire geometry and body heat source plots of *Q(x,y,z)*, showing the Gaussian profile in x and y directions, and exponential decay in the z direction……………………………86

Figure 5.9: Simulated top facet temperature of a 130 nm diameter GaAs nanowire for thermal conductivity values ranging from 1-20 $Wm^{-1}K^{-1}$. A value of 6 $Wm^{-1}K^{-1}$ produces the same temperature as the Raman experiment (570 K)…………………………………………………...88

Figure 5.10: TEM image of a GaAs nanowire showing sidewalls which have undulations on the order of 1 nm………………………………………………………………………………..90

Figure 5.11: Temperature distribution of Si and GaAs nanowire for the same incident energy and resonant conditions. The order magnitude difference of the absorption coefficients and thermal conductivites of the materials are the reason for huge differences in temperature………………..91

Figure 5.12: Simulated top facet temperatures of a 1 µm long GaAs and Si nanowire versus incident laser power density (solid black lines). The dots represent the experimentally determined top facet temperatures for a 1 µm long GaAs nanowire. There is a reasonably good agreement between the experiments and simulations……………………………………………………...93

Figure 5.13: Temperature distribution of a GaAs and Si nanowire for two different input powers of 40 W/mm^2 and 1.52 kW/mm^2, respectively. Even though the nanowires have the same temperature difference across their lengths, different temperature profiles are still observed……94

Figure 5.14: Contour plot for the top facet temperature of a 1 µm long, 130 nm diameter nanowire for different of α and κ, and an input power density of 40 W/mm^2. Regardless of the value of α, a reduction in κ leads to an increased top facet temperature. On the other hand, the same optimal value for α leads to the maximum top facet temperature for every value of κ……………………..96

Figure 5.15: Contour plot for the top facet temperature of a 1 μm long, 130 nm diameter nanowire for different of α and nanowire length, L, and an input power density of 40 W/mm^2. For a given nanowire length, there is an optimal value for α that produces the maximum nanowire temperature……………………………………………………………………………………97

Figure 6.1: Raman scattering from a-Si nanowire arrays after exposure to an irradiance of 480 W/mm^2 to promote crystallization. Clear spectral differences are seen relative to Figure 4.10…104

Figure 6.2: Normalized Raman spectra from all of the nanowire samples. Different degrees of crystallinity are observed. As the diameter of the nanowire increases, the amorphous signatures begin to diminish……………………………………………………………………………..105

Figure 6.3: Stack plot of all Raman spectra taken showing the emergence of two distinct spectral features at ~ 300 cm^{-1} and ~ 500 cm^{-1} - 510 cm^{-1}……………………………………………...106

Figure 6.4: Representative fits for 75 nm, 80 nm, 100 nm, and 125 nm diameter nanowires……109

Figure 6.5: FWHM of the 520 cm^{-1} peak of c-Si. The 85 nm diameter sample exhibits the smallest linewidth, and therefore the highest quality silicon crystals……………………………………110

Figure 6.6: RIV for the c-Si phonon peak at 520 cm^{-1}, as well as the RIV for the TO phonon frequency of a-Si at 480 cm^{-1} for all diameters…………………………………………………112

Figure 7.1: Geometric illustration of the diffraction effect, and the variables appearing in equation 7.1……………………………………………………………………………………………….116

Figure 7.2: Diagram of the experimental setup to observe and measure diffracted colours from silicon nanowire arrays………………………………………………………………………….118

Figure 7.3: Brightfield images of SiNW arrays, with lattice spacing varying from 200 nm to 1700 nm. Vivid colour are observed especially for lattices with smaller spacing, where resonant coupling becomes important……………………………………........………………………………...120

Figure 7.4: Colour generation from SiNWs with lattice spacing ranging from 600 nm to 1300 nm when imaged with a white LED light source incident at a grazing angle. Vivid primary colours are observed, which so far, have been difficult to generate in a bright field setup…………………...121

Figure 7.5: Spectral measurement of diffracted wavelengths for three different lattice spacings of 600 nm (blue), 700 nm (green) , and 800 nm (oranges) for an incident angle of 50°. All spectra have been normalized to unity intensity……………………………………………………………124

Figure 7.6: Diffracted colour vs incident angles of 35°, 50°, and 60° from a SiNW array with a 700 nm lattice spacing. All three RGB primaries are easily generated and are understood using Bragg theory………………………………………………………………………………………...125

Figure 7.7: Diffracted colour vs SiNW diameter for a constant lattice spacing of 600 nm, for different diameters of 80 nm and 200 nm. The same hue (colour) is observed in both cases, supporting the Bragg interpretation for colour generation in the current experimental setup, this is not the case for nanowires illuminated in a bright field configuration…………………………..125

Figure 7.8: Two orientations of SiNW nanowire arrays with respect to the incident beam (45° and 90°). For 45°, a new set of Bragg planes emerges, resulting a √2 decrease in the lattice spacing as compared to the case where light is incident normal to the array edge, and thus different colours can be generated from the arrays in this fashion as well………………………………………126

Figure 7.9: Comparison between the experimental RGB (a) and HSL(b) values, and theoretical values predicted (solid lines) by the design, and (c) the experimentally observed colour versus the colours that were expected to be seen…………………………………………………………...132

Figure 7.10: A spectral measurement for two different refractive index fluids of 1.300 (open red circles) and 1.305 (open blue circles). Air is shown for reference (open black circles) as well as the fits to the data (solid lines)………………………………………………………………..133

Figure 7.11 A brightfield image of the GaAs nanowire array showing the demonstrating photo-thermal laser printing at 10000 DPI. An SEM image of a section of the modified area is also shown………………………………………………………………………………………...136

Figure 7.12 The letters UW written into an a-Si nanowire array using a laser. The dots consist of c-Si and were realized using photo-thermal modification as discussed in Chapter 6……………136

Figure 7.13 A higher magnification SEM image of the edge of the modified nanowires from Figure 7.11………………………………………………………………………………………...137

List of Tables

Table 3.1: Gas mixtures and pressures used for etching the various semiconductor materials to form nanowires………………………………………………………………………….31

Table 3.2: Specifications for various components in the Raman spectrometer. These values were used for all experiments appearing in the thesis…………………………………………………36

Table 4.1: Measurement parameters used to acquire Raman spectra from Si nanowire..............40

Table 4.2: Measurement parameters used to acquire Raman spectra from GaAs nanowires…....48

Table 4.3: Measurement parameters used to acquire Raman spectra from a-Si nanowires……..59

Table 4.4: Values for the FWHM, centre frequency, and RIV of the TO mode from a-Si nanowires…………………………………………………………………………………...60

Table 5.1: Measurement parameters used to acquire Raman spectra from GaAs nanowires for the purposes of understanding their photo-thermal properties………………………………………70

Table 6.1: Measurement parameters used to acquire Raman spectra from a-Si nanowires that were crystallized……………………………………………………………………………..104

Table 6.2: Calculated crystalline volume fractions of c-Si and poly-Si after irradiation of the nanowire samples. The fractions were calculated using equation 6.1………………………….108

Table 7.1: Measured diffracted wavelengths versus lattice spacing……………………………122

List of Abbreviations

aSi	Amorphous Silicon
Al	Aluminum
As	Arsenic
a-As	Amorphous Arsenic
c-As	Crystalline Arsenic
C	Carbon
Cl	Chlorine
Cr	Chromium
CCD	Charge Coupled Device
EDX	Energy Dispersive X-Ray
F	Fluorine
GaAs	Gallium Arsenide
H	Hydrogen
HAADF	High Angle Annular Dark Field
ICP	Inductively Coupled Plasma
IPA	Isopropyl Alcohol
MIBK	methyl isobutal ketone
N	Nitrogen
N.A.	Numerical Aperture
NW	Nanowire
PMMA	Poly(methyl methacrylate)
RIE	Reactive Ion Etching
S	Sulfur
SEM	Scanning Electron Microscope
Si	Silicon
TEM	Tunneling Electron Microscope

CHAPTER 1

Introduction

Nanotechnology is enabling very fine control over the size and shape of semiconducting materials. These materials at the nanoscale exhibit many different properties than their bulk counterparts. The large surface to volume ratios that are created inherently produce larger surface state populations, and when the dimensions approach the Bohr exciton length scales, quantum confinement effects become quite significant. In this study, focus is given to semiconductor nanowires. Due to their ability to effectively confine carriers and photons in two directions and propagate in the third, nanowires are particularly attractive for opto-electronic applications. The increased absorption and resonant waveguiding properties of nanowires are attracting ever increasing attention for a wide variety of applications including lasers [1, 2], solar cells [3-6], structural color generation [7-9], imagers [10], and sensors [11-13]. Specifically, vertically oriented nanowire arrays are known to have markedly increased optical absorption due to resonant coupling into optical modes [20]. Nanowires also behave as efficient thermoelectric materials [15-18]. Semiconductor nanowires are known to have thermal conductivities which are dominated by phonon processes, as opposed to electronic processes, which make them an attractive choice for thermoelectric devices [19-22]. For example, GaAs in its bulk form has a bulk thermal conductivity of 54 $Wm^{-1}K^{-1}$, whereas GaAs nanowires have been reported to have thermal conductivity ranging from 8-36 $Wm^{-1}K^{-1}$ [18]. Silicon nanowires have shown a 100-fold increase in ZT values over bulk silicon [15-17]. Computer simulations have also suggested that the thermal conductivity of nanowires can be further reduced by creating nanowires with rough surfaces [23]. The thermal conductivity of GaAs is naturally lower than Si, making it an attractive material choice for nanowire based PTE applications. In order to fully realize the potential of various nanowire systems, one must understand how the length and diameter affect the physical properties of the nanowires themselves. Furthermore, nanowires which are arranged into various lattices may have properties which are dependent on the collective nature of the array. To this end, optical characterization of semiconducting nanowires has proven to be a powerful tool, but is still in its infancy.

With these wide range of applications, it is imminent that commercial applications would be developed in the near future. Thus, characterization of nanowires becomes crucial. TEM measurements are generally used to confirm crystalline structure of NWs, and has been used in a study to confirm the presence of various silicon polymorphs in single nanowires [10]. Even though these modalities provide the information required, they cannot probe a large area of nanowires at once. Furthermore, nanowires which are fabricated as photonic lattices would have to be broken off the substrate for TEM characterization. Thus developing non-destructive rapid in-line characterization tools is essential if nanowires structures and devices are going to be integrated into everyday devices. A wide range of properties need to be characterized from the diameter of the wires, to the crystalline structure. Nanowire diameters are typically measured using electron microscopy, which is costly and very inefficient. Along the same lines, TEM measurements are generally used to investigate the crystalline nature of nanowires.

Raman spectroscopy is becoming increasingly popular for the study of semiconductor nanowires. In this connection several new phenomena have been elucidated from Raman scattering spectra. Firstly, the high surface to volume ratios have allowed for the measurement of surface phonon modes [24, 25]. The position of the surface phonon peak was found to vary with diameter, as well as with the dielectric constant of the medium surrounding the nanowires. Some authors, including our group, have even reported enhanced Raman scattering intensities from nanowires. The increased intensities result from the dielectric mismatches at the air-nanowire interfaces, and it was recently shown that vertically oriented nanowires provide a further increase in Raman scattering intensity [26,27]. The increases result from the fact that vertically oriented nanowires act like dielectric waveguides which efficiently couple light into the semiconductor volume. We recently showed that highly enhanced Raman scattering from vertically oriented silicon nanowires, arranged in square lattices, can be realized through proper choice of lattice spacing (pitch) and diameter of the wires [26, 27]. Thus, Raman scattering can provide information about the electromagnetic interactions occurring in the nanowire array. Experimental Raman scattering studies on nanowires also show phonon confinement effect in nanowires with diameters less then 25 nm [28]. Raman line shapes from silicon nanowires displayed significant broadening and redshifts with respect to their bulk counterparts. Phonon confinement is well understood in terms of the RCF (named after the authors Richter, Campbell and Fauchet) model [29, 30]. Some debate remains over its validity since a spectral redshift of at most only 1 cm^{-1} is predicted for the first-order mode centered at 520 cm^{-1}, whereas shifts of 10-20 cm^{-1} have been reported in NWs which are larger than 20 nm in diameter [31-33]. Generally, it is accepted that only nanowires with diameters below 20 nm experience quantum confinement effects [28].

In this work, micro-Raman spectroscopy was used to investigate the vibrational properties of silicon (Si), gallium arsenide (GaAs), and amorphous silicon (a-Si) nanowire arrays. It is shown that micro-Raman spectroscopy can be used to rapidly verify the crystalline quality of nanowires, and can also be used to further understand the electromagnetic coupling properties of nanowires arranged into lattices, as well as the thermal properties of nanowire arrays. It is also shown that the refractive index of a-Si nanowires can be correlated to average Si-Si-Si bond angle variation.

During the investigation of GaAs nanowire Raman spectra, another derivative research was proposed. The photo-thermal properties of vertically etched gallium arsenide nanowire arrays are examined using Raman spectroscopy. Square lattices of nanowires with a constant pitch of 400 nm, and diameters ranging from 50 to 155 nm, were illuminated using a 532 nm laser at an incident energy density of 10 W/mm^2. Nanowire temperatures were highly dependent on the nanowire diameter, and were determined by measuring the spectral redshift for both TO and LO phonons. The highest temperatures were observed for 95 nm diameter nanowires, whose top facets and sidewalls heated up to 600 K and 440 K, respectively, and decreased significantly for the smaller or larger diameters studied. The diameter-dependent heating is explained by resonant coupling of the incident laser light into optical modes of the nanowires, resulting in increased absorption. Photo-thermal activity in a given nanowire diameter can be optimized by proper wavelength selection, as confirmed using computer simulations. This demonstrates that the photo-thermal properties of GaAs nanowires can be enhanced and tuned by using a photonic lattice structure, and smaller nanowire diameters are not necessarily better to achieve efficient photo-thermal conversion. The diameter and wavelength dependence of the optical coupling could allow for localized temperature gradients by creating arrays which consist of different diameters.

This work was further extended to study resonant photo-thermal modification of vertically arranged zincblende (ZB) GaAs nanowires using Raman spectroscopy. The diameter which enables the strongest excitation of the HE_{11} mode was found to be 125 nm, and was identified by measuring the spectral shift of the transverse optical (TO) phonon mode of the GaAs nanowire samples with diameters ranging from 80 nm to 200 nm. It is instructive to note that the resonant diameter which produces the strongest excitation is strictly dependant on the incident wavelength [17, 22]. At resonance, the temperature of the nanowire sample was found to vary nearly linearly with input power. Additionally, it was observed that power densities of only 20 W/mm^2, and resulting temperatures of only 440 K, were sufficient to induce the onset of arsenic formation in vertically oriented GaAs nanowires, demonstrating that photo-thermal degradation due to resonant waveguiding lowers the threshold power density which a vertical GaAs nanowire can support. To observe the degradation of the nanowires directly, a focused ion beam (FIB) was used to mill the nanowires along the axial direction for observation by high angular annular dark field (HAADF) transmission electron microscopy combined with energy dispersive x-ray (EDX) spectroscopy. The HAADF images and EDX analysis clearly show the structural changes associated with laser heating, and demonstrate for the first time that, depending on the incident power, heating due to waveguiding results in vertical hollow gallium oxide nanowires, or an As-Ga core shell structure. These findings provide valuable information for scientific investigations and engineering applications of GaAs nanowires, and can be extended to other compound semiconductors, such as InAs and InP, where structural decomposition also can occur. The ability to alter the physical nature of GaAs nanowires using resonant photo-thermal modification can be used to realize new functional properties, and may give rise to new physics and devices.

The concept of heating due to resonant excitation was used to realize vertical silicon nanowire arrays from amorphous silicon nanowire arrays. It is well known that amorphous silicon can be converted to its crystalline form using heat. The crystalline quality, and crystalline volume fraction was examined once again using Raman spectroscopy, for nanowire diameters ranging from 75 nm to 125 nm. Interestingly, it was observed that smaller diameter nanowires are limited to how much crystalline silicon will form, whereas diameters above 95 nm had nearly all of their amorphous component modified. However, it was observed that the 85 nm diameter produced the highest quality silicon crystals. These results were readily understood in terms of the shift in resonance for the HE_{11} mode. Specifically, as the material crystallizes, its refractive index changes towards the value of Si, and depending on the diameter involved, the local temperature may rise or drop as crystallization proceeds. For a-Si, the resonant diameter is 85 nm, and for c-Si it is 100 nm for an incoming wavelength of 533 nm. In this connection, as the 85 nm diameter crystallizes, the local temperature drops. In fact, crystallization is known to occur on the nanosecond time scale [34]. On the other hand, as the 100 nm diameter begins to crystallize, it resonates more with the incoming light field, and therefore the local temperature is at least maintained, allowing for crystallization to proceed over a much longer timescale, and accounts for the increased c-Si volume fractions.

Lastly, while performing the Raman experiments, it was observed that all nanowire arrays generate structural colours that depend on the lattice geometry. Along these lines, it is shown that the pitch of nanowire arrays can be simply determined by using diffractive techniques, and without the need for a spectrometer. This idea was extended to realize a colourimetric refractive index sensor. Vivid colours spanning from bright red to blue are easily achieved. In keeping with this, a single square lattice of silicon nanowires is also able to produce different colours spanning the entire visible range. It is also shown that the 2-D gratings also have a third grating direction when rotated 45 degrees. These simple and elegant solutions to colour generation from silicon are used to demonstrate a cost-effective refractive index sensor. The sensor works by measuring colour changes resulting from changes in the refractive index of the medium surrounding the nanowires using a trichromatic RGB decomposition. Moreover, the sensor produces linear responses in the trichromatic decomposition values versus the surrounding medium index. A refractive index resolution of 10^{-4} was achieved by performing basic image processing on the collected images, without the need for a laser or a spectrometer. Spectral analysis enables an increase in the index resolution of the sensor to a 10^{-6}, with a sensitivity of 400 nm/RIU. This is nearly four times the resolution of silicon photonic integrated ring resonators, and two times larger than slot waveguide based sensors, and can be achieved without any significant optical alignment.

Lastly, the optical changes resulting from the photo-thermal modification of nanowire arrays are readily seen in brightfield. The colours generated by the nanowires are modified within the focal spot of the laser. In this connection it is shown that a simple microscope image can be used to determine whether or not any physical changes have occurred from laser irradiation. Futhermore, the modified region is essentially limited to focal spot of the laser, allowing for the potential to realize nanowire photo-thermal laser printing through spatial tuning of the optical properties of a nanowire array. One recent study has shown that photo-thermal melting of plasmonic nanostructures can be used to realize a 125000 DPI colour laser printer [35]. Here, photo-thermal printing at 50000 DPI is demonstrated using a 20 X lens, in both GaAs and a-Si nanowire arrays. In this case, the nanowires maintain their vertical nature, and do not melt. Additionally, since the nanowires arrays consist of semiconductor material, Raman analysis of the structural modification becomes possible, allowing for an overall understanding of the process. It is unlikely that decomposed GaAs nanowires will find a useful application, other than laser printing. This is not the case for a-Si nanowires. Both vertical c-Si and a-Si nanostructures are heavily researched for their optical absorption characteristics for next generation solar cells. More recently, researchers are interested in colourful solar cells for aesthetically pleasing solutions. In this connection, photo-thermal printing of a-Si nanowire arrays allows for c-Si and a-Si nanowires, on the same substrate, with minimal fabrication steps. More generally, the fact that the vertical nature is maintained is attractive for researchers looking to make use of the any properties of both c-Si and a-Si on the same substrate.

The following chapter provides a background on Raman scattering from semiconductor crystals. Focus given to the diamond and zincblende crystal structures and the propagation of phonons, and surface phonons. The Raman selection rules are also introduced, with specific attention given to diamond and zinc-blende structures. Chapter 3 briefly discusses nanowire sample fabrication, and the experimental details of the Raman scattering measurements. Raman scattering results from vertical Si, GaAs, and a-Si nanowires are presented in Chapter 4. Chapter 5 dicusses enhanced photo-thermal conversion from GaAs nanowires, and structural modification of GaAs nanowires due to resonant heating is presented and understood. Some of the experimental conclusions regarding heating in vertical nanowires are supported using finite element method (FEM) computer simulations, and Chapter 5 also briefly introduces the background physics associated with these calculations/simulations. Chapter 6 investigates the photo-thermal conversion of amorphous silicon nanowires into silicon nanowires. Specifically, the crystalline quality of the resulting nanowires is examined using Raman spectroscopy, and the results are compared to the high quality single crystal nanowires presented in chapter 5. Chapter 7 demonstrates how simple brightfield images can be used to discern the pitch and diameter of vertical nanowire samples, and how a simple refractive index sensor is realized from such a technique. Additionally, spatial photo-thermal tuning of the optical properties of GaAs and a-Si nanowires in Chapter 7. Lastly, Chapter 8 summarizes the findings, and directions for future work are discussed.

CHAPTER 2

Raman Scattering in Solids

Introduction

Raman scattering is an extremely powerful spectroscopic technique that is able to probe phonons in semiconductor materials. Raman scattering is an inelastic light scattering process which mainly probes phonon modes arising at the Γ point in the first Brillouin zone of crystals. With the use of a confocal microscope, it is possible to obtain sub-micron resolutions of material properties. Raman spectroscopy has become a standard tool for the characterization of a wide variety of materials and provides information about crystal structure, phonon modes, plasmons, stress/strain, and thermal properties.

Generally, crystal systems exhibit very sharp Lorentzian lines in their Raman spectra ~3-4 cm^{-1}, centered at the various Transverse Optical (TO) and Longitudinal Optical (LO) phonon frequencies of the material system in question. This spectral signature can be readily used to confirm that long-range crystalline order is present in semiconductor material systems. Amorphous materials are characterized by their lack of crystalline order, and therefore exhibit very broad Raman signatures ~ 100 cm^{-1}. Polycrystalline materials can exhibit both amorphous and crystalline signatures in their Raman spectra depending on the grain sizes. In some cases, it is possible to extract the amount of crystalline and amorphous material present. This is discussed in more detail in the chapter the follows where it will be shown that the amounts of amorphous silicon (a-Si) and crystalline silicon c-Si in nanowires can be determined. In keeping with this, deviations in spectral lineshapes also provide valuable information on what is happening inside the crystal lattice.

Phonon frequencies are sensitive to local temperature, and are shifted to higher energies as the temperature increases. The relationships which describe phonon frequency shifts as a function of temperature are beyond the scope of this work, and are rarely used to determine the actual temperature. Interestingly, Raman scattering can be used to determine the temperature of samples. The temperature is proportional to the Stokes and anti-Stokes scattering intensities. Besides shifting phonon frequencies to higher energies, increased temperatures also induce line broadening in Raman spectra. Strains that are present in the lattice also have the effect of shifting phonon frequencies to different values. Compressive and tensile strains cause phonon frequencies to decrease and increase in energy respectively, and are therefore easily probed using the Raman technique. In general, even though the theoretical aspects describing the changes in phonon frequencies are quite involved, experimental Raman spectroscopy is easily is able to provide direct information on these aspects. Another area in which Raman spectroscopy is a powerful tool is for the detection of surface phonons. Normally, surface phonons are observed when the translational symmetry of the surface is broken. This can result in the activation of large wave vector surface mode whose vibrational frequency is sufficiently separated in the first-order spectrum, and thus detected experimentally.

Recently, Raman spectroscopy has been applied to the study of semiconductor nanowires, where some new physics has been observed. For example, spectral features associated surface phonon modes have been observed, and have been attributed to the increased surface to volumes ratios inherently present in these structures [24]. Additionally, increased Raman scattering intensities from nanowires relative to their bulk counterparts have been observed, which results from the efficient coupling of incident light field into the nanowire core [26,27]. Lastly, decreases in the thermal conductivity of nanowires have been successfully measured using Raman spectroscopy.

As semiconductor nanostructures become more important and reach the device level, the ability to characterize them using a non-destructive technique becomes equally important. In this connection, Raman scattering is an essential tool which can be used to understand the underlying physics of materials at the nanoscale.

In order to be able to quantify and understand Raman spectra from semiconductor nanowires properly, and how their spectra are different from bulk (or not), requires a basic understanding of the Raman scattering process, crystal structure, and selection rules. Specifically, it is important to understand the origins of the peaks in crystal systems so the origins of the deviations which might appear can be understood. Otherwise one is simply limited to seeing changes in peaks without any insight into the origins of these changes. Along these lines, it is particularly important to understand phonons and their origins, and the nomenclature generally associated with crystalline materials.

2.1 Raman Scattering

The Raman process involves the interaction of incoming electromagnetic radiation with the vibrational states of a material. Since momentum must be conserved, any energy that is lost/gained by the photon must be accompanied by a gain or loss of vibrational or rotational energy of the system. Figure 2.1 shows a schematic energy level diagram of the Raman process. Specfically the Raman process involves the absorption of an incident photon with energy $\hbar\omega_i$ and wavevector $\mathbf{k_i}$, which excites the system, initially in an energy state E_1 to a virtual state. Instantaneously, the system relaxes to a state E_2 and emits a photon with energy $\hbar\omega_f = \hbar\omega_i + (E_1 - E_2)$ and wavevector $\mathbf{k_f}$. This is different to fluorescence, where the excited stated are electronic states and are long lived

(~ns). When the initial and final states are equal ($E_1 = E_2$), we have Rayleigh scattering. Stokes scattering occurs when excited systems relax back to higher energy states, and anti-Stokes scattering occurs for systems which relax back to lower energy states. Thus for Stokes and anti-Stokes processes, the energies of the emitted photons are shifted by a fixed amount, independent of the incoming photon energy. This is known as the Raman shift, and is usually measured in units of cm^{-1}. Along these lines, Raman spectra provide direct information on differences in the vibrational energy states of the system.

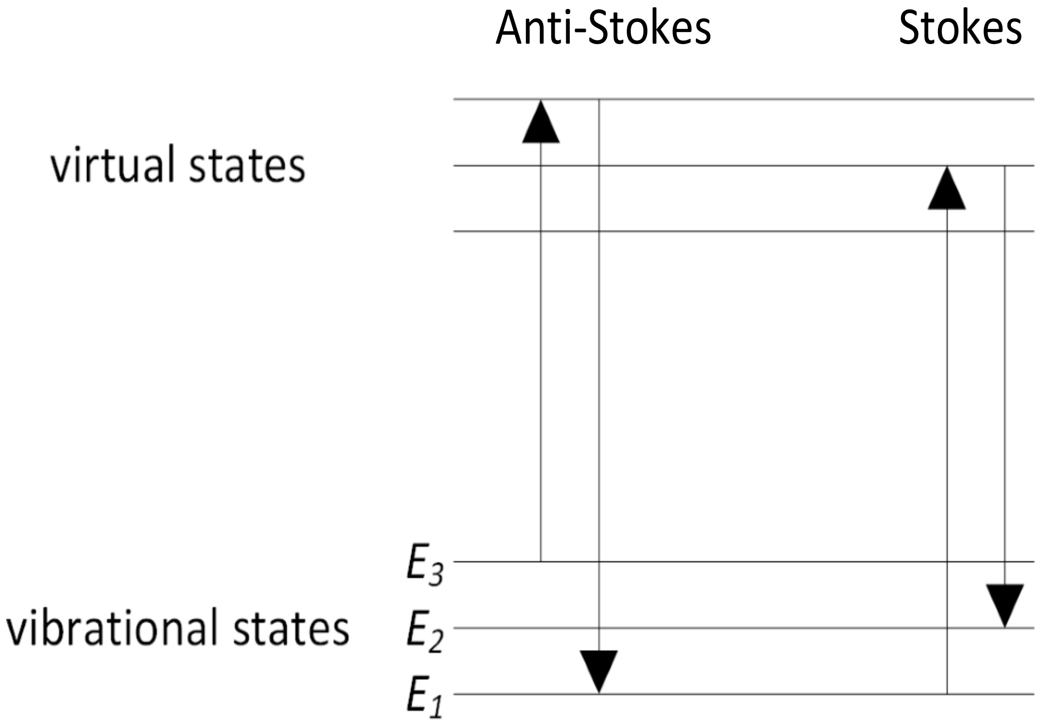

Figure 2.1: Schematic energy level diagram illustrating the transitions involved in the Stokes and anti-Stokes Raman processes.

What follows is a description of the Raman effect from a classical point of view. In this case, the degree of polarization is at the heart of the Raman effect. The electric field generated, at a point ***r*** in a transparent crystal, by a plane monochromatic wave is given by

$$\mathbf{E} = \mathbf{E_0}\cos(\omega_0 t) \qquad 2.1$$

The oscillating electric field causes an induced dipole moment

$$\mathbf{P} = \alpha\mathbf{E_0}\cos(\omega_0 t) \qquad 2.2$$

where α represents the polarizability and is a 3x3 tensor. All elements of the tensor are real unless magnetic interactions occur. Furthermore the symmetry of the crystal determines the form of the tensor. The time dependance of $\boldsymbol{\mu}$ and **E** implies that the dipole is oscillating in time, and therefore will radiate energy. The polarizability can be expanded using a Taylor series in normal coordinates. The normal mode of vibration is defined by

$$\mathrm{U_i} = \mathrm{U_i^0}\cos(\omega_i t) \qquad 2.3$$

where ω_i is the angular frequency for the i^{th} normal mode. Expanding **P** using a Taylor yields

$$\mathbf{P} = \alpha_0\mathbf{E_0}\cos(\omega_0 t) + \frac{1}{2}\left(\frac{\partial\alpha}{\partial \mathrm{U_i}}\right)\mathbf{E_0}\mathrm{U_i^0}\big[[\cos(\omega_0 + \omega_i)t + \cos(\omega_0 - \omega_i)t\big] \qquad 2.4$$

Here the first term represents Rayleigh scattering and the last two terms represent the Stokes and anti-Stokes respectively. Upon inspection, we see that $\left(\frac{\partial\alpha}{\partial \mathrm{U_i}}\right) \neq 0$ for Raman scattering to occur. In other words, there must a non-zero change in polarizability associated with the vibrational mode to observe Raman spectra.

2.2 Semiconductor Crystal Structure

Since Raman scattering ultimately involves phonons when dealing with crystals, it is important to understand the underlying crystal structure(s) of semiconductor materials, and the propagation of phonons within them. We are ultimately concerned with understanding Raman spectra from semiconductor nanowires We will focus our attention to first understanding the diamond and zinc-blende crystal structures. The elemental semiconductors, Si, and Ge crystallize into diamond structures, and the compound semiconductors such as GaAs, GaP, InAs, InP, AlAs, AlP, GaSb, InSb stabilize into the zincblende (ZB) structure. The tetrahedral bonding structure of diamond is shown in Figure 2.2a. This is known as a diamond lattice, and can actually be considered as a face-centered cubic (fcc) lattice with a two point basis. The zincblende structure consists of two different atoms distributed on a diamond lattice. As an example, the zincblende structure of GaAs is shown in Figure 2.2b. The diamond nature of this structure is clearly seen. In the zincblende structure, the two point basis is occupied by two different atoms.

Lattice planes and directions are usually defined in terms of their Miller indices. The Miller indices are the coordinates of the vector which is normal to the plane. When considering the real space lattice, square brackets are used. For discussions involving the reciprocal lattice, round brackets are used to denote various planes and directions. For cubic systems, the reciprocal lattices are also cubic. Therefore, the Miller indices can be represented by either round or square brackets, and only non-cubic systems one needs to remember the difference. Families of planes which are

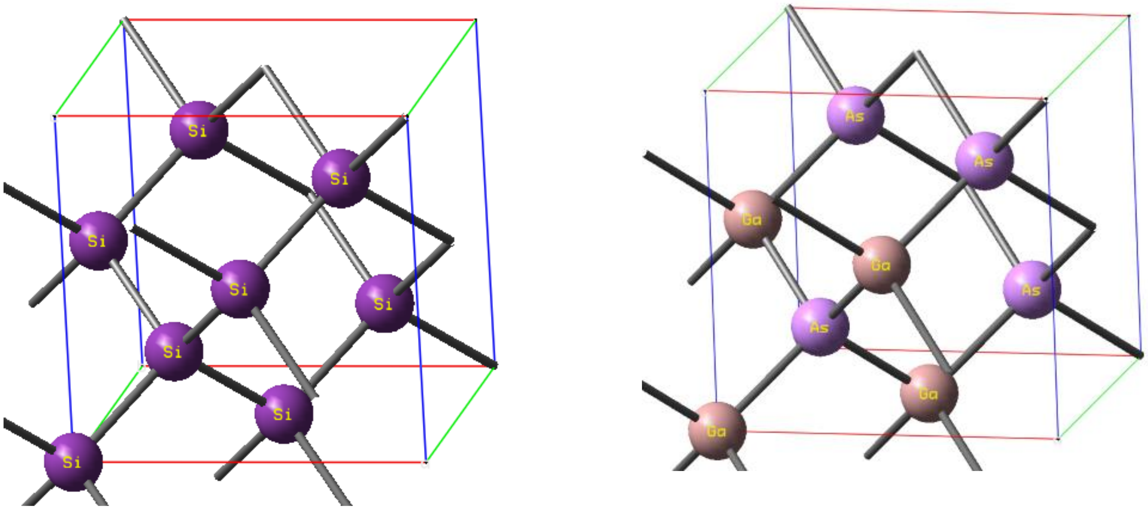

Figure 2.2: Views of the tetrahedral bonding arrangement in both diamond (left) and zincblende (right) lattices. The diamond lattice can be thought of as a face-centered cubic lattice with a two point basis occupied by identical atoms, whereas the basis is occupied by two different atoms in a zincblende structure.

equivalent due to symmetry, such as the [100], [010], and [001] planes are referred to as <100> planes. When dealing with directions in the lattice, the [100] direction, for example, is the unit normal for the [100] plane. Views of the GaAs zincblende lattice along the [100], [010] and [001] directions are shown in Figure 2.3a to illustrate the symmetry of these planes. This situation obviously applies to the diamond lattices as well. The differences come about when viewing the crystals along the <111> directions. Diamond lattices have inversion symmetry, and are known as centrosymmetric structures. On the other hand, zincblende structures lack inversion symmetry. This is apparent in Figure 2.3b, where views of each crystal along the [111] and [-1-1 1] directions are shown. When viewed along these directions, different atoms are seen depending on the orientation.

2.3 Phonons

Treatment of vibrations in both crystals with a monatomic basis and crystals with a two atoms per primitive basis is given in this section. We begin by considering simple cubic crystals with a monatomic basis, with atoms of mass M. Solutions take on their simplest form for vibrations along the <100>, <110>, and <111> directions. In these cases, vibrations of the crystal result in entire planes of atoms moving either perpendicular or parallel to the direction of the wave. In this way, phonons are waves that propagate with wavevector $\boldsymbol{k}$ and can have a polarization either perpendicular or parallel to $\boldsymbol{k}$. The fact that vibrations in a crystal can be described by planes of atoms reduces the mathematical problem to one dimension. That is we can consider a single coordinate U_n representing the plane n, and its displacement from equilibrium. It is useful to note that for every wavevector there are three modes as solutions: two transverse, and one longitudinal.

Consider a set of ionic planes with atoms of mass M separated by a distance a. The distance to the n^{th} plane is given by na. By assuming the force between planes is a linear function of the displacements between planes, and accounting for only nearest neighbour interactions, the total force on plane n induced by planes $n+1$, and n-1 is given by the following equation of motion [37]

$$M\frac{\partial U(na)}{\partial t^2} = -C[2U(na) - U(n-1)a - U(n+1a)] \qquad 2.5$$

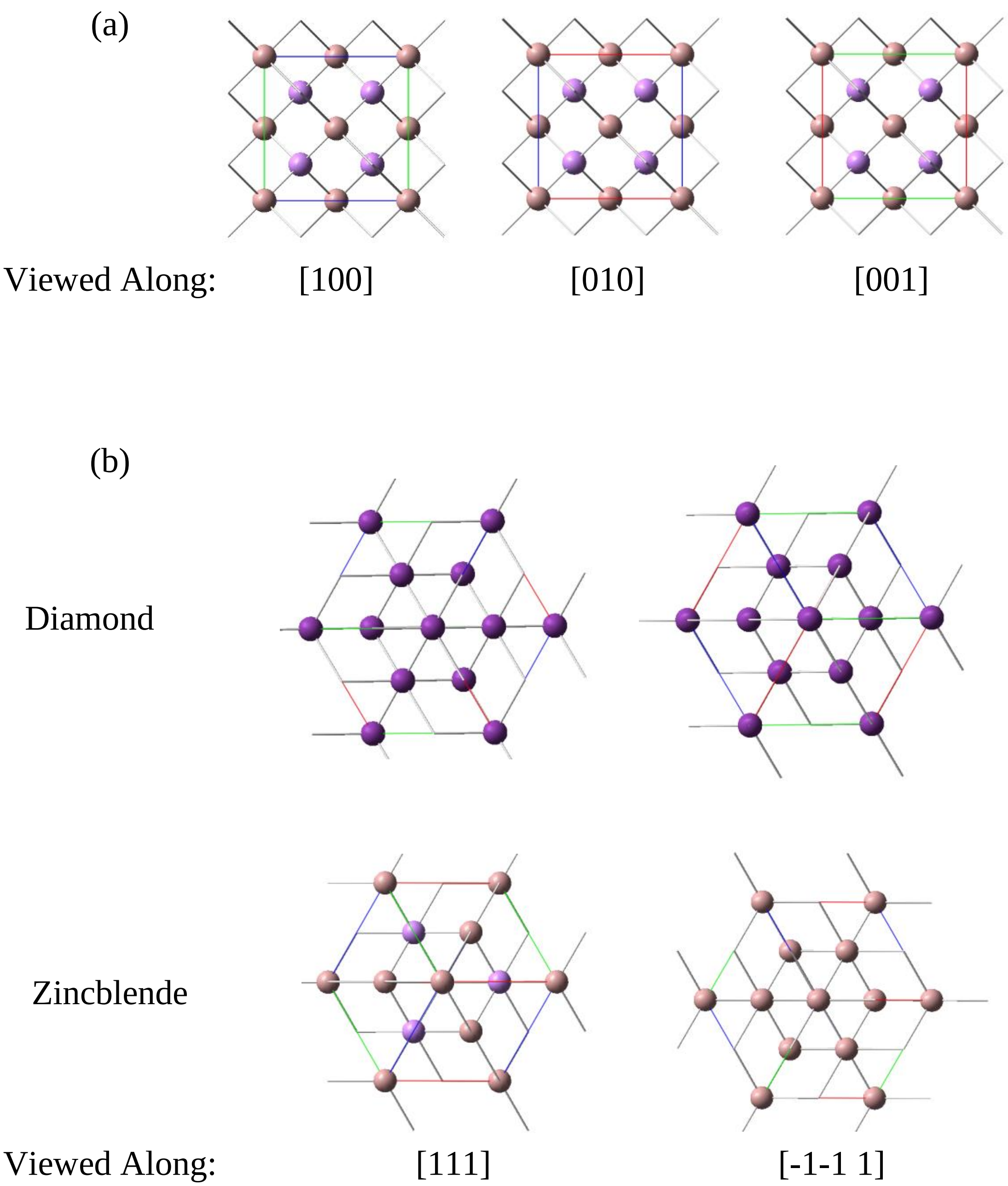

Figure 2.3: (a) View of zincblende structure along the <100> directions. The same symmetries apply to the diamond lattice as well. **(b)** View of diamond and zincblende along the [111] and [-1 -1 1] directions.

These equations are identical to those obtained when considering each ion is connected by springs with spring constant *C*. Seeking travelling wave solutions of the form $u(na,t)\sim e^{i(kna-\omega t)}$, equation (1) takes the form

$$-M\omega^2 e^{i(kna-\omega t)} = -C\left[2 - e^{-ika} - e^{ika}\right]e^{(ikna-\omega t)} \qquad 2.6$$

$$-M\omega^2 = -2C(1-\cos ka) \qquad 2.7$$

Requiring that $e^{i(kNa)} = 1$ due to periodic boundary conditions, we consider only values of k which lie between -π/a and π/a. These values correspond to edges of the Brillouin zone. The dispersion relation ω(k) becomes

$$\omega(k) = \sqrt{2\frac{C}{M}(1-\cos ka)} = 2\sqrt{\frac{C}{M}}\left|\sin\frac{1}{2}ka\right| \qquad 2.8$$

Here *ω(k)* is an even function of *k* and therefore *ω(k)= ω(-k)*. This dispersion relation is plotted in Figure 1.4. The ionic displacements are just the real and imaginary parts of $u(na,t)$:

$$u(na,t)\sim\begin{cases}\cos(kna-\omega t)\\ \sin(kna-\omega t)\end{cases} \qquad 2.9$$

These solutions describe waves propagating with wavevector *k*, phase velocity $v_p = \omega/k$, and group velocity $v_g=\partial\omega/\partial k$. When the wavelength is large compared to the spacing between ions (*k* is small compared to π/a), the dispersion relation becomes linear:

$$\omega(k) = \sqrt{2\frac{C}{M}(1 - \cos ka)} = \left(a\sqrt{\frac{C}{M}}\right)|k| \tag{2.10}$$

This is same situation frequently encountered when considering light waves. When *ω(k)* is linear, the phase and group velocities are identical. In this connection, the dispersion curve consists of only acoustic branches.

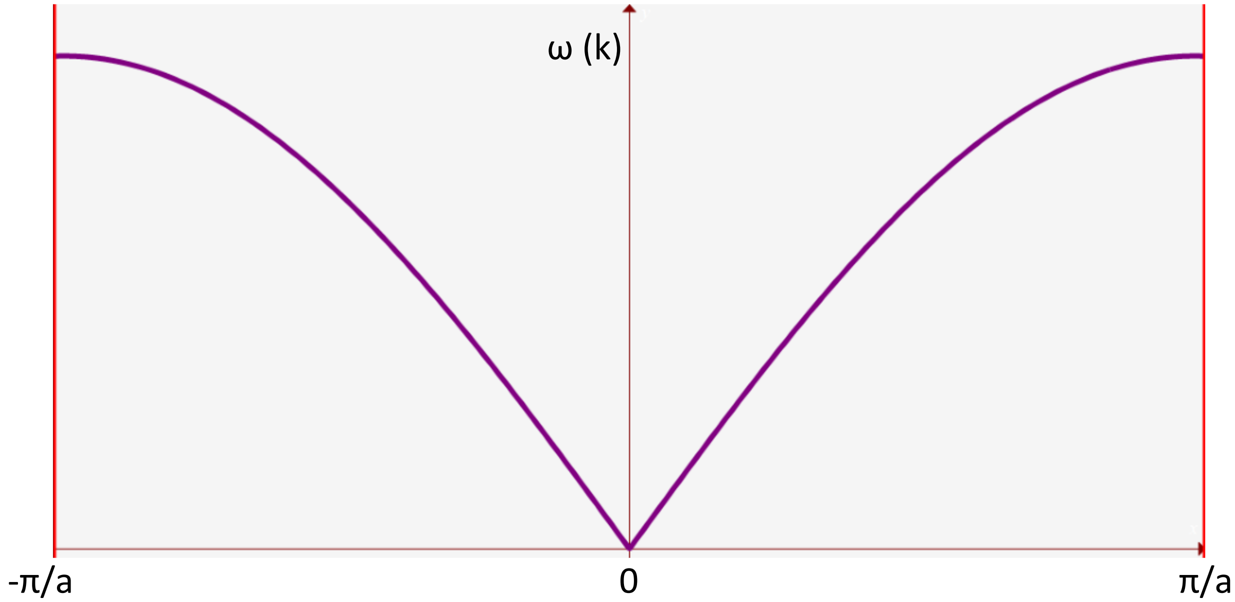

Figure 2.4: Dispersion relation for a monatomic chain with spacing *a*. The group velocity $\partial\omega/\partial k$ vanishes at the boundaries of the zone.

Extending these ideas to lattice with two-atom basis requires that we consider ions which are connected by two different spring constants, C and G. We could equally have considered two ions of different masses connected by the same spring constant as well. Following the procedure outlined above yields the following relationship between ω and k:

$$\omega^2 = \frac{C+G}{M} \pm \frac{1}{M}\sqrt{C^2 + G^2 + 2CG\cos ka} \tag{2.11}$$

Thus there are two dispersion relations for k. The first branch is the acoustic, with $\omega(k) = 0$ at $k=0$, and $\omega(\pm\pi/a) = \sqrt{2G/M}$. The other branch is known as the optical branch, which starts at $\omega(0) = \sqrt{2(C+G)/M}$, and decreases to $\sqrt{2C/M}$ at the zone edges. Figure 2.5 shows the dispersion relations for a linear chain with a two atom basis.

In a three dimensional lattice with a basis, the ideas remain the same. The effect of a polyatomic basis is to produce optical branches. In three dimensions, for every value of the wavevector $\boldsymbol{k}$, there will be 3n branches in the phonon dispersion relation. Here n represents the number of ions in the basis. Three of the $3n$ branches are acoustic, and the remaining 3n-3 are the optical branches. Along these lines, phonons can be either acoustic or optical, and have polarizations which are perpendicular, known as transverse, and parallel, known as longitudinal, to the direction of propagation. These are denoted as TA, LA, TO, and LO modes respectively.

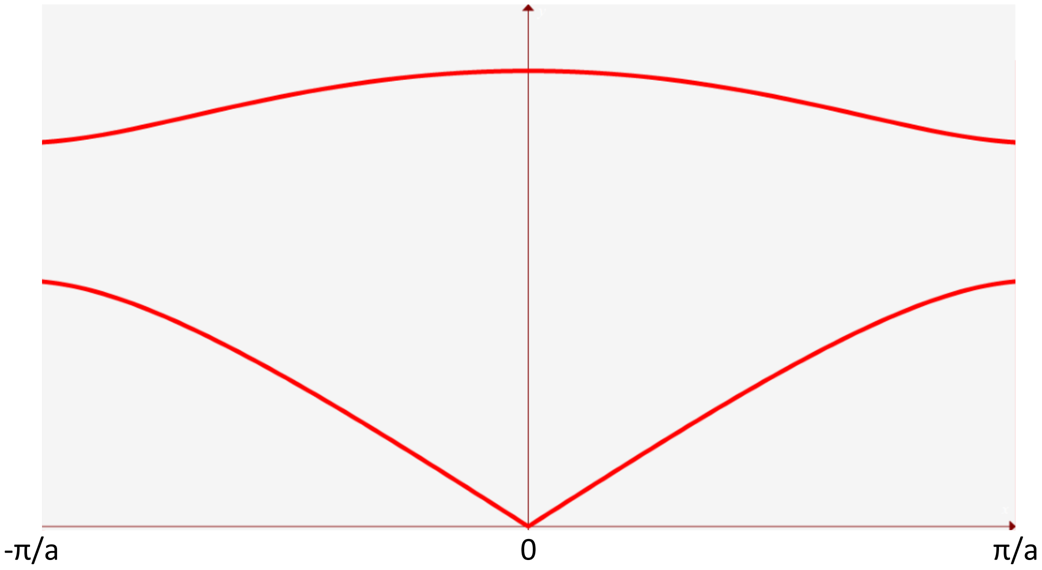

Figure 2.5: Phonon dispersion relation for linear chain with a diatomic basis. The effect of two different atoms is that an optical branch is now seen in the dispersion relation. This branch is responsible for the optical behaviour of crystals.

2.3.1 Surface Phonons

Surface active modes in nanowires are similar to bulk phonons, however the atomic displacements are confined to the near surface region of the material, where periodic boundary conditions break down. The amplitudes of these displacements will decay as one gets further from the surface. Compound semiconductors exhibit a charge distribution between their cation and anion lattices. In keeping with this, a dispersion relation is set up between the phonon frequency and the wave vector measured along the surface. The surface mode, ω_S, lies between those of the longitudinal and transverse phonons. Strictly speaking the dispersion relation depends on the dielectric functions of the semiconductor, and that of the material in contact with the surface, which in most cases is a thin layer of oxide surrounded by air [36].

The interface modes which appear whenever there is an interface between two materials are generally localized to the interface, and propagate along the interface[14]. For a nanowire geometry, which is akin to a long filament, the solutions are found using Maxwells equations with appropriate boundary conditions. The interested reader is referred to the literature [36, 37] for an in-depth analysis of these solutions. Here a brief description of the physical origin of surface phonon modes is given.

For an infinite sheet between a dielectric of ε_m and a material $\varepsilon(\omega)$, the vibrational frequency of the surface mode is given by the following expression [36]:

$$\epsilon(\omega) + \epsilon_m = 0 \tag{2.12}$$

For cylindrical interfaces between a dielectric medium ε_m, and a material, $\varepsilon(\omega)$, the surface phonon frequency is calculated by solving the following equation [36,28]:

$$\epsilon(\omega) + \epsilon_m f(kr) = 0 \tag{2.13}$$

where r is the radius of the nanowire cylinder, and $f(kr)$ is defined as

$$f(kr) = \frac{I_0(kr)K_1(kr)}{I_1(kr)K_0(kr)} \tag{2.14}$$

where I and K are Bessel functions. For an infinitely long cylindrical nanowire, with a finite radius, it has been shown that the dispersion relation for surface phonons is given by [36,28],

$$\omega_s^2(k) = \omega_0^2 + \frac{\omega_p^2}{\epsilon' + \epsilon_m f(kr)} \tag{2.15}$$

where ω_p is the plasma frequency, and ε' is the high frequency dielectric constant of the material. It is pointed out that the above expressions for surface phonon frequencies only apply for nanowires with a circular cross section, and where the phonon wave vector $\boldsymbol{k} >> \omega/v_p$.

A few studies [37, 38] have introduced a dielectric continuum model for rectangular cross section nanowires. The model begins with ignoring the exponentially decaying electric fields at the corner regions, allowing for the solution to be separable into components in the plane perpendicular to the wire axis. In this case there will be symmetric and asymmetric modes. By applying the correct boundary conditions, the dispersion relations for surface phonons in a square cross-section nanowire geometries can be calculated. The following expressions have been obtained for the symmetric, ω_s, and asymmetric, ω_{As}, phonon dispersion relations [28]:

$$\begin{aligned} \omega_s &= \omega_{\mathrm{TO}}^2 \frac{\epsilon_0 \tanh(qL/2) + \epsilon_m}{\epsilon' \tanh(qL/2) + \epsilon_m} \\ \omega_{\mathrm{As}} &= \omega_{\mathrm{TO}}^2 \frac{\epsilon_0 \coth(qL/2) + \epsilon_m}{\epsilon' \coth(qL/2) + \epsilon_m} \end{aligned} \qquad 2.16$$

Here L is the edge length of the nanowires. As the edge length approaches infinity, the hyperbolic tangent arguments go to unity, and both expressions for the symmetric and asymmetric modes in equation 2.16 become that of an infinite, flat, semiconductor surface. In general, the surface phonon frequency decreases with decreasing nanowire diameter. Furthermore, the position of the surface phonon peak is sensitive to the dielectric constant of the surrounding medium. Surface phonons will not be resolved in elemental semiconductors, like Si, since the TO and LO phonon frequencies in these systems are degenerate.

2.4 Raman Selection Rules

In general, a backscattering configuration is used where the scattered light is detected along the same axis as the excitation beam. The scattered energy per unit time into a solid angle $d\Omega$ is given by

$$I_s = I_i \cdot \frac{4\pi^2\alpha^2}{\upsilon_s^4} |\hat{e}_i \cdot \boldsymbol{R} \cdot \hat{e}_s|^2 d\Omega \tag{2.17}$$

Here, α is the fine structure constant, ν_s is the wavenumber of the scattered light, $\bar{R}$ is known as the Raman scattering tensor, and $\widehat{e_i}$ and $\widehat{e_s}$ are the incident and scattered polarization unit vectors respectively. Along these lines, Raman scattering experiments which involve fixed incident and detected polarizations will select certain elements of the scattering tensor $\bar{R}$. These are commonly referred to as Raman selection rules. It is instructive to note that the Raman tensor has the same form as polarizability tensor.

To illustrate how selection rules can affect Raman spectra from crystals, we will use zinc-blende GaAs as an example. Since we are interested in the vibrational properties of semiconductor crystals, phonons are involved. The unit cells of diamond and zinc-blende each contain two atoms. This leads to six branches in the phonon dispersion relation, three of which are acoustic branches, and the remaining three are optical branches [39]. In each case, phonons can either be longitudinal or transverse. Longitudinal phonons involve atomic displacements that are along the direction of the wave vector ***k***, and transverse phonons involve vibrations that are perpendicular to ***k***.

Transverse acoustic (TA), and longitudinal acoustic (LA) phonons represent shear and compressional sound waves in the crystal. First order Raman spectra arise from transverse optical (TO) and longitudinal optical phonons only (LO). In the case of Si, the LO and TO phonon frequencies are degenerate at 520 cm^{-1}. This is due to the bonding nature in Si being purely covalent, and no net charges are associated with the atoms in each unit cell. Thus, atomic displacements experience the same restoring force regardless of the type of vibration. However in zinc-blende crystals like GaAs, the LO phonon appears at a higher energy (~290 cm^{-1}) than the TO phonon (267 cm^{-1}). This is due to the ionic nature of the bond between the Ga and As atoms. The As atoms contribute more electrons to the bond than the Ga atoms, and therefore electrons spend more time on average near the As atoms giving them a slightly negative charge. To illustrate how this leads to different restoring forces for transverse and longitudinal vibrations, we consider the [111] direction. The Ga, and As atoms lie in planes which are perpendicular to the [111] direction as shown in Figure 2.6. The planes of Ga atoms can be thought of as sheets of positive charge, and the planes of As atoms can be considered to be sheets of negative charge. In this case, a TO mode involves these planes sliding back and forth past each other, without any increase in distance between the planes. However the situation is different for the LO phonon modes, where the separation distance changes between the charged planes. This has the effect of creating an additional Coulomb restoring force, increasing the frequency of the LO phonon mode relative to the TO mode [40].

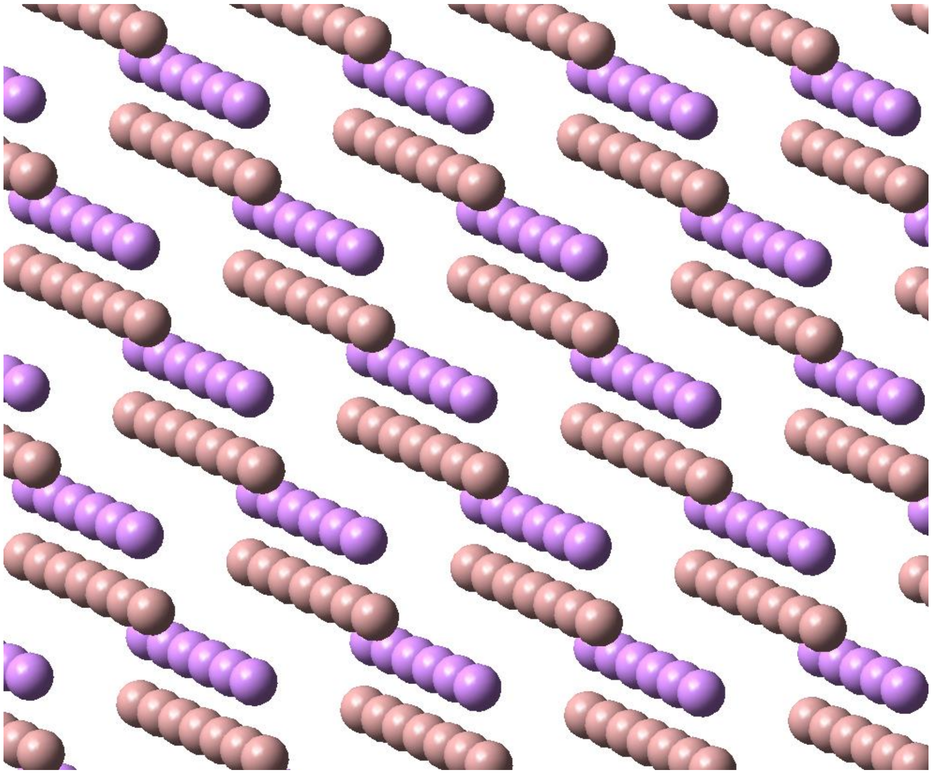

Figure 2.6: Zincblende GaAs lattice showing the planes which lie perpendicular to the [111] direction. An additional Coulomb restoring force is created during a LO vibration and therefore has a higher energy than the TO vibration. The bonds between the atoms have been removed for clarity.

For zinc-blende crystals, the Raman tensor is a third-rank tensor with linearly independent components with indices xyz and its corresponding cyclic permutations. Optical phonons polarized along the x, y, and z directions will have each have two non-zero components in their respective Raman tensor. Using the standard Cartesian basis the Raman tensors for zinc-blende crystals are.

$$R(x) = \begin{pmatrix} 0 & 0 & 0 \\ 0 & 0 & 1 \\ 0 & 1 & 0 \end{pmatrix} R(y) = \begin{pmatrix} 0 & 0 & 1 \\ 0 & 0 & 0 \\ 1 & 0 & 0 \end{pmatrix} R(z) = \begin{pmatrix} 0 & 1 & 0 \\ 1 & 0 & 0 \\ 0 & 0 & 0 \end{pmatrix}$$

As an example, let us consider spectra collected from a (100) surface in the backscattering geometry. A TO phonon will have a polarization that is perpendicular to the [100] direction. In general the polarization will have components in both the [010] and [001] directions. Therefore the Raman tensor for a TO phonon propagating along the [100] direction has a Raman tensor which is a linear combination of $R(y)$ and $R(z)$. In the backscattering geometry, both $\mathbf{k_i}$ and $\mathbf{k_s}$ are along the [100] direction, and therefore e_i and e_s have no components along this direction for TO phonons. However the quantity $|\hat{e}_i \cdot (\boldsymbol{Rx} + \boldsymbol{Ry}) \cdot \hat{e}_s|^2$ is non-zero only if either e_i or e_s has components which are along the [100] direction. Therefore TO scattering is forbidden from (100) surfaces in the backscattering geometry. In contrast, the LO phonon has a polarization which is along the [100] direction in this configuration with Raman tensor $R(x)$, and is allowed. Using the same ideas, one can derive the selection rules for TO and LO phonons for other surfaces and scattering geometries as well. Both TO and LO phonons are observed from (111) surfaces, and only TO scattering occurs for spectra recorded from (110) surfaces. For bulk materials, these selection rules become particularly important. However, for nanowires which are fabricated using either top down or bottom up approaches have sidewalls which represent different crystalline facets. In this connection, there is a breakdown of the Raman selection rules, and therefore TO and LO scattering is usually observed from GaAs nanowires. This is shown in Figure 2.7, where Raman scattering from both TO and LO phonons is experimentally observed from a sample of 50 nm diameter GaAs nanowires, and only LO scattering is observed from the [100] starting wafer.

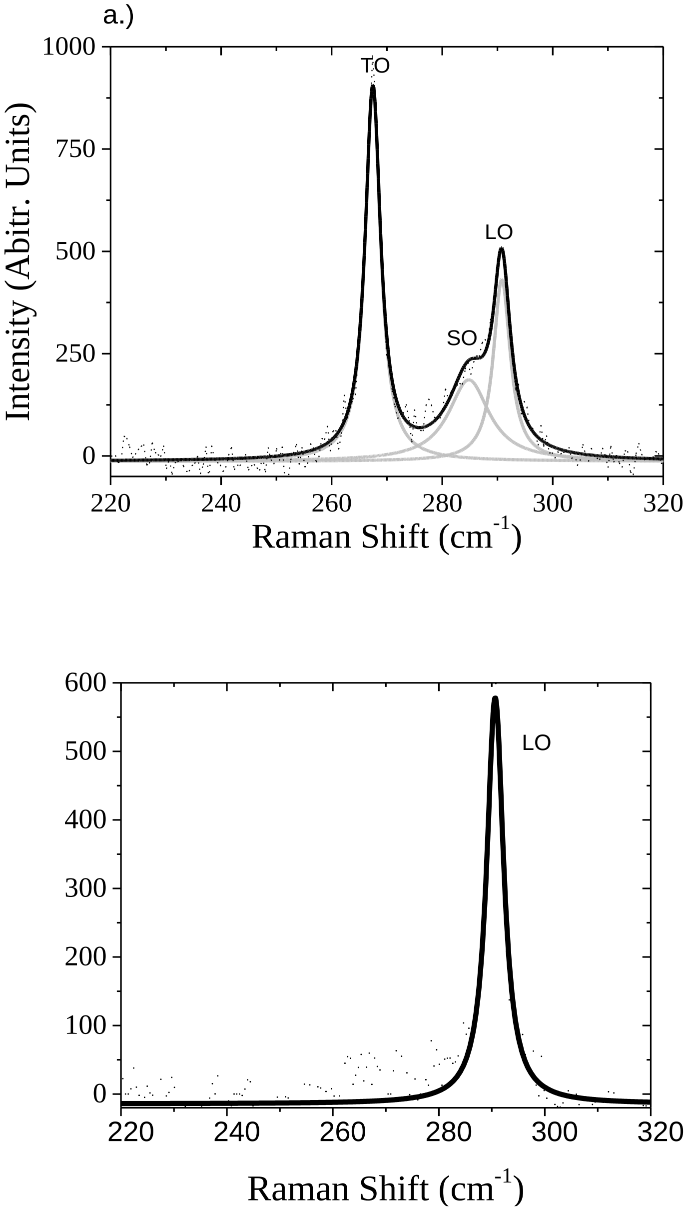

Figure 2.7: a.) Spectral deconvolution of the Raman spectrum for the 50 nm diameter sample showing both TO and LO scattering centered at 267 cm^{-1} and 291 cm^{-1} respectively. A third peak corresponding to the surface phonon mode also appears between the TO and LO phonon modes, as discussed in the first chapter. **b.)** Raman scattering from a bulk [100] GaAs wafer where only LO scattering is allowed and TO scattering is forbidden as expected from the selection rules.

This lays the foundation for Raman scattering in crystals. The origins and meanings of the TO and LO modes are now understood. Furthermore the selection rules are now known, and explains why two peaks can appear from crystals with a multi-ion basis. The ideas presented in this chapter will be used to analyze and discuss collected Raman spectra from Si, GaAs and a-Si nanowires in the next chapter.

CHAPTER 3

Experimental Section

3.1 Nanowire Samples

The nanowire samples used in this study were fabricated by other members of our research group. The fabrication cleanroom is located in the Quantum Nano Centre at the University of Waterloo. The Si, GaAs, and a-Si nanowires examined in Chapters 4,5,6,7 were fabricated by current PhD candidate, Nanvneet Dhindsa. The details of his fabrication processes are available in the literature [9,19,41]. The silicon nanowires examined in Chapter 4, Section 4.1, were fabricated by Dr. Reza Khorasaninejad [8]. What follows is a brief outline of the fabrication procedure for each type of semiconductor nanowire appearing in this thesis.

All nanowires were fabricated using a top-down approach. To begin with, the various substrates were spin coated with poly(methyl methacrylate) (PMMA), and baked at 350 K for 20 minutes. The spin coated wafer / substrate was then exposed to an electron beam in a RAITH 150-TWO, at 20 kV, and then developed in a mixture of methyl isobutal ketone (MIBK) : isopropyl alcohol IPA (1:3) at 293 K for 30 s, dipped in IPA for 30 s, and followed by nitrogen drying. For the Si, and a-Si nanowires, 30 nm thick aluminum masks were used for the plasma etching process. For GaAs nanowires, an Al/Cr (20 nm/30 nm) mask was used. The masks protect the substrates from etching, resulting in the formation of nanowires. Then the samples were inserted in an ICP–RIE plasma etcher (Oxford Plasmalab 100 ICP380), and the etching process was carried out using two gas mixtures depending on the semiconductor material being etched. Table 3.1 lists the gas mixtures used for etching the Si, a-Si, and GaAs nanowire samples. Also listed are the gas pressures. Each nanowire array spans an area of 100 × 100 μm^2 and the nanowires within each array are arranged in a square lattice. Figures 3.1, 3.2, and 3.3 show representative SEM images of Si, GaAs, and a-Si nanowire arrays respectively. It is instructive to note the a-Si nanowires were etched into a grown amorphous silicon layer on a glass substrate.

Semiconductor Material	**Gas Mixture (sccm)**	**Gas Pressure (Torr)**
Si	SF_6 (20 sccm) C_4F_8 (40 sccm)	10
a-Si	SF_6 (20 sccm) C_4H_8 (40 sccm)	10
GaAs	Cl_2 (20 sccm) and N_2 (5 sccm)	10

Table 3.1: Gas mixtures and pressures used for etching the various semiconductor materials to form nanowires [9,19,41].

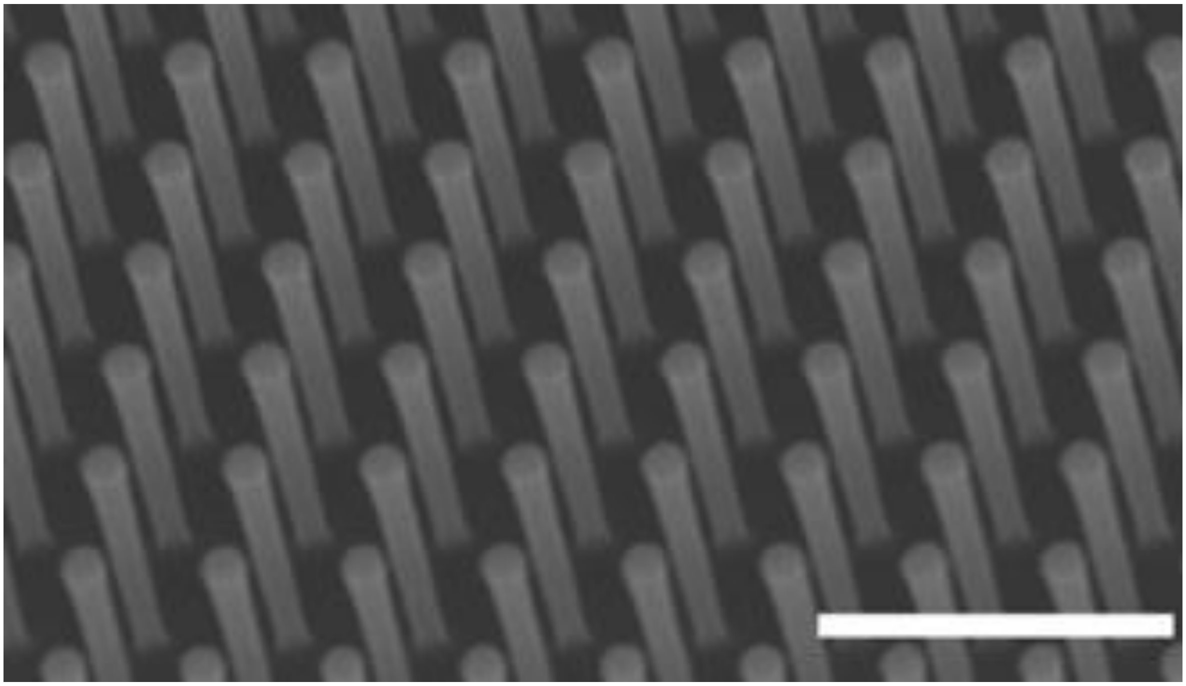

Figure 3.1: Representative SEM image of an etched Si nanowire array, showing a regular arrangement of vertical 135 nm diameter Si pillars. The scale bar is 1 µm.

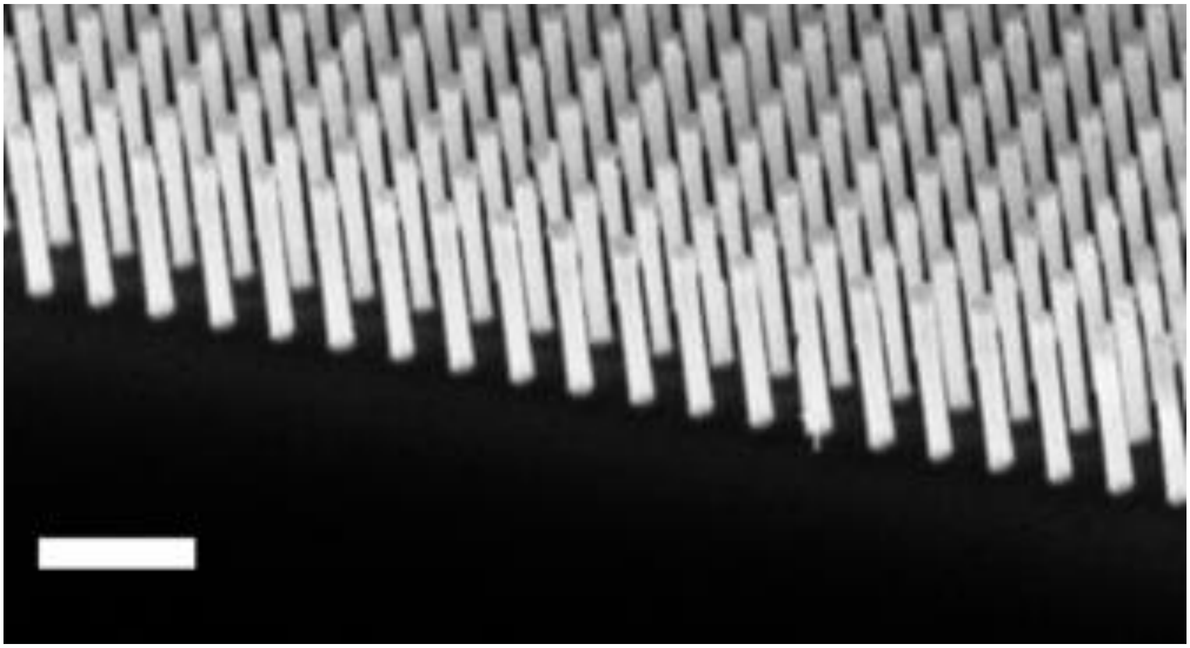

Figure 3.2: SEM image of a square array of 125 nm diameter, 1 µm long GaAs nanowires. The uniform pitch and vertical nature of nanowires are clearly seen. The scale bar is 1 µm.

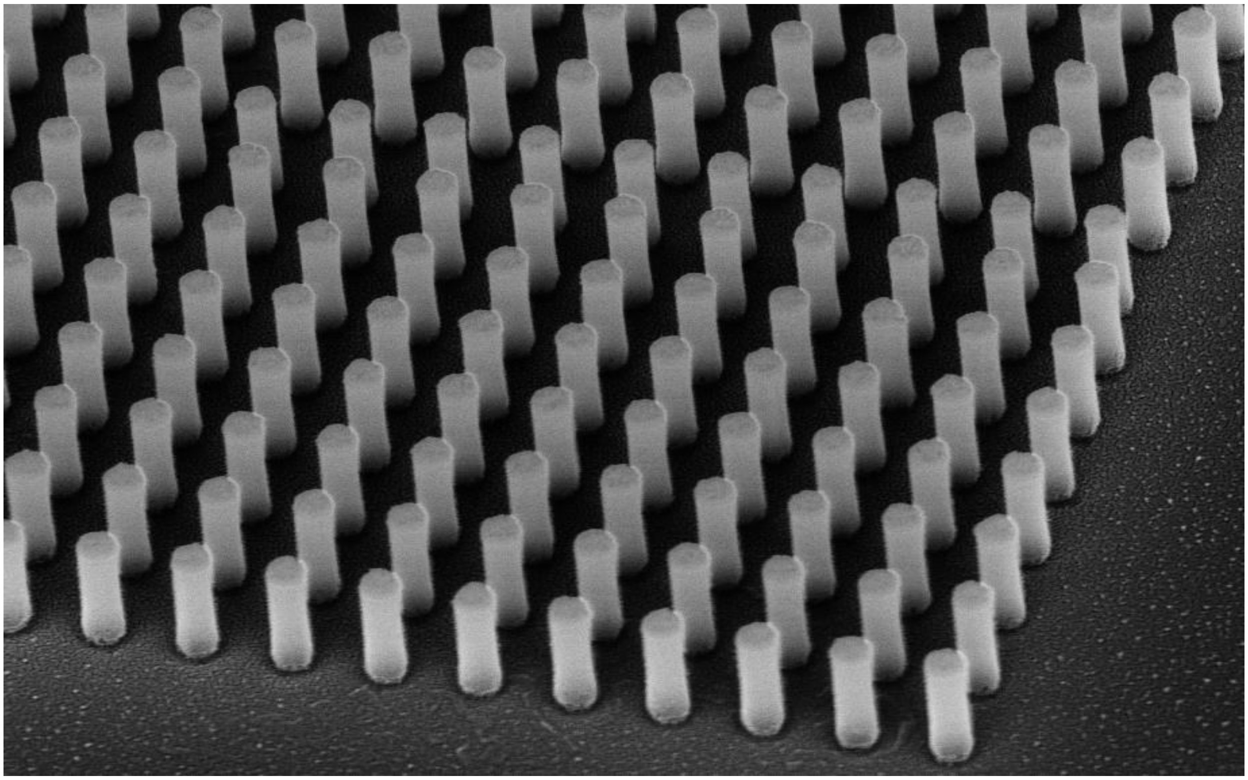

Figure 3.3: SEM image of a-Si nanowires. Since the nanowires are on a glass substrate, charging effects make imaging the array quite difficult. However vertically oriented nanowires can still be made out in the image.

3.2 Raman Spectroscopy

A typical Raman spectroscopy setup involves an excitation laser, optics to isolate the Raman signal from the laser line, and a spectrometer. The most common laser wavelengths used are 485 nm, 514 nm, 633 nm, and 785 nm. The choice of wavelength depends on the sample type being studied. For example, to quench fluorescence, longer wavelengths are generally desired. Along these line longer wavelengths are also used when studying biological specimens to avoid over heating the samples.

The main difficulty that is encountered when putting together a Raman spectrometer is the ability to separate the very weak Raman signal from the strong Rayleigh scattered light. To overcome this notch filters can be used. The issue here is that notch filters generally do not allow for measurement of low frequency vibrational modes (< 100 cm-^{1}), which can be an issue for solid state samples. Stray light can also be generated in the spectrometer and depends on the quality of the gratings, and this connection holographic gratings are generally employed. Holographic gratings produce much less stray light than their ruled counterparts. Another method of reducing stray light is to use a double or triple spectrometer setup which have multiple dispersion stages. It is also instructive to note that the most common type of detector used today is a Charge-Coupled device (CCD) detector.

3.2.1 Confocal Setup

A further reduction in stray light can be achieved by using a confocal microscope. A typical confocal Raman spectrometer setup is shown in Figure 3.4. In this case, the incoming laser light is focused onto the sample using a microscope objective, thus illuminating a small area of the sample. Raman scattered light is collected through the same objective (backscattering configuration), after which a double action filter rejects the laser light, and allows the Raman scattered light through. Any rays which do not originate from the focal spot are rejected by a pinhole which is placed directly after the filter, and therefore the recorded spectra are from the focal point only. By varying the aperture size of the hole, different degrees of spatial resolution can be achieved. Along these lines, a confocal setup can not only be used to gain information in the horizontal plane, but also the vertical direction as well. To achieve this, a piezo controlled stage is usually required.

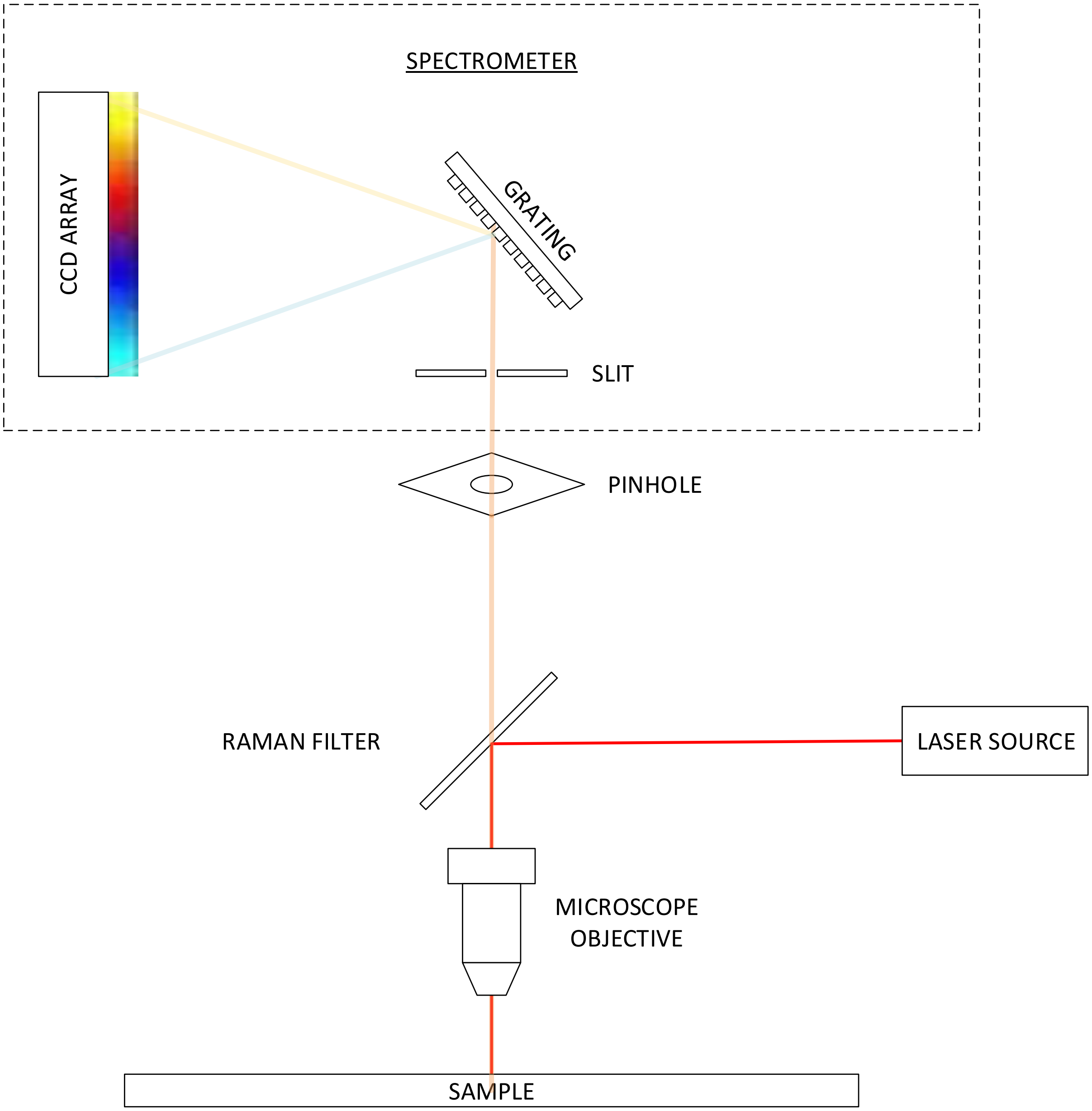

Figure 3.4: Typical confocal Raman setup. The purpose of the pinhole is to reject scattered light which does not originate from the focal spot of the objective, further reducing stray light.

Additionally, a confocal setup can be used to create a Raman image of sample in both the horizontal (x,y) and vertical directions (z).

Component	Specifications
Laser Source	532 nm, and 633 nm. Max Power: 40 mW
Grating	1800 lines/mm
Pinhole Size	250 um
Detector	Nitrogen Cooled CCD
Microscope Objectives	20 X (0.35 NA) and 50 X (0.5 NA)

Table 3.2: Specifications for various components in the Raman spectrometer. These values were used for all experiments appearing in the thesis.

3.2.2 Raman Measurements

All Raman measurements were performed on Jobin Yvon Horiba LabRam spectrometers in the backscattering configuration. The power density was varied for each sample accordingly using a combination of 20x and 50x lenses, as well as various neutral density filters. For all silicon nanowire measurements appearing in Chapter 4, an excitation wavelength of 633 nm was used. The GaAs nanowire Raman measurements in Chapters 4,5 and 7 employed excitation wavelengths of 532 nm, and 633 nm respectively. Finally for a-Si nanowire samples, an excitation wavelength of 532 nm was used. The choice of wavelength was subject to availability. Exact details (power density, number of accumulations, exposure times) for each measurement performed can be found in the associated chapters. Analysis of all Raman spectra was performed in the Origin software environment, and the fitting processes used are discussed where applicable. Table 3.2 lists the specifications of the laser source, objectives, gratings, and pinhole size used in all experiments appearing in thesis.

CHAPTER 4

Raman Scattering from Vertical Nanowire Arrays

Introduction

When nanometer sized structures are created, electron and phonon transport can be significantly altered affecting both the electrical and thermal conductivities of nanowires with respect to their bulk counterparts. Furthermore, the vibrational properties of nanowires are another topic of interest, in which many Raman studies have been published in an effort to understand phonon confinement and heating effects [28-32]. Phonon confinement is well understood in terms of the RCF model [29, 30], however a spectral redshift of at most only 1 cm^{-1} is predicted for the first-order mode at 520 cm^{-1} in Si when the diameter of the nanowires is 10 nm, whereas shifts of 10-15 cm^{-1} have been reported in NWs which are larger than 20 nm in diameter [31-33]. The general conclusion has been that both phonon confinement and local heating can be responsible for the observed broadening and spectral redshift of the first order Raman peak, and that only nanowires with diameters below ~ 20 nm experience quantum confinement effects [28]. The main shifts observed experimentally result from local heating. Broadening of the first order mode can also be indicative of the lack of long range order, a possibility which was not considered in the previous works mentioned. Raman spectroscopy is proving to be a powerful tool which can be used to characterize various types of nanowires in order to determine their crystalline structure and thermal properties relative to bulk. In this chapter focus is given to understanding the Raman spectra from vertically arranged Si, GaAs, and aSi nanowires.

4.1 Silicon Nanowires

The only allowed first-order Raman processes in Si are from the zone center phonons, which results in a well-defined sharp Lorentzian lineshape centered at 520 cm^{-1} with a FWHM of ~ 3.4 cm^{-1} [50]. The diamond crystalline nature of the NWs can be quickly confirmed by observing the most dominant Raman peak belonging to the first-order phonon, centered in the Brillouin zone [43, 44]. Table 4.1 lists the measurement parameters used to acquire Raman spectra from silicon nanowires. For the etched vertically ordered silicon nanowires with diameters ranging from 30 nm to 60 nm, the zone-center phonon mode consistently appears at 520 ± 0.3 cm^{-1} (within the accuracy of the measurement), and is well fit to a Lorentzian lineshape with a FWHM 3.4-3.5 cm^{-1} (Figure 4.1). These values are in excellent agreement with the values for bulk crystalline silicon. No spectral shifts or broadening of the first order mode was observed from the etched arrays, suggesting that heating and phonon confinement effects do not exist in our samples. This is consistent with the RCF model used to describe phonon confinement, which predicts a discernible redshift in the first order line only for diameters less than 20 nm [28]. Since bulk silicon is an excellent thermal conductor, and the etched NWs have maintained the lattice properties of the bulk as evidenced in the Raman spectra, the lack of heating results from the presence of long range crystalline order in the SiNWs. Deviation from the crystal structure in the form of defects and grain boundaries will act as scattering centers, which would decrease the ability for the nanowires to transfer heat to their surroundings, resulting in a broadening of the first-order mode. One Raman study [31] of grown nanowires has reported shifts of ~ 10 cm^{-1} for nanowires with diameters ranging from 20 – 60 nm, which does not agree with predictions of the RCF model. Another study [45] also observed a shift and broadening of the first-order spectrum in grown SiNWs. The general consensus is that heating from the laser, and phonon confinement can produce a broadening and shift of the first order Raman peak.

Measurement Parameter	**Value**
Laser Wavelength / Power	633 nm / 10mW
Laser Power Density	100 W/mm^2
Exposure Time	2 s
Accumulations	10

Table 4.1: Measurement parameters used to acquire Raman spectra from vertical Si nanowires.

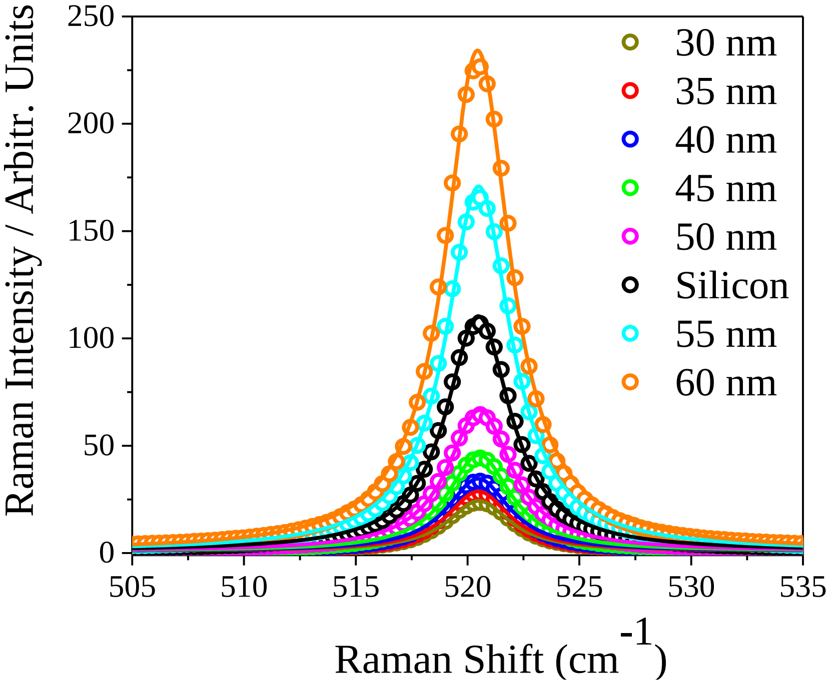

Figure 4.1: First order Raman scattering from arrays of vertically etched nanowire arrays with diameters ranging from 30 nm to 60 nm. Each sample has a spectrum that is well to fit to Lorentzian line (solid line) with a FWHM of 3.4-3.5 cm^{-1}.

In contrast, etched crystalline SiNWs as low as 30 nm are still able to conduct heat resulting in a undistorted first order line, which make them attractive model system to study phonon confinements effects if one can achieve diameters less than 20 nm in the fabrication process.

The crystalline silicon structure of the NWs was further confirmed by acquiring the multi-phonon spectrum and comparing it to bulk Si. The multi-phonon Raman spectrum of our SiNWs is identical to that of the bulk which is well understood [42-44], and is shown in Figure 4.2. The main two-phonon peaks in bulk Si are the 2TO(L) mode appearing at ~940 cm^{-1}, TO(X) + TA(X) at ~ 610 cm^{-1}, TO(W) + TA(X) at ~ 650 cm^{-1}, 2TA(W) at ~ 440 cm^{-1}, and a 2TA(X) mode at ~ 300 cm^{-1}.

TO and TA refer to Transverse Optical and Transverse Acoustic modes respectively, and W, X, and L represent points of symmetry near the Brillouin zone center in a diamond lattice [42-44]. All of the aforementioned peaks appear in the Raman spectra for etched ordered array and are very well defined. The nanowires display two phonon peak structures, the shapes of which result from the shapes of the critical point contributions to the density of states [44]. These shapes are identical to that of bulk silicon confirming that the NWs are indeed crystalline over a long range. Other studies [31-33, 47] have presented the multi-phonon spectrum of grown SiNWs and identified various two phonon Raman peaks. However, the shapes of their two-phonon peaks have been compromised and do not have the sharp spectral features which are present in our samples. This suggests that deviations from the crystalline structure are present in those samples. In one case [31] the authors did indeed confirm the presence of stacking defaults and twins from high resolution TEM images. A simple Raman measurement, consisting of an exposure time of a few seconds, and some tens of accumulations, can rapidly verify the presence of long range crystalline order in etched arrays of silicon nanowires.

The nanowire model can also be used to study weak Raman peaks. Typically multi-phonon peaks in bulk silicon have a low intensity with some peaks barely appearing above the noise floor. According to the laws of electromagnetism, etched vertical SiNWs should display an enhancement in Raman scattering per unit volume of Si (REV), due to the large dielectric mismatch between the silicon surfaces and the surrounding air [46]. In a previous work from our group [26], the REV for nanowires ranging from 30 nm to 60 nm in diameter was studied and understood using a model based on the confinement of light within the nanowire cores. We now know that the increased REV is a result of strong excitation of the HE_{11} mode [7,19,47]. An

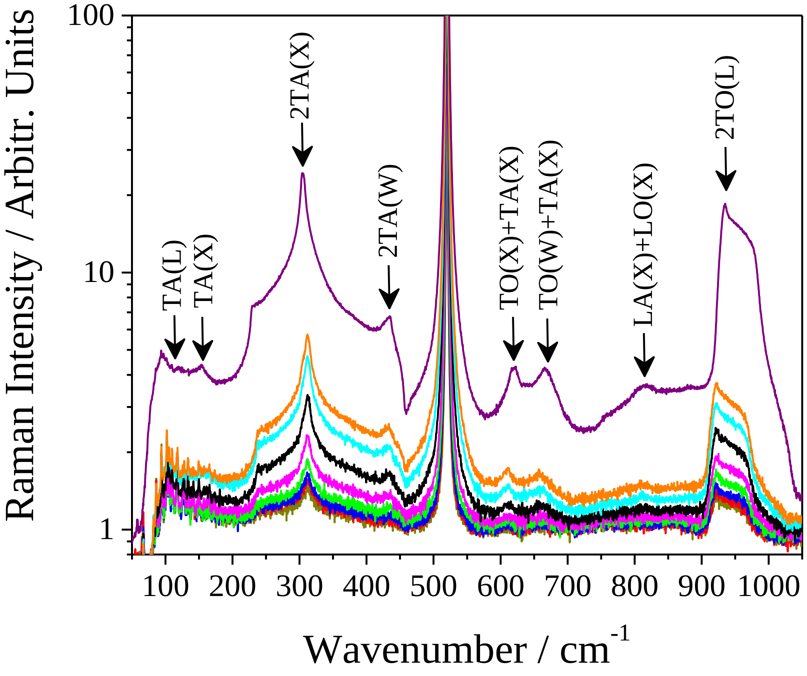

Figure 4.2: Multi-phonon Raman spectrum of etched SiNW for diameters of 30, 33, 39, 42, 47, 56, 60, and 135 nm. The Raman scattering intensity increases monotonically with NW diameter, and the results are plotted on a logarithmic scale for ease of visualization.

increasing REV vs NW diameter was observed up to maximum value of 70. In a similar study [48], an increasing trend in REV was observed for decreasing NW diameters ranging from 450 nm – 900 nm up to a maximum value of ~ 175, suggesting there is a potential to achieve a maximum in REV. This taken together with the fact that large Raman scattering enhancements which result from electromagnetic coupling of light between the wires allows for the acquisition of the multi-phonon spectrum with a significantly improved signal to noise ratio. Samples with a variation of diameters and pitches were fabricated in an attempt to achieve a high enhancement in the multi-phonon spectra of SiNWs [27]. It was observed that the Raman spectrum for 135 nm diameter NWs was greatly enhanced over the bulk and is shown in Figure 4.3 with bulk Si shown for reference. The entire multi-phonon spectrum has been enhanced over the whole spectral range. Peaks which appear in the spectrum for the large 135 nm diameter SiNWs do not appear in bulk silicon under the same experimental conditions (Figure 4.3). Low-wavenumber vibrational modes are now visible centered at ~ 150 cm^{-1}, which are identified as the TA(X) mode, and one appearing at ~ 120 cm^{-1}, identified as the TA(L) mode. A weak spectral signature at ~ 820 cm^{-1} is assigned to the LA(X)+LO(X) vibrational mode. The 2TA(X) mode at 300 cm^{-1}, and the 2TO(L) mode at ~940 cm^{-1} also show a much higher spectral intensity. Conclusively, etched arrays of vertically aligned silicon nanowires have the potential to produce high intensity higher-order Raman sidebands in silicon, allowing for a high resolution study of the multi-phonon spectra and dynamics. It is reported here that even with a large enhancement in the Raman signal from a crystalline Si sample, no fourth order processes were observed, showing even more that the Raman cross section for such a process is extremely small. Interestingly, fourth order processes have been observed from roughened silicon surfaces. Thus, lack of fourth order peaks suggest that the nanowires have been etched with smooth sidewalls, a testament to the etching processes developed in our group.

In summary, a confocal micro Raman study, covering the spectral range of 50 cm^{-1} to 1500 cm^{-1}, was carried out on an etched vertical NWs, with diameters ranging from 30 nm to 60 nm arranged in a square array with a pitch of 100 nm. These samples were previously studied for the Raman enhancement properties [26,27]. The Raman results indicate a highly crystalline nature for all of the SiNW samples studied, as evidenced by the multi-phonon spectrum matching that of a bulk crystalline silicon wafer. Additionally, the lattice vibrations of silicon resulting in three and four phonon processes can potentially be studied due to the Raman enhancement present in ordered SiNWs. In this connection an array of 135 nm diameter NWs was fabricated from which a Raman enhancement per volume (REV) of ~838 was achieved, resulting in a significantly improved signal to noise ratio in the Raman spectrum. The large enhancements resulting from efficient electromagnetic coupling could have potential in applications involving light emission from silicon.

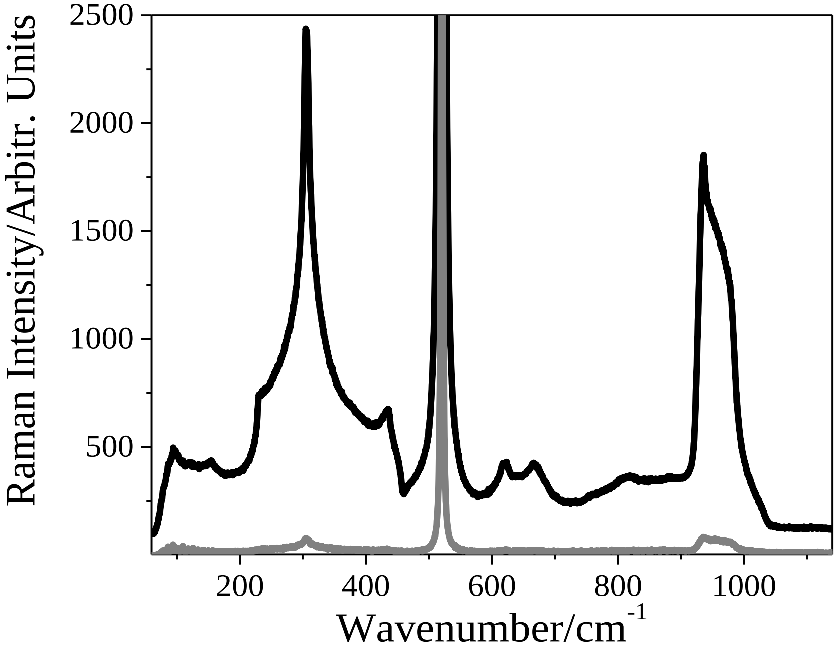

Figure 4.3: Raman spectrum from 135 nm diameter SiNWs (black trace) covering the 50 cm^{-1} to 1150 cm^{1} spectral range. The bulk silicon spectrum (gray) is shown for reference. New spectral features are observed in the low wavenumber region (100 cm^{-1} – 150 cm^{-1}) as well as in the ~ 850 cm^{-1} region

4.2 Raman Spectra of Gallium Arsenide Nanowires

Raman spectra for GaAs nanowires with diameters ranging from 50 nm to 155 nm are shown in Figure 4.4. A Raman spectrum was also measured from the unpatterned area between the nanowire arrays corresponding to the etched bottom GaAs surface, and is also shown in Figure 4.4 (labeled as “bulk”). Table 4.2 lists the acquisition parameters used to acquire the spectra seen in Figure 4.4. As discussed in section 2.4 of chapter 2, in the backscattering geometry, the Raman selection rules for zincblende GaAs forbid scattering from the tranverse optical (TO) phonon centered at 267 cm^{-1} for the (100) GaAs starting wafer, and only the longitudinal optical (LO) phonon is observed in the corresponding Raman spectrum. The etching process introduces surface roughness and crystalline damage along the nanowire sidewalls and relaxes this selection rule, and scattering by TO phonons can be observed [24]. The area of the etched wafer where the nanowires are not present only shows one spectral feature corresponding to the LO phonon. The lack of TO scattering indicates that the bottom wafer surface is still smooth after the etching process, and therefore the presence of TO scattering is from the nanowire sidewalls. This was also confirmed through optical reflection measurements by another student in our group where it was found that the reflection from the etched GaAs substrate was similar to that of the starting wafer [41]. The Raman spectra from vertically etched nanowires show three distinct spectral features for all of the diameters. In all cases, peaks corresponding to scattering from TO phonons at 267 cm^{-1} and LO phonons at 290 cm^{-1} are seen, as well as a third peak corresponding to scattering from surface optical phonons (SO) is observed.

As can be readily seen in Figure 4.4, the intensity of the LO and TO phonons is highly dependent on the diameter of the nanowires. Diameter dependent red shifts in the LO and TO phonons and concomitant broadening of the Raman lines is also observed. In order to accurately determine the peak position and full width at half maximum (FWHM) of the lines, the Raman spectra were deconvolved into three Lorentzian peaks, and a representative fit for the 50 nm diameter sample is

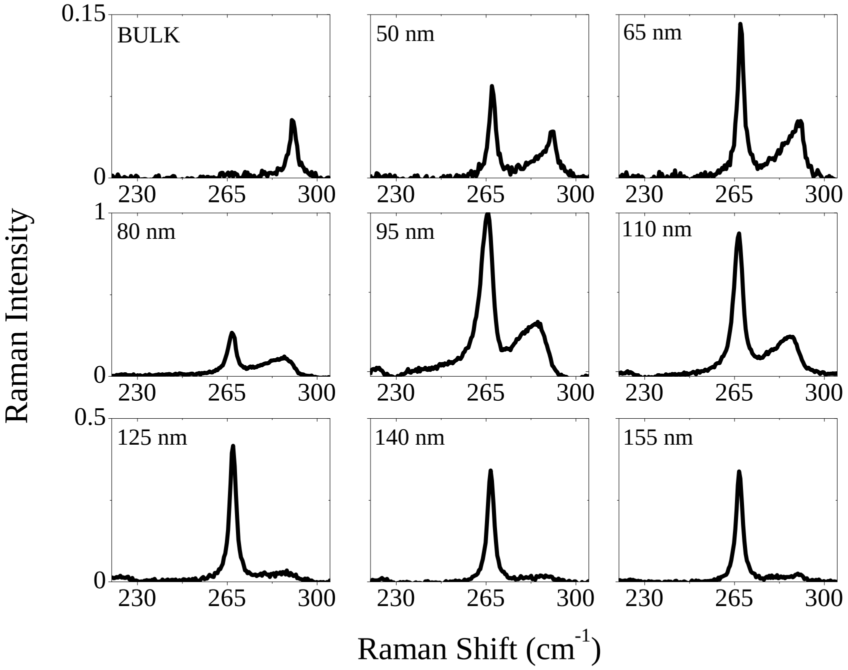

Figure 4.4. Raman spectra covering the 220 cm^{-1} to 305 cm^{-1} spectral range for eight different diameters of GaAs nanowires ranging from 50 to 155 nm. The Raman spectrum from the bulk starting wafer is also shown. For all nanowires, scattering from the LO mode at 291 cm^{-1} and the TO mode centered at 267 cm^{-1} are observed, which are consistent with scattering from the zincblende crystal structure. The SO mode centered at 286 cm^{-1} is also present in all nanowire samples.

Measurement Parameter	**Value**
Laser Wavelength / Power	533 nm / 1 mW
Laser Power Density	10 W/mm^2
Exposure Time	15 s
Accumulations	20

Table 4.2: Measurement parameters used to acquire Raman spectra from vertical GaAs nanowires.

shown in Figure 4.5. The TO and LO modes for the 50 nm diameter nanowire sample are well fit to Lorentzian lineshapes with center frequencies of ω_{TO} = 291 cm^{-1} and ω_{LO} = 267.5 cm^{-1}, and spectral widths of 3 cm^{-1} and 3.3 cm^{-1}, which are in excellent agreement with the values for bulk GaAs crystals at T = 300 K. The SO peak was centered at 286.3 cm^{-1} with a FWHM of 10 cm^{-1}. A well accepted expression for the SO frequency at room temperature as a function of cylinder size and dielectric constant is given by equation 2.13. For GaAs, values for dielectric constant, $\varepsilon_0 = 12.85$, and dynamic dielectric constant, $\varepsilon_\infty = 10.88$, are generally used in the calculations [24]. If the surrounding medium is taken to be air ($\varepsilon_m = 1$) then one obtains a value of 286 cm^{-1} for the frequency of surface phonons for a nanowire diameter of 50 nm at room temperature. Again, this value is in excellent agreement with the experimentally measured value of 286.3 cm^{-1}. Therefore, it can be concluded from the fitting parameters associated with each peak, that the 50 nm diameter sample did not experience any heating effects from the Raman laser and the nanowire temperature is 300 K for this sample. This confirms that the etched GaAs nanowires consist of a high quality zincblende structure.

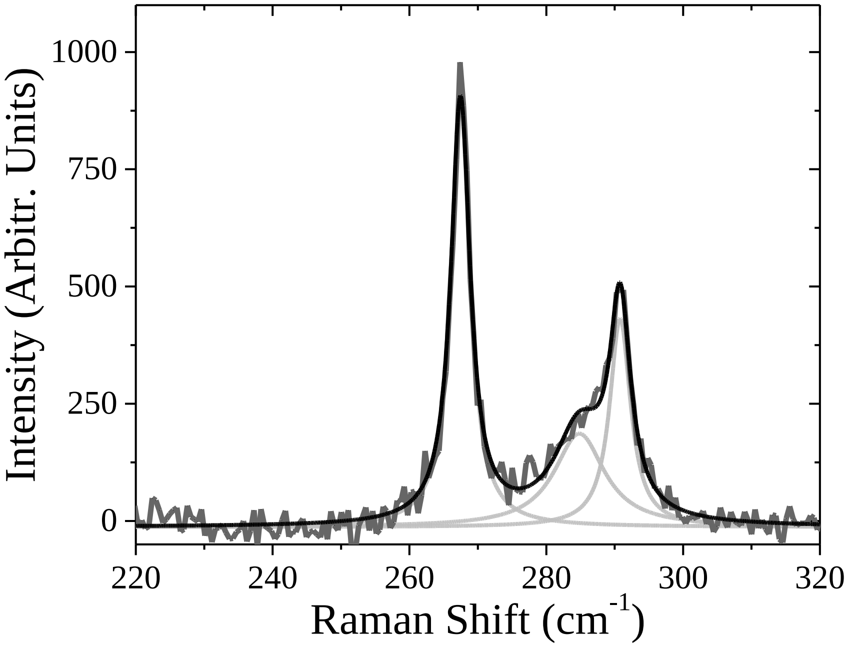

Figure 4.5: Spectral deconvolution of the Raman spectrum (dark grey trace) for the 50 nm diameter sample. A good fit (solid black line) is achieved by modeling the LO, TO, and SO modes as independent Lorentzian functions (solid grey lines).

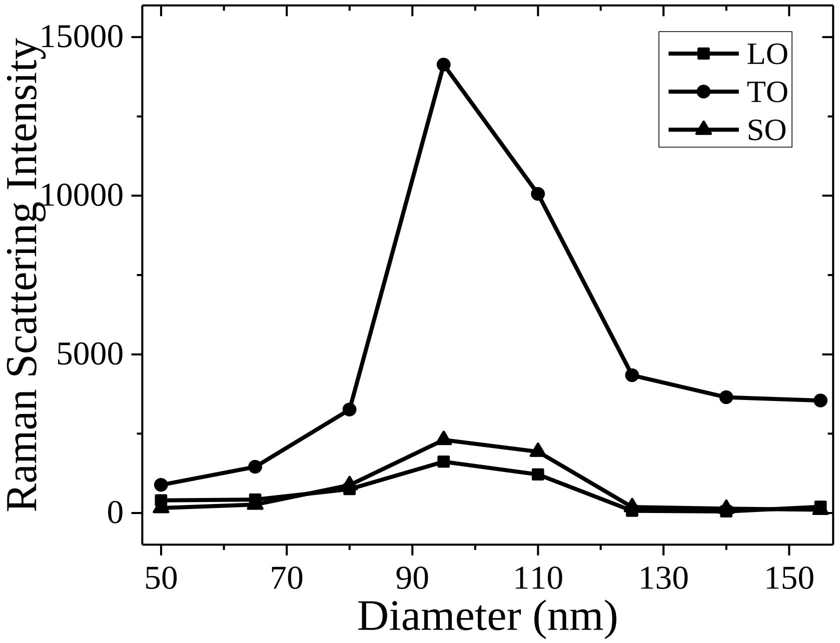

Figure 4.6: Peak intensities for LO, TO and SO phonons as the nanowire diameter is changed. A maximum in Raman scattering intensity occurs for the 95 nm diameter sample.

A similar analysis was performed for the other nanowire diameters. The scattering intensities, center frequencies, and FWHM of the TO and LO modes as a function of diameter are plotted in Figures 4.6, 4.7, and 4.8 respectively. Interestingly, a highly diameter dependent non-monotonic red-shift and spectral broadening are seen for both modes. The maximum red shift and broadening is observed for the 95 nm diameter sample, which also has the highest Raman scattering intensity. As was the case of Si nanowires, the increased intensity results from the strong excitation of the HE_{11} mode [7,19,47]. It is clear that phonon confinement is not responsible for the observed broadening or downshift of the Raman scattering frequencies. Instead the results suggest there is strong diameter dependent heating effect in GaAs nanowires which results from the

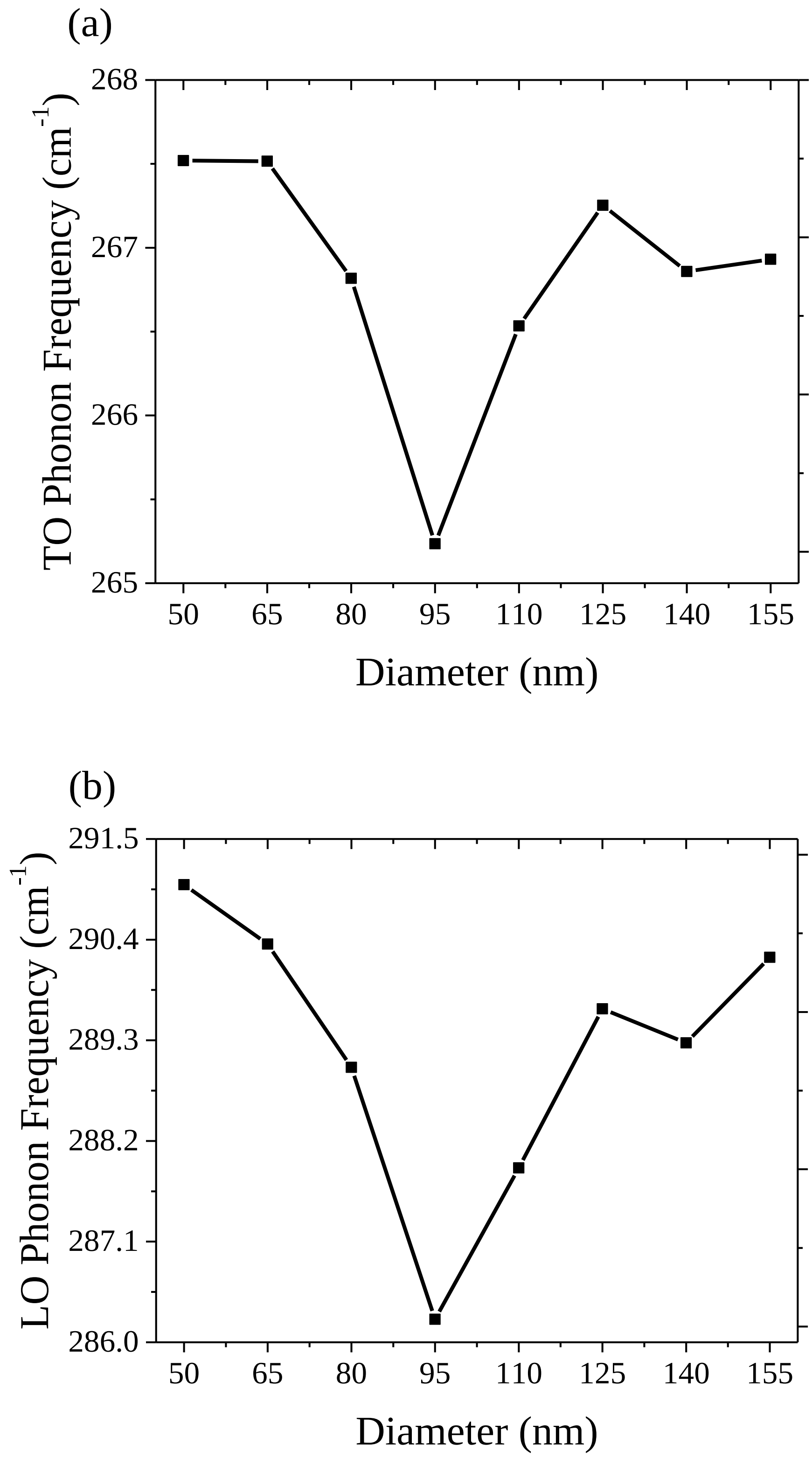

Figure 4.7: TO (a) and LO (b) phonon frequencies versus GaAs nanowire diameter.

excitation of the HE_{11} mode as seen below in Figure 4.8. This effect can be exploited to create devices for both photo-thermal and photo-thermoelectrical applications. These ideas are examined in the following chapter.

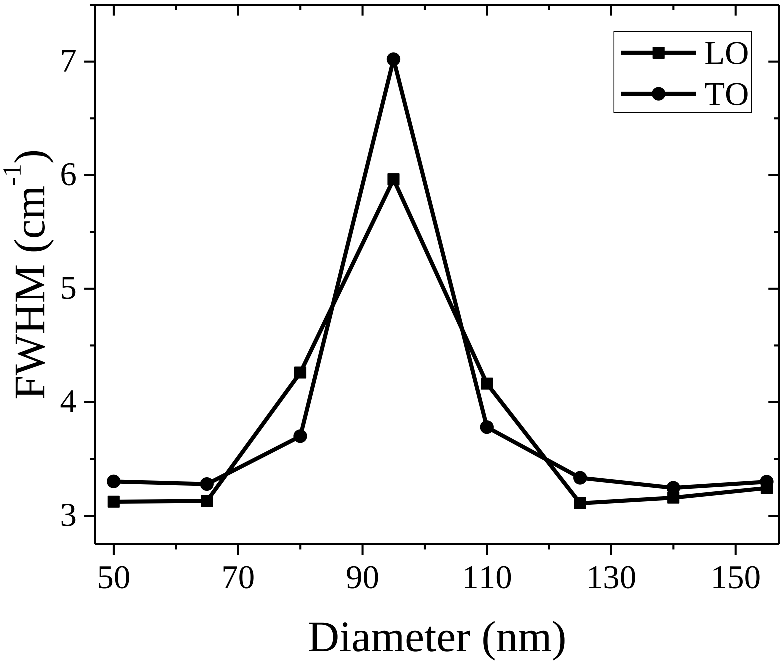

Figure 4.8: FWHM for LO and TO phonon Raman lines with changing diameter of nanowires. FWHM of SO phonon was consistently found to be ~ 10 cm^{-1} over the diameters studied.

To gain further insight the waveguiding effect of GaAs nanowires, the local electric field intensity was examined using finite difference time domain (FDTD) simulations involving the complete structure using a commercial software, Rsoft. The 1 µm long nanowires were oriented in the z-direction on top of a semi-infinite GaAs substrate, and a 532 nm plane wave polarized along the x direction was used to simulate the incident light field. Periodic boundary conditions were used in x and y directions so that the array can be simulated by a single unit cell. Perfectly matched layer

(PML) boundary conditions were also employed to reduce spurious reflections. Values for the optical constants, n = 4.13, and k = 0.34 for GaAs at 532 nm were used. Simulated irradiance distributions for three nanowire diameters of 50 nm, 100 nm and 150 nm are shown in Figure 4.9 (a)-(c). From the figure alone, it is clearly evident that the 100 nm diameter nanowire sample generates the highest electric field enhancement, as well as a strongly guided HE_{11} mode [7,19,47]. The large electric field enhancement is also responsible for the large Raman scattering enhancement of the TO, LO, and SO phonon modes seen in Figure 4.6, where a factor 14 increase in Raman scattering intensity is observed for the 95 nm sample relative to the other diameters studied. This result is similar to our previous work on the Raman enhancement properties of vertically etched silicon (Si) nanowire arrays, where it was demonstrated that Raman scattering intensity from the first-order phonon mode in the diamond lattice of Si can be increased by a factor of 15 by tuning both the diameter and pitch of the nanowires in the square lattice [27]. Figure 4.9(d) plots optical absorptance for an incident wavelength of 532 nm, in both 500 nm and 1 μm long GaAs nanowires, for various diameters ranging from 50-175 nm. Maximum absorption is seen for the 95 nm diameter sample, in agreement with the experimental results. Interestingly, it was also determined that most of the optical power is absorbed within the first 500 nm.

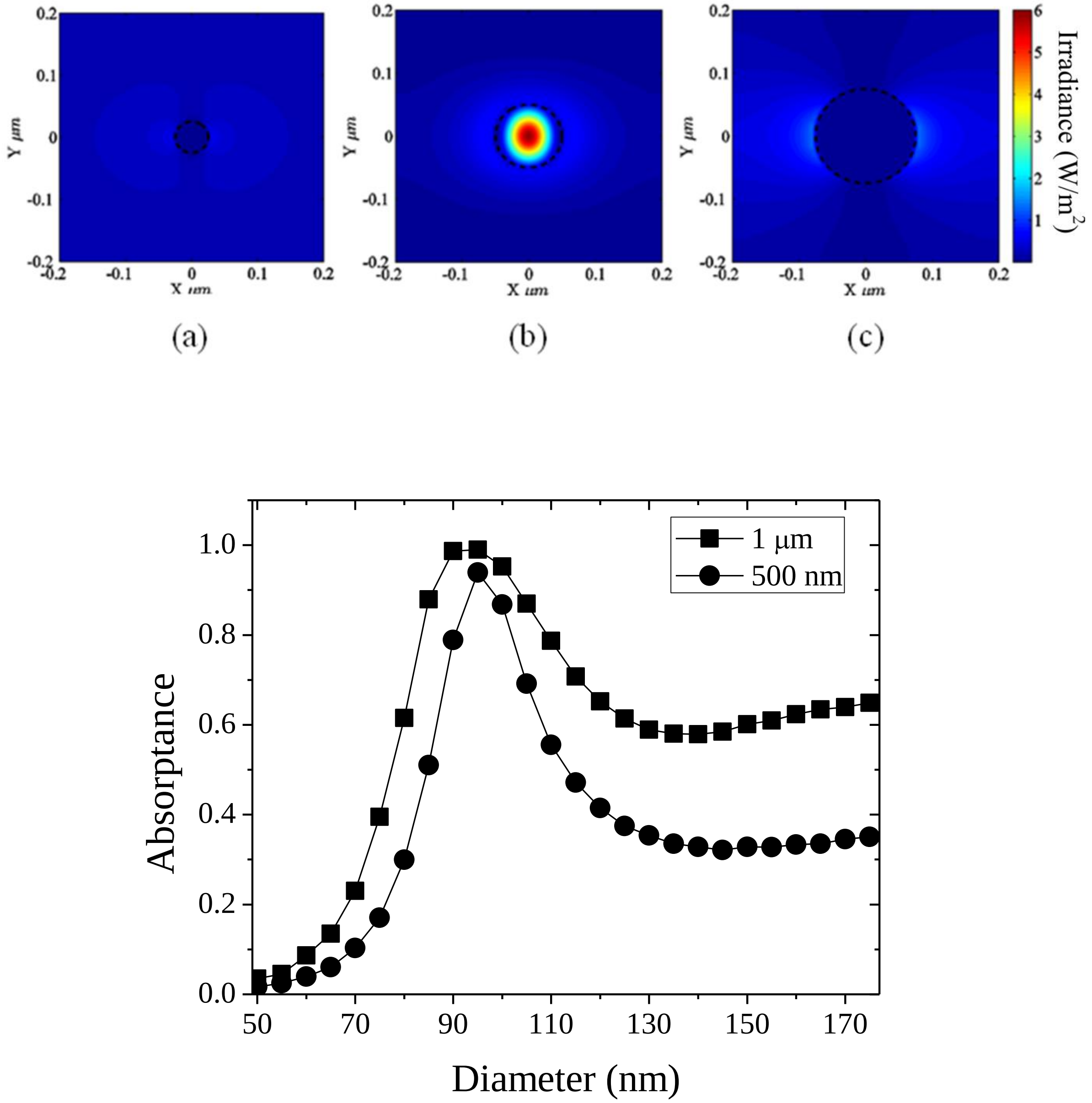

(d)

Figure 4.9. Irradiance distribution for three different nanowire diameters of (a) 50 nm, (b) 100 nm, and (c) 150 nm. The distributions were taken at a cross-section 100 nm into the nanowire. (d) Absorptance at a wavelength of 532 nm in nanowires of different diameters. The black squares represent absorption over a length of 1 μm, while the circles represent absorption within the first 500 nm of the nanowire.

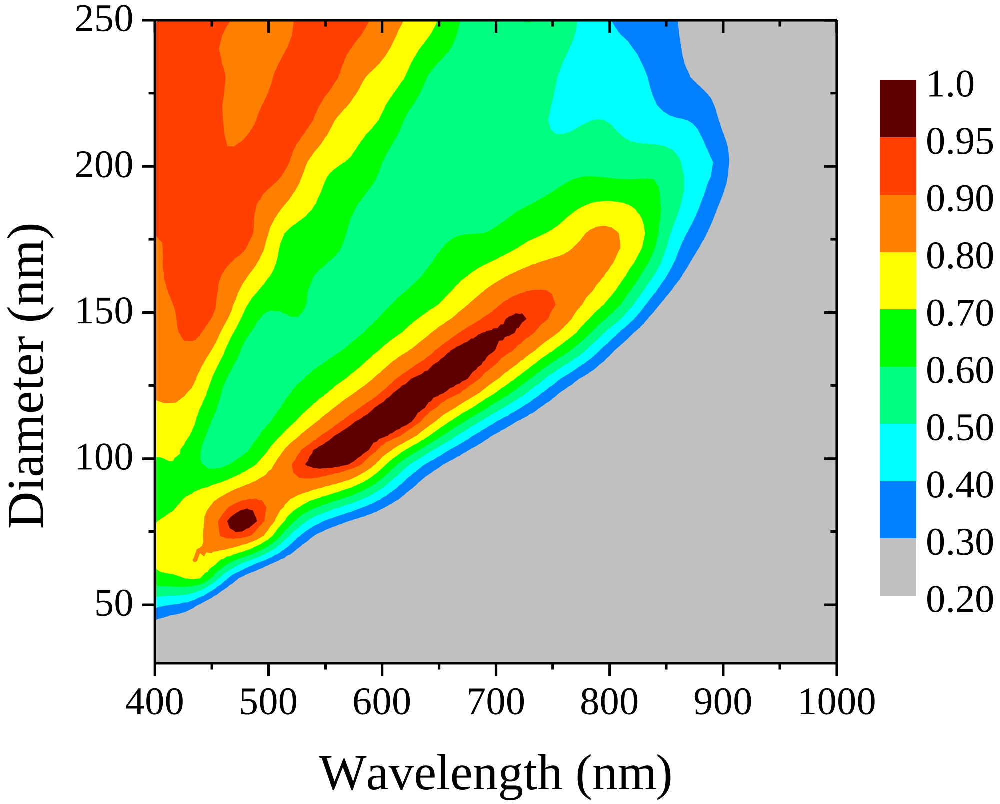

Figure 4.10: Simulated absorptance for 1 µm long nanowires for different incident wavelengths and diameters. The nanowires were arranged in a square lattice with a pitch of 400 nm. From the contour plot it is seen that larger diameter nanowires (> 150 nm) are more effective at absorbing wavelengths below 500 nm, whereas smaller diameter nanowires are more effective for absorbing wavelengths above 500 nm.

As mentioned earlier, the optimal diameter for maximum temperature change will be dependent on the incident wavelength. For applications involving either single or multiple wavelengths, or broadband absorption, simulated electric field intensities or absorption profiles could be used to determine the feasibility of a given design for a PTE device. Once again, using FDTD simulations, the optical absorption for 1 µm long GaAs nanowires at different incident wavelengths (up to the bandgap of GaAs) and for various nanowire diameters (50 nm - 250 nm) was calculated to create a contour plot in Figure 4.10. For each 1 nm change in incident wavelength, the optimal diameter shifts by 0.29 nm in a near linear relationship over a wide wavelength span from 450 nm to 800 nm. For diameters larger than 150 nm, a second absorption peak occurs due to excitation of higher order modes. The contour plot suggests that for an incident wavelength of 633 nm, the resonant diameter would shift to 120-125 nm. In other words, a sample with nanowires falling into this diameter range should produce the highest scattering intensity. To confirm this, Raman measurements were performed using an excitation wavelength of 633 nm, for diameters ranging from 80 nm to 240 nm. The Raman scattering intensity per unit volume versus nanowire diameter is plotted in Figure 4.11. A clear shift in the resonant diameter to 125 nm is seen, and confirms that excitation of the HE_{11} mode is responsible for the observed scattering intensities.

In summary, a confocal Raman study was carried out on vertical GaAs. It is conclusively shown that Raman scattering can be used to verify the zincblende nature of the etched nanowires arrays. Furthermore, in keeping with the results in section 4.1, Raman scattering is also readily able to identify the resonant diameter associated with wavelength of the incoming laser light and thus can also be used to study the electric field distributions within the nanowires. The resonant behavior suggests that local temperatures can be tuned by simply adjusting the nanowire diameter around the 95 nm diameter for the input wavelength of 532 nm. More generally, for each optical wavelength, there exists a certain resonant diameter. One can potentially realize lateral temperature gradients by tuning the nanowire diameter allowing one to make planar PTE devices. Optical

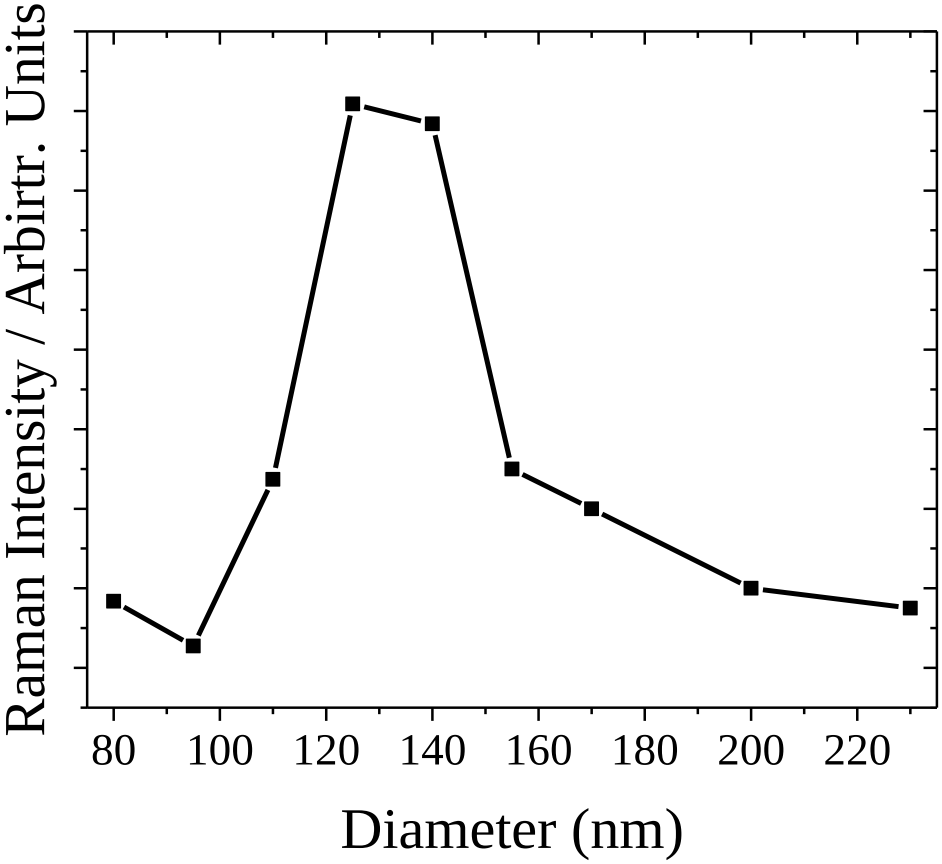

Figure 4.11: Peak intensities for LO, TO and SO phonons as the nanowire diameter is changed. A maximum in Raman scattering intensity occurs for the 125 nm diameter sample.

coupling into vertically arranged nanowires also has important implications for next generation GaAs based PTE devices, where it is important to maximize the amount of heat that can be generated from the photon flux which is used to power the device as the optimal diameter(s) will depend on how well the incident wavelength(s) couple(s) into the nanowires. The following chapter examines the temperature increases that can be realized by using strong waveguiding in nanowires.

4.3 Amorphous Silicon Nanowires

So far, crystalline Si and GaAs nanowire structures were examined. In order to contrast those results, this section is concerned with Raman scattering from amorphous silicon nanowires. The Raman bands associated with amorphous silicon are readily distinguished from crystalline silicon. A Raman spectrum from the bulk a-Si layer prior to nanowire fabrication, and spectra of a-Si nanowires after the etching process are shown in Figure 4.12 as the open grey circles. It is observed that the Raman spectra are quite consistent, and only changes in scattering intensity are observed as the diameter is varied from 75 nm to 125 nm. Bulk amorphous silicon has three phonon peaks appearing in the 250 cm^{-1} to 600 cm^{-1} range. In contrast to crystalline Si, these signals are much broader (~ 50 cm^{-1} - 100 cm^{-1} wide). Figure 1 also shows the deconvolution of each spectrum into three Gaussian peaks; one for the TO mode (red trace), one for the LO mode (green trace), and one for the LA mode (blue trace). The overall fit to each spectrum is plotted as a solid black line. The main feature is a broad peak centered at 480 cm^{-1}, and corresponds to the TO vibrational mode [20]. The other two peaks are the LO and LA modes centered at ~ 400 cm^{-1} and 300 cm^{-1} respectively [21].The FWHM, $\Delta\omega$, of the TO phonon peak has previously been related to the average Si-Si-Si bond angle variation $\Delta\theta_b$by [50],

$$\Delta\omega = 15 + 6\Delta\theta_b \tag{4.1}$$

The values for $\Delta\omega$ and ω from the fitting process for the TO mode, and the calculated values for $\Delta\theta_b$ for all nanowire diameters are tabulated in Table 4.4. The FWHM of the TO mode for the bulk sample was found to be ~ 76 cm^{-1}, and agrees well with the values reported in the literature for this material [50]. Interestingly, a-Si nanowires show a ~ 12 cm^{-1} reduction in the width of this peak. For the bulk a-Si sample $\Delta\theta_b$ = 10.1 °, and for the nanowire samples, this bond angle variation is

Measurement Parameter	**Value**
Laser Wavelength/Power	533 nm / 0.6 W
Laswer Power Density	6 W/mm^2
Exposure Time	5 s
Accumulations	15

Table 4.3: Measurement parameters used to acquire Raman spectra from a-Si nanowires.

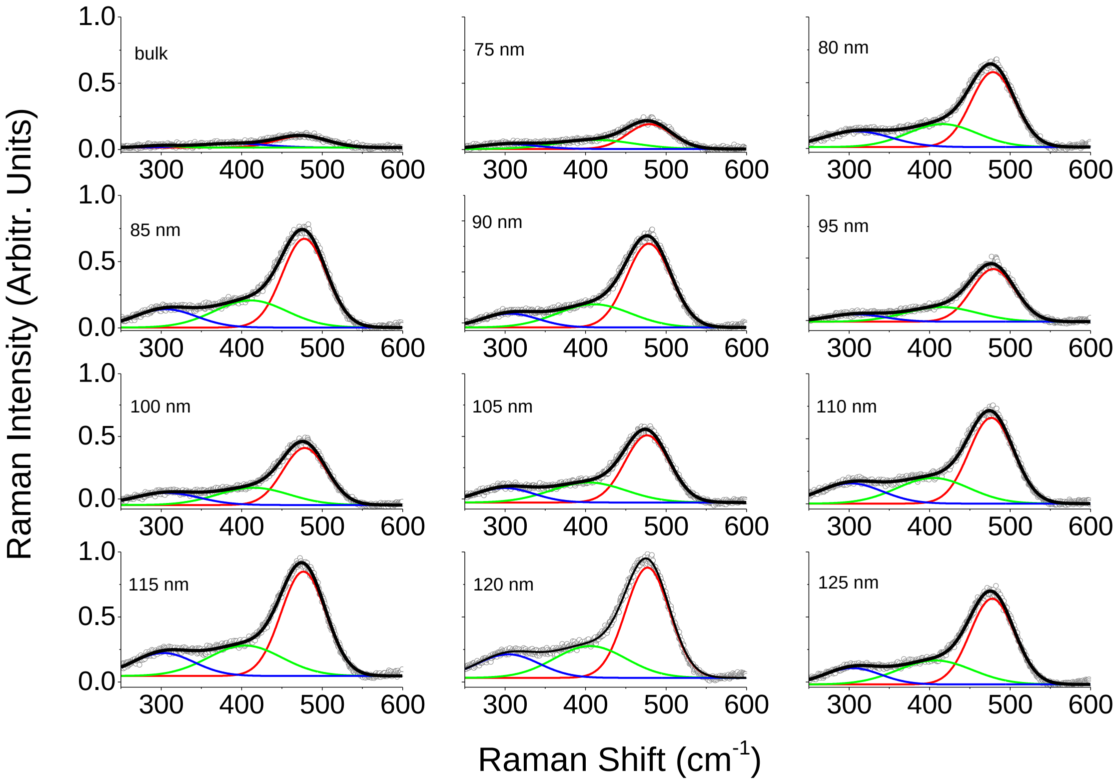

Figure 4.12. Raman spectra (gray circles) from a-Si nanowire arrays for diameters ranging from 75 nm to 125 nm and the thin-film starting layer. All spectra are well fit (solid black line) to three peaks representing scattering from the TO (red), LO (green), and LA (blue) phonon modes.

Diameter (nm)	**FWHM (cm^{-1})**	**Frequency (cm^{-1})**	**RIV**	**$\Delta\theta_B$**
BULK	76.1	477.5	0.19	10.3
75	64.5	479.6	0.36	8.3
80	64.2	478.6	0.96	8.2
85	64.4	477.8	1	8.2
90	64.9	478.6	0.88	8.3
95	63.5	478.9	0.50	8.1
100	63.7	478.3	0.49	8.1
105	64.5	476.3	0.53	8.2
110	65.2	476.6	0.59	8.4
115	65.2	476.7	0.66	8.4
120	64.4	477.0	0.64	8.2
125	64.5	477.7	0.46	8.2

Table 4.4: Values for the FWHM, centre frequency, and RIV of the TO mode from a-Si nanowires.

reduced to ~ 8° - 8.4°, suggesting a reduction the amorphous nature of the material. However the peak position of the TO mode has not been significantly affected, and therefore the nanowires are still be considered to be amorphous in nature. The reduction in bond angle variation can be understood by recalling that c-Si is made up of a tetrahedral network of covalent bonds, and that this is a result of minimizing free energy. Accordingly, the bonds in the a-Si network will always tend towards making tetrahedral bond angles. Since the free energy of c-Si is lower than a-Si, and given an extremely long period of time, a sample of a-Si would eventually crystallize and become c-Si even at room temperature, and raising the temperature speeds up the process . In practice, this in unlikely, and usually a transformation to a polycrystalline state is observed when heating is induced. Therefore it is likely that the reduction in bond angle variation was the result of the baking the photoresist at 180 °C.

More interestingly, the Raman enhancement effect we have previously observed in crystalline Si [26] and [27] GaAs nanowires is also observed in a-Si nanowires. The Raman scattering enhancements are the result of optical confinement of the incoming light field within the cores. This funneling effect of the incoming light field increases the irradiance on each nanowire, which leads to increased Raman scattering intensities. For the diameter range studied, the increased irradiance results from the excitation of the HE_{11} mode. Particularly, the highest Raman scattering intensity occurs when the optical confinement of the incident field is maxmized, and the strongest excitation of the HE_{11} mode results. This resonant behaviour only occurs for vertical nanowires, and where the wavevector of incoming lightfield is parallel to long axis. Accordingly, apart from semiconductor material composition and phonon confinement effects, Raman measurements also provide information on optical waveguiding properties of nanowire arrays. When performing UV-Vis absorptance measurements care must be taken in order to account for scattered light, which is not always easy, especially from periodic structures such as a nanowire array. A Raman measurement does not suffer from this, and acquiring a spectrum is quite straightforward. As the nanowire diameter increases, the material volume within the laser spot also increases and must be accounted for in order to quantify the amount of enhancement. By calculating the Raman scattering intensity per unit volume (RIV) versus nanowire diameter, one is able to identify the diameter that resonantly excites the HE_{11} mode for the given input wavelength.

To confirm this proposal, the intensity of the TO phonon mode per unit volume of nanowire material was measured for two incident wavelengths of 532 nm and 633 nm. As shown in Figure 4.13, the 85 nm diameter sample produces the highest RIV for an incoming laser wavelength of 533 nm. Correspondingly, the 120 nm sample produced the highest RIV when the incident wavelength was changed to 633 nm. Since the Raman intensity measured during the experiment has arbitrary units, the calculated RIV values are normalized with respect to highest value. Therefore the resonant diameters were assigned an RIV value of unity. At the resonant diameter an REV 20 over the a-Si thin film at 533 nm was measaured. At 633 nm, the REV over bulk increases to nearly 200. In comparison, Si nanowires have shown REV values of up to 840. We have previously shown that the RIV from Si nanowires can be modelled as [27],

$$I/_{V} = \kappa \frac{\mathrm{I}_{overlap}}{A^2} T_i T_R \qquad 4.2$$

Here I is the intensity of the Raman scattered light, V is the volume of the nanowire, A is the cross-sectional area of the nanowire, T_i and T_r are the transmittances through the nanowires for the incident and Raman wavelengths, and κ is an empirically determined factor. The large differences in REV at different wavelengths is mainly the result of differences in transmittance. The

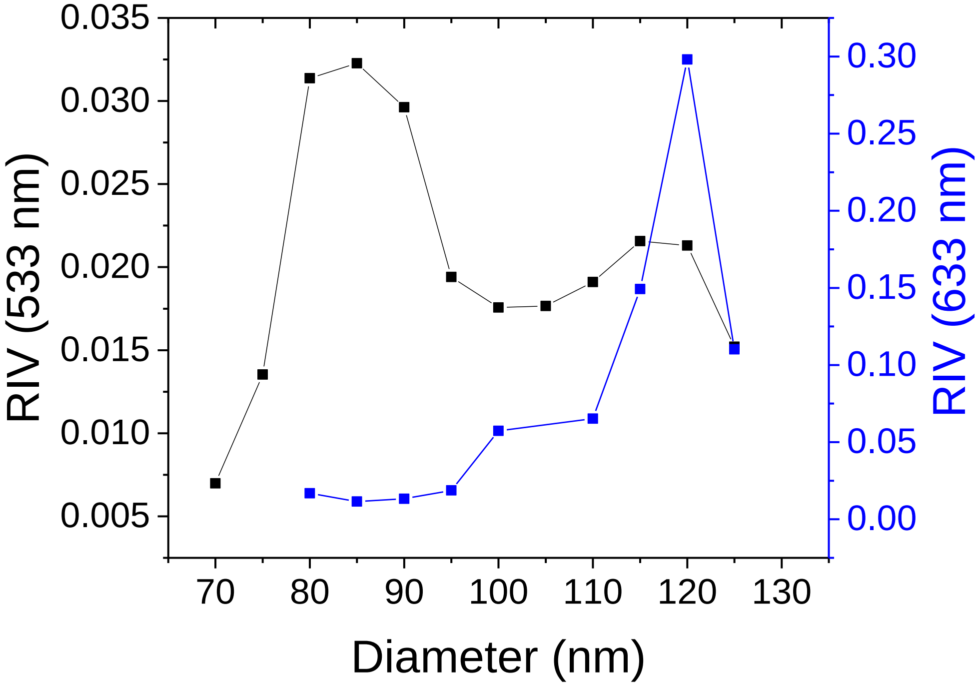

Figure 4.13: TO scattering intensity per unit volume from a-Si nanowires with diameters ranging from 75 nm to 125 nm. A clear resonant effect is observed for the 85 nm and 1250 nm diameter sample. In keeping with the results of our previous studies, this behaviour is the result of resonant excitation of the HE_{11} mode.

transmittance depends on the absorption coefficient, *k*, of the nanowire material, and the wavelength of incident light. According to equation 2, lower absorption coefficients lead to increased Raman scattering. Referring to Figure S1 in Supplementary Information, the absorption coefficient of a-Si at 533 nm is 0.46, and at 633 nm $k = 0.09$. Along these line the absorption coefficient of c-Si at 633 nm is 0.02. The results presented here from a-Si nanowires confirm that highly absorbing nanowire materials generate much lower REV values.

The shift in resonance is in keeping with the idea that for a given incident wavelength there is a specific diameter that will resonantly excite the HE_{11} mode. It is instructive to note that the degree of excitation of the HE_{11} mode for a given photon energy does not depend solely on the diameter of the nanowire. In general, the degree of excitation depends on the diameter of the nanowire, and also on the refractive index of the nanowire material and surrounding medium. The refractive index of the a-Si starting layer was measured using a FilmMetrics F-40 thin film analyzer. For an incident wavelength of 533 nm, values of n = 4.8 and k = 0.46 were measured, and at 633 nm, the measured values were n = 4.4 and k = 0.09. Finite difference time domain (FDTD) simulations can be used to determine the average electric field intensity within the nanowire core versus diameter for a given incident wavelength and material, the result of which can be used to identify the resonant diameter. If we assume that the optical constants of the nanowires remain unchanged after the fabrication process, then computer simulations suggest that the resonant diameters for a-Si nanowires are 80 nm and 105 nm for incident wavelengths of 533 nm and 633 nm, respectively. Even though the difference is small (5 nm) between the measured and simulated result at 533 nm, there is a 20 nm difference between the results at 633 nm. Since the refractive index determines the resonant diameter, the difference between resonant diameters determined from experiment and simulation suggests that the nanowire refractive indices have changed relative to the thin film starting layer.

Referring back to Table 1, the average bond angle variation between neighbouring Si atoms, $\Delta\theta_b$, is reduced for nanowires by ~ 3°. Strictly speaking, this means that the nanowires are less amorphous than the thin film starting layer. Furthermore it is well know that crystalline Si (c-Si), and a-Si have different optical constants. Therefore as the bond angle variation is reduced, the optical constants of the material must begin to shift towards the values associated with c-Si. That is, *n* is expected to shift towards 4.2 from 4.8 at 533 nm, and from 4.4 to 3.9 at 633 nm. In general, for wavelengths in the visible range, a reduction of refractive index is expected as $\Delta\theta_b$ is reduced. This can account for the difference observed between the simulated and measured values.

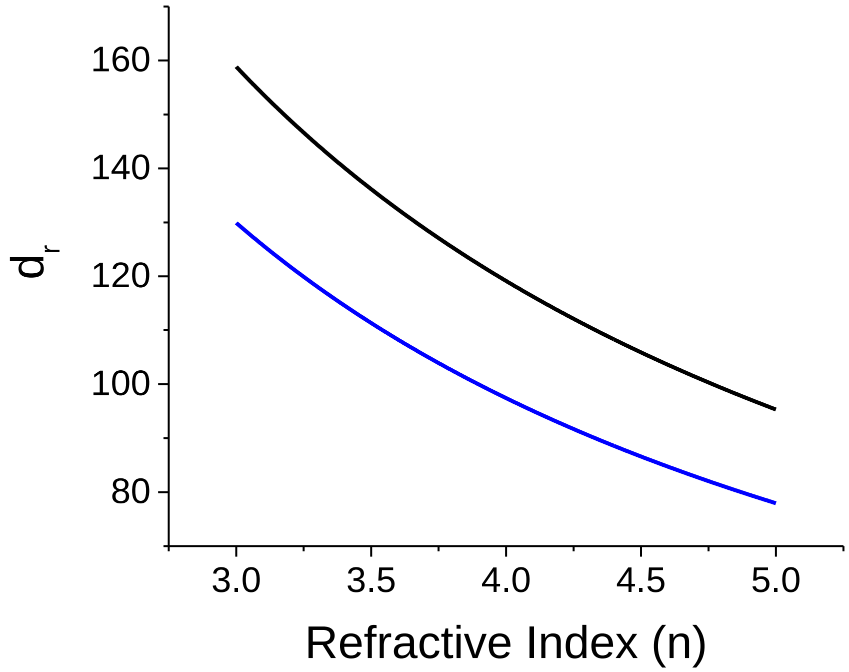

Figure 4.14: Resonant diameter which produces the highest optical confinement versus refractive index for incident wavelengths of 533 nm (blue) and 633 nm (black).

By varying the refractive index in the simulations, it becomes possible to gain insight into relationship between the resonant diameter and refractive index of the nanowire for a given wavelength, and therefore estimate the refractive index of the nanowire. Figure 4.14 plots the simulated resonant diameter, d_r *versus* refractive index *n* for two incident wavelengths of 533 nm and 633 nm. Also shown as points are the resonant diameters measured using Raman spectroscopy. By combining the Raman measurement, with computer simulations, the estimated refractive indices of the a-Si nanowires are 4.6 at 533 nm, and 3.95 at 633 nm. Therefore, with the aid of computer simulations, the resonant behaviour of TO phonon intensity as a function of nanowire diameter can be used to estimate the refractive index of the nanowire material or surrounding medium if one or the other is known. The estimated values for a-Si nanowires are consistent with the idea that as the bond angle is reduced, the refractive index will also decrease. Interestingly, the 3˚ reduction in bond angle variation had more effect on the refractive index at 633 nm, which now is closer to the value of c-Si.

To conclude, amorphous silicon nanowires were studied with Raman spectroscopy, using two excitation wavelengths of 532 nm and 633 nm. One can identify the nanowire diameter that produces the strongest confinement of the incoming light field by determining which nanowire diameter produces the highest TO scattering intensity per unit volume. Furthermore, with the aid of computer simulations, the resonant diameters determined from Raman spectra can be used to estimate the refractive index of the nanowires. It was found that the refractive index of the nanowires is reduced at both 532 nm and 633 nm wavelengths relative to the a-Si thin film starting layer. The change in refractive index was attributed to reduced bond angle variation present in Si network of the nanowires. In this connection, Raman spectroscopy can be used to determine the physical and optical properties of vertical a-Si nanowire arrays.

CHAPTER 5

Photo-Thermal Properties of Vertical GaAs Nanowires

Introduction

Recently, there has been interest in nanostructures which efficiently convert incident light into heat for photo-thermal-electrical (PTE) applications. Current applications include PTE devices for energy conversion [51-53], bio-implantable electronics [54], and laser therapeutic agents for selective elimination of microorganisms [55]. In PTE applications, light is converted to heat, and then converted to electricity, presenting an additional method to fully utilize solar energy. The thermoelectric figure of merit, ZT = $\sigma S^2 T/\kappa$, determines the efficiency of a given thermoelectric (TE) device. Here, S is the Seebeck coefficient, σ is the electrical conductivity, and κ is the thermal conductivity. Naturally, materials that possess both a high electrical conductivity and a low thermal conductivity are of particular interest for use in thermoelectric devices as this would lead to the highest values of ZT. Additionally, PTE applications must efficiently use incoming light to generate heat. As such, there has been an increased attention towards materials which efficiently absorb light and have low thermal conductivity. For example, enhanced PTE conversion in tilted layered cobaltite thin films was demonstrated by using a carbon nanotube layer to increase optical absorption [56]. Another study has used the enhanced absorption of carbon nanotubes to develop a PTE converter for bioelectronic applications [54], which uses a low power laser source outside of the body to power an implanted device. Another structure which is of interest for efficient optical absorption is the one-dimensional semiconductor nanowire.

Reduced thermal conductivities relative to bulk semiconductors have been reported in semiconductor nanowires, and are being exploited for thermo-electric and photo-thermal applications [15-19]. Along these lines it has recently been shown that resonant light absorption, along with reduced thermal conductivities, can create significant local heating in GaAs nanowires [19], even for relatively low input power densities. Generally, for applications and spectroscopic measurements involving light, the ability to control and maintain the original crystal structure of the nanowire is arguably the most critical factor in determining whether a particular device will function as desired. This concept becomes particularly important when considering nanostructures based on the arsenide semiconductors, where it is well known that arsenic dissociates from the lattice and forms crystalline arsenic (c-As) when local temperatures exceed 878 K and 663 K for bulk gallium arsenide (GaAs) and bulk indium arsenide (InAs), respectively [57].

Firstly, it is of interest to understand the photo-thermal potential of vertical GaAs nanowires when resonant excitation of the HE_{11} mode is achieved. Secondly, it is crucial to understand how crystal structure or composition of vertical nanowires is modified under resonant optical excitation and what power densities vertical GaAs nanowires can support under these strong waveguiding conditions before structural changes begin to occur if these structures are to be employed in photo-thermal applications.

5.1 Enhanced Photo-Thermal Conversion

Currently, Raman spectroscopy remains one of the most powerful tools available to study photo-thermal conversion in semiconductor nanowires. The excitation laser can be used to locally heat the sample, and also acquire Raman spectra from the same location. When the local temperature of the sample increases, these phonon frequencies are shifted to lower values, and the line shapes experience spectral broadening due to anharmonic processes leading to thermal expansion of the GaAs lattice [27]. Additionally, for GaAs a well-established linear relationship that relates the TO and LO phonon frequency shifts to local temperature exists and is given by [18],

$$d\upsilon/dT = 0.016\ \mathrm{cm}^{-1}\ \mathrm{K}^{-1} \qquad 5.1$$

Thus to quantify the ability for GaAs nanowires to convert light into heat, one can measure the frequency shifts of TO and LO modes for different input power densities. The Raman spectrum associated with a (100) starting wafer exhibits only scattering from the LO phonon mode [24]. The etching process does not produce a discernible increase in LO scattering, but does produce a significant amount of TO scattering [19]. Therefore the measured temperatures associated with the LO and TO phonon shifts can be correlated to the average temperatures of top facets of the nanowires and sidewalls, respectively.

For Raman measurements where no local heating was desired, a power density of 0.8 W/mm^2 was used. Measurements were also performed with higher power densities of 20 W/mm^2, 40 W/mm^2, and 80 W/mm^2 to determine the effect of laser heating on the Raman spectra, and deduce changes in the crystal structure. For room temperature measurements, the exposure time for the detector and number of accumulations was varied accordingly to achieve a good signal to noise ratio. For higher laser power levels, the time evolution of c-As formation was recorded by acquiring single shot Raman spectra every 5 seconds. All single shot spectra were smoothed using a Svatzky-Golev filter.

In Chapter 4, it was shown there is a resonant wavelength at which the HE_{11} mode is excited for a given diameter of semiconductor nanowire. Along these lines, not only does this result in enhanced Raman scattering, but others have also shown that excitation of the HE_{11} mode results in increased absorption. In turn, the amount of heat an object can generate from light is strictly proportional to how much of the incoming light field is absorbed. In keeping with this, the results in Chapter 4 have suggested that resonant excitation can lead to local temperature increases in GaAs nanowire arrays. In this chapter the photo-thermal properties of nanowires with diameters ranging from 80 to 230 nm are studied in detail using a 633 nm laser excitation source. Table 5.1 lists the experimental details of the Raman experiments appearing in this section.

Measurement Parameter	**Value**
Laser Wavelength / Power	633 nm / 10mW
Laser Power Density	20 W/mm^2
Exposure Time	10 s
Accumulations	20

Table 5.1: Measurement parameters used to acquire Raman spectra from GaAs nanowires for the purposes of understanding their photo-thermal properties.

Calculated temperatures from the TO and LO phonon shifts observed in Figure 4.7 are plotted in Figure 5.1 using equation 5.1. Since the nanowires are vertically oriented with respect to the light source, it is expected that the top facets will heat up more. Scattering from the TO and LO modes are thought to be from the

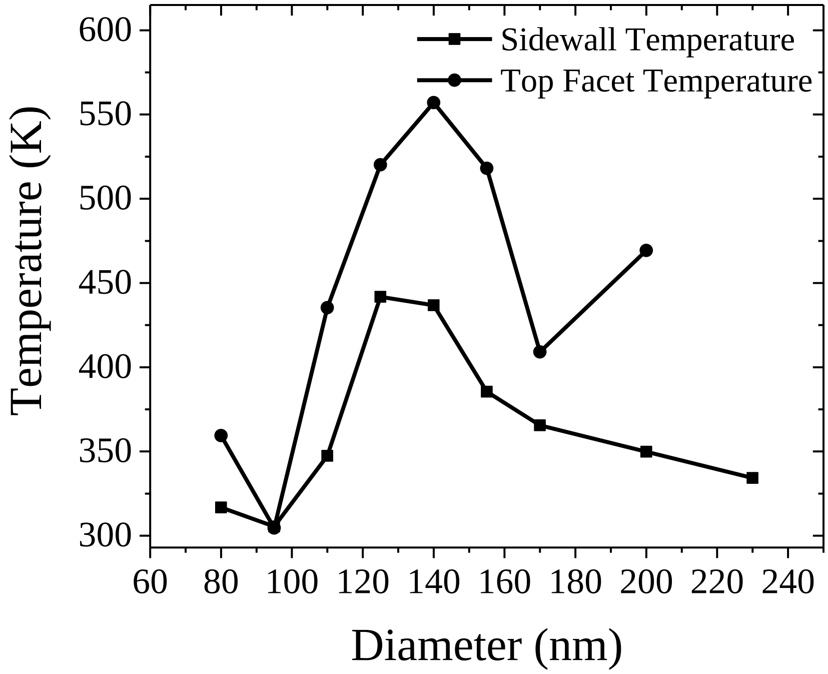

Figure 5.1: Measured temperature of the nanowire sidewalls and top facets versus diameter for an input power density of 20 W/mm^2. The temperature was calculated using equation 5.1.

sidewalls and top facets of the nanowires, respectively (as evidenced by the presence of the TO mode only after nanowire sidewalls are created, see Chapter 4). It is therefore expected that each nanowire will have a different local temperature on the top facet and sidewalls depending on the nanowire diameter. The dependence of the local nanowire temperature on the nanowire diameter is clearly seen in Figure 5.1, and demonstrates the use of photonic modes in achieving higher light induced temperatures. In previous studies involving heating in nanowires, the highest local temperatures are usually observed for the lowest nanowire diameters for a given input energy flux due to reduced thermal conductivities as the diameter decreases [14]. In contrast, this study confirms that by using vertically oriented GaAs nanowires with a diameter of 125 nm, more heat can be generated for the same amount of input light at a wavelength of 633 nm, and therefore smaller nanowires are not necessarily better. Specifically, temperature increases approaching 140 K at the top facets are realized for the diameter of 125 nm for an irradiance of 20 W/mm^2. As a comparison, a temperature increase of 50 K was observed in single wall carbon nanotubes embedded in polydimethylsilicate substrate for an incident intensity of 318 mW/mm^2 [54]. The large Raman scattering enhancement is an indication of strong electric field confinement within the nanowires, leading to higher temperatures. Previous Raman scattering studies on vertically oriented crystalline silicon nanowires arranged in square lattices [26, 27] have not shown any local heating, even at laser input intensities an order of magnitude higher than the one used in this study. This result suggests that lower thermal conductivities are seen in GaAs nanowires as compared to Si nanowires.

The resonant temperature behaviour suggests that local temperatures can be tuned by simply adjusting the nanowire diameter around 125 nm diameter, for an input wavelength of 633 nm. More generally, for each optical wavelength, there exists a certain resonant diameter. One can potentially realize lateral temperature gradients by tuning the nanowire diameter allowing one to make planar PTE devices. Optical coupling into vertically arranged nanowires also has important implications for next generation GaAs based PTE devices, where it is important to maximize the amount of heat that can be generated from the photon flux which is used to power the device as the optimal diameter(s) will depend on how well the incident wavelength(s) couple(s) into the nanowires.

The heating behavior of vertically etched nanowires was examined using Raman spectroscopy. A non-monotonic behavior in the nanowire temperature as a function of diameter was observed. As the diameter was increased to 125-140 nm, the nanowire temperature on the top facet and surface sidewalls increased to 520-557 K and 436-441 K, respectively. As the diameter was further increased to 155 nm, a decrease in temperature to 330 K occurs, therefore demonstrating that the temperature can be tuned via nanowire diameter. The increased heating is attributed to the vertical nature of the nanowires, which effectively creates an array of dielectric waveguides, into which the incident light field can couple resulting in the strong diameter dependent heating effect. For any nanowire based PTE device it is of paramount importance to maximize the amount of heat that is generated from a given incident photon flux. To this end, this study has shown that vertically oriented GaAs nanowires arranged in square lattices are able to generate various amount of heat for a given nanowire diameter and incident wavelength. These findings demonstrate that GaAs nanowires arranged in a photonic lattice can be used to optimize the photo-thermal effect. The diameter dependent nature of the effect opens up a new avenue for PTE devices using localized temperature gradients. In particular, it may be possible to realize PTE devices that use planar temperature gradients, rather than longitudinal ones.

5.2 Photo-Thermal Modification of GaAs Nanowires

As mentioned earlier, it is well known that GaAs thermally decomposed when temperatures exceed 878 K [57]. Currently, Raman spectroscopy remains one of the most powerful tools available to study changes in crystal structure or composition. The excitation laser can be used to locally heat the sample, and also acquire Raman spectra from the same location. Previous studies have shown that both horizontal GaAs and InAs nanowires can be locally modified by using a laser to heat the nanowire samples [20, 58, 59]. In these cases, single horizontal nanowires were studied, where the laser was focused onto the sides of the nanowires, and power densities on the order of 10^3-10^4

W/mm^2 were required to observe the formation of c-As. Interestingly, it has been shown that c-As was being formed in horizontal GaAs nanowires when local temperatures approach only 600 K, suggesting that the temperature required to induce oxidation and c-As formation is reduced significantly relative to bulk [20].

For horizontal nanowires, the incident laser beam causes continuous ablation of the nanowire material from the surface, leading to eventual severing of the nanowire [20, 21]. It is not clear how heating resulting from the absorption of the HE_{11} optical mode in vertical nanowires, which has maximum power density in the center of the nanowire [17], will affect the physical nature of the nanowires. For light trapping applications, and even spectroscopic measurements that involve vertically oriented GaAs nanowires, it is important that the salient features of this process are understood to prevent nanowire damage, and maintain device functionality. Currently, there is no information available in the literature which discusses the dissociation of arsenic from vertical GaAs nanowires, the threshold power densities associated with this process, or how the morphology is altered.

The formation of c-As is thought to arise from the interfacial solid-solid reaction, $As_2O_3(s) + 2GaAs(s) \rightarrow Ga_2O_3(s) + 4As(s)$ [60, 61]. In terms of Raman scattering, bulk c-As produces a TO phonon peak centered at 198 cm^{-1}, and an LO phonon peak at 257 cm^{-1}, and have already been observed in both horizontal GaAs and InAs nanowires which were locally heated using lasers [20,58,59]. It is crucial to understand how much irradiance a vertically oriented nanowire will support before structural modification takes place. To track the evolution of c-As under strong waveguiding conditions, the nanowires were exposed to the laser power densities of 20 W/mm^2, 40 W/mm^2, and 80 W/mm^2 in different parts of the array. Single shot Raman spectra were recorded every 5 seconds, over a span of 70 seconds, and are plotted in Figures 5.2, 5.3, and 5.4 for the three power densities. For an input of 20 W/mm^2, corresponding to a maximum local temperature `of 420 K, a weak emergence of the TO phonon mode of c-As centered at ~200 cm^{-1} is seen over time. Additionally a broad background covering the 200-250 cm^{-1} region starts to form, and is readily associated with amorphous arsenic (a-As) [20]. When the power level and maximum local temperature are increased to 40 W/mm^2 and 571 K, respectively, both the TO, and LO phonon mode of c-As centered at 243 cm^{-1}, begin to emerge and build up in intensity over time. Again the TO phonon emerges first and is seen within the first 5 seconds of exposure to the laser. Scattering from the LO phonon starts to emerge after 20 s, and also continues to increase in intensity over time. Upon raising the incident intensity to 80 W/mm^2, and local temperature to 923 K, a further increase in the amount of c-As formation is seen. Once again, the TO phonon mode of c-As appears prior to emergence of the LO phonon peak, which suggests that some structural re-ordering is occurring as the amount of c-As content increases.

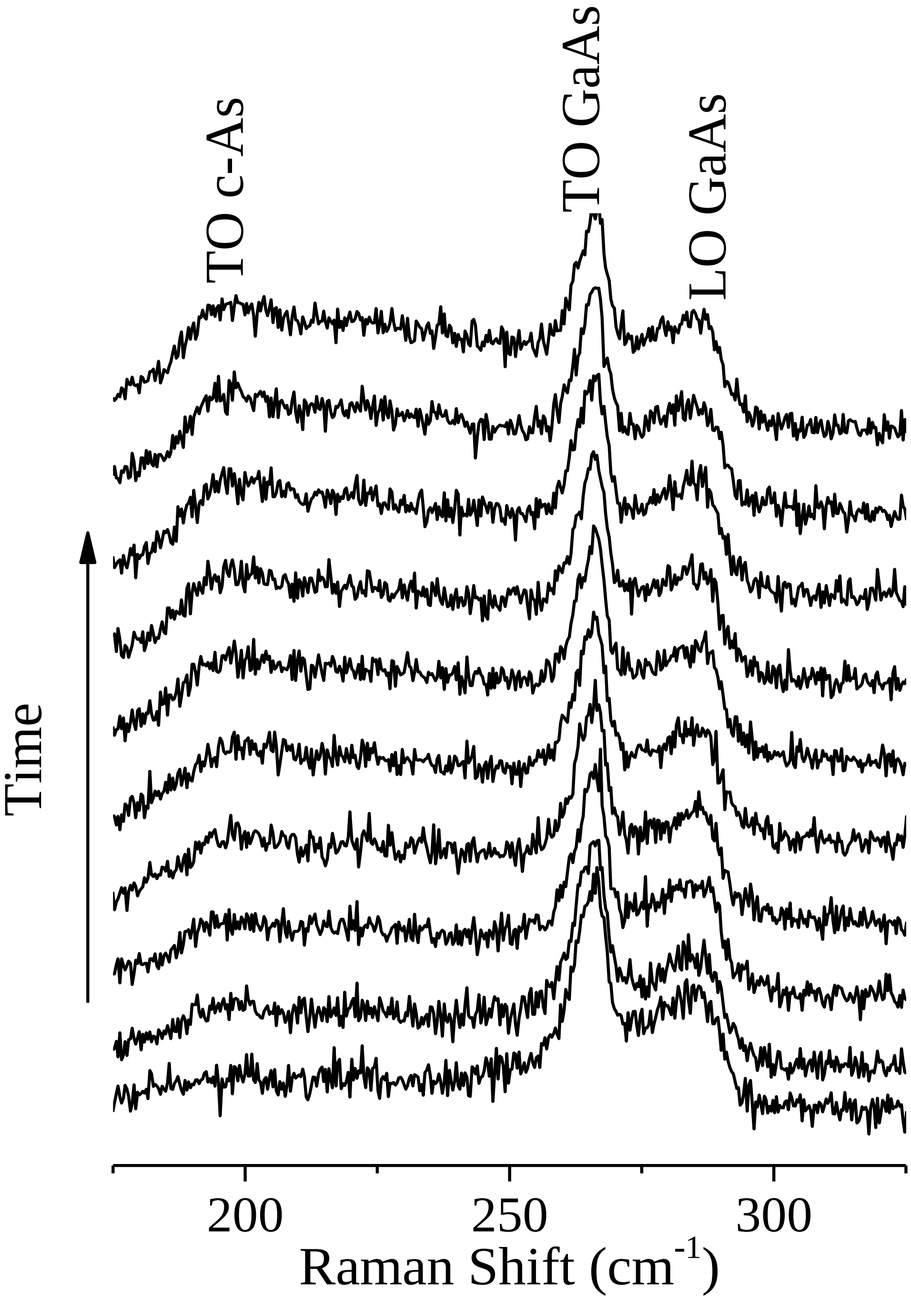

Figure 5.2: Time evolution Raman spectra recorded every 5s from vertically oriented, 125 nm diameter GaAs nanowires for an input power density of 20 W/mm^2.

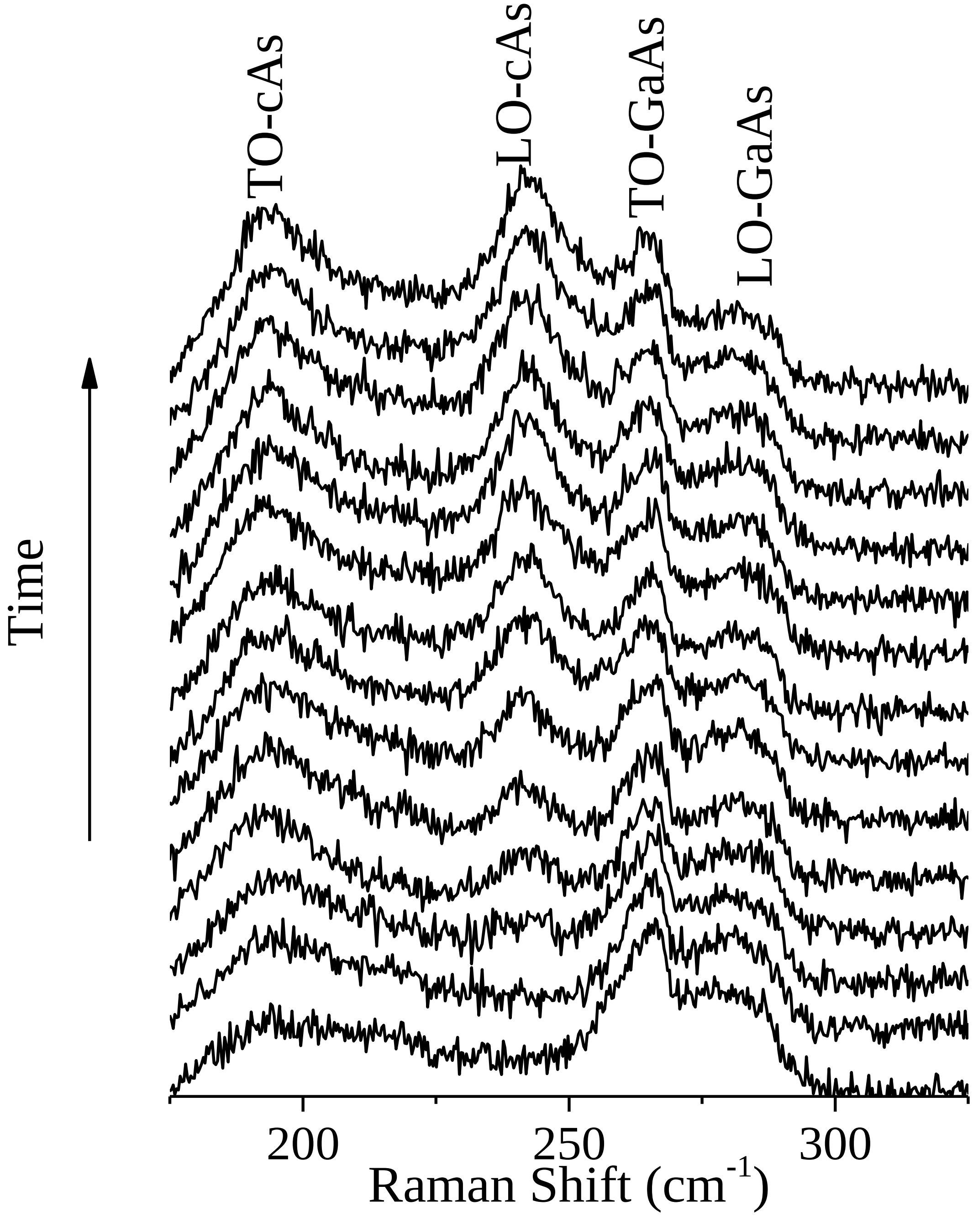

Figure 5.3: Time evolution Raman spectra recorded every 5s from vertically oriented, 125 nm diameter GaAs nanowires for an input power density of 40 W/mm^2.

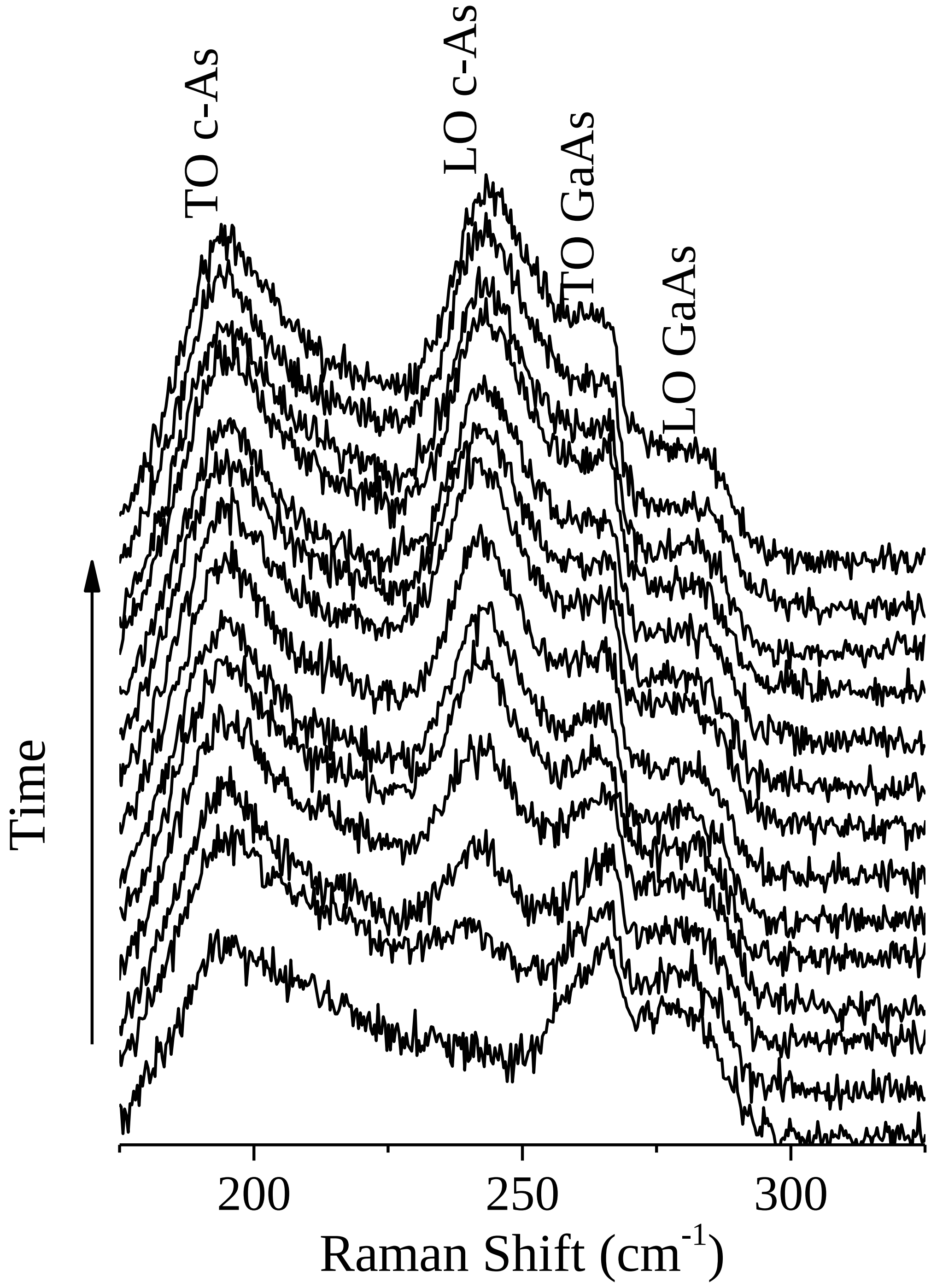

Figure 5.4: Time evolution Raman spectra recorded every 5s from vertically oriented, 125 nm diameter GaAs nanowires for an input power density of 80 W/mm^2.

The three most common allotropes of As are metallic gray, yellow, and black As. Gray arsenic is considered to be the most common form and crystallizes into a hexagonal rhombohedral crystal structure [62]. Specifically, it is a double layered structure, with each layer consisting of six-membered rings. Within a layer, the distance between As atoms is 2.504 Å, while the interlayer distance is 3.136 Å [62]. Assuming that gray As is formed during the laser annealing process, a tentative explanation for the appearance of the TO scattering peak prior to the LO scattering peak is that as As species form, only single layers of six membered interlocked rings form giving rise to only TO scattering. As the reaction proceeds, the layers become held together and begin to form the rhombohedral lattice, allowing for LO scattering to occur.

By tracking the LO phonon peak intensity as a function of time, it becomes possible to roughly determine when the solid-solid reaction described above is no longer occurring, since the LO scattering intensity should plateau as the reaction nears completion. This concept is seen in Figure 5.5, where the LO phonon intensity of c-As is plotted as a function of time for incident intensity of 80 W/mm^2 while the sample temperature was 923 K. After 70 seconds at 923 K, the LO phonon peak intensity begins to plateau with a time constant of ~ 17.2 s, indicating the reaction is being driven to completion, and that a finite amount of GaAs nanowire material has been modified.

After exposing the sample to power density of 80 W/mm^2 for 70 seconds to fully induce arsenic formation, the nanowires were measured once again at room temperature using a much lower laser power density of 0.8 W/mm^2, to confirm whether the changes in the Raman scattering spectrum of the sample are permanent. The result is plotted in Figure 5.6. In contrast to Figure 4.5 in Chapter 4, the Raman spectrum now consists of six peaks, three of which are the original LO, TO, and SO modes of GaAs (shown as dotted lines), and the remaining three belonging to the LO and TO modes of c-As, and scattering from a-As (shown in solid lines). The center frequencies for the

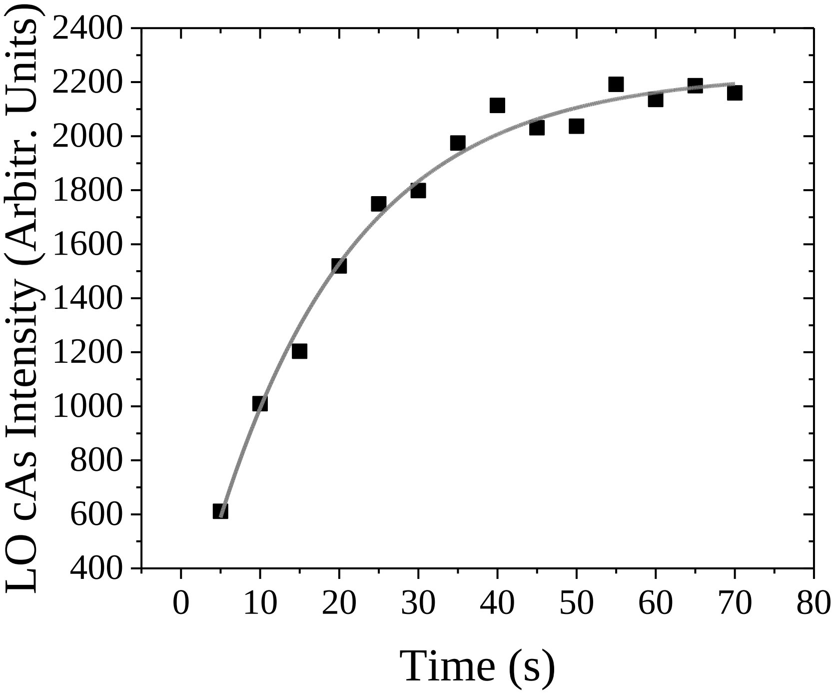

Figure 5.5: Time evolution of the LO phonon peak of c-As. The intensity begins to plateau after ~70 s, with a time constant of ~ 17.2 seconds.

TO and LO modes of c-As were found to be 258 cm^{-1} and 200 cm^{-1}, and agree well with the values quoted in the literature [20, 58-60]. Amorphous arsenic is also present, and appears as the broad peak centered at 226 cm^{-1}. Thus it can be concluded that both c-As and and a-As formation in vertically oriented nanowires does occur and the structural changes are clearly visible by comparing the Raman spectra before exposure in Fig. 1b to after exposure in Fig. 4e. Clearly, heating due to resonant waveguiding reduces the power density which a vertical GaAs nanowire can support by three orders of magnitude before permanent changes to the crystal structure take place.

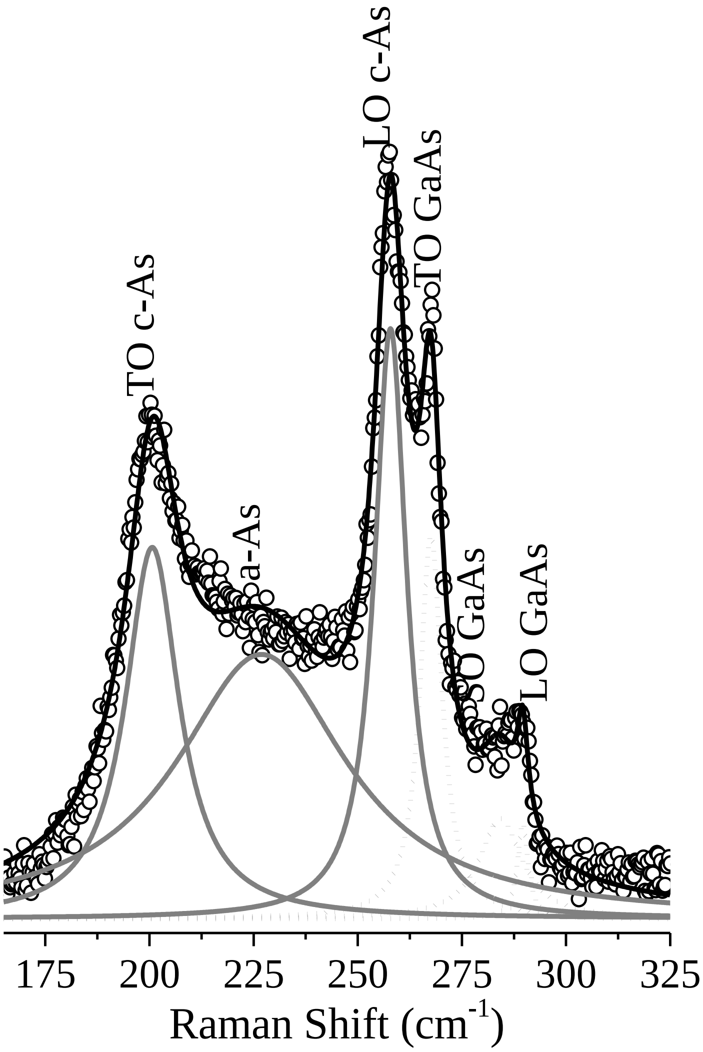

Figure 5.6: Raman spectrum taken at a power density of 0.8 W/mm^2 after the sample was exposed to elevated temperatures. Three new peaks corresponding to the TO phonon of c-As at 200 cm^{-1}, the LO phonon of c-As at 258 cm^{-1}, and scattering from a-As centered at 226 cm^{-1} are observed.

Although Raman scattering is able to provide information on the structural changes occurring in the nanowire array, it cannot provide information with respect to physical appearance of the altered nanowires. Given a high enough temperature, As species begin to evaporate from the surfaces of horizontal InAs nanowires, leading to continuous shedding of nanowire material, resulting in decreased Raman scattering intensities and eventual severing of the nanowire [58, 59]. However, for vertical nanowires, absorption of the HE_{11} mode is the heat source, which would effectively heat the nanowire from the inside out, and it is completely unknown what kind of structure is created if evaporation is induced.

To further understand and see how the nanowires are modified when very high temperatures are realized, TEM investigations of FIB cross-sectional samples were performed. To prepare a suitable sample, an area of ~ 100 μm^2 was exposed to 1 kW/mm^2 of laser power. The laser used was not integrated with the Raman system, and therefore sample temperatures cannot be measured through the phonon frequency shifts. A HAADF image of the FIB lamella, containing nanowires from both inside and outside of the laser exposed area, is shown in Figure 5.7. HAADF imaging is sensitive to both the atomic number and local thickness, and darker regions seen in the image correspond to areas which contain less material. Interestingly, the vertical nature of the nanowire is maintained, with the upper portion becoming a hollow nanotube, while the nanowire base and Al/Cr mask remain intact. As one moves towards the edge of the laser annealed area where the laser intensity rapidly falls off, a concomitant decrease in amount of hollowing of the nanowire is observed. Outside of the annealed area, an unaltered nanowire is seen, and therefore the hollowing of the nanowire was not the result of the milling process.

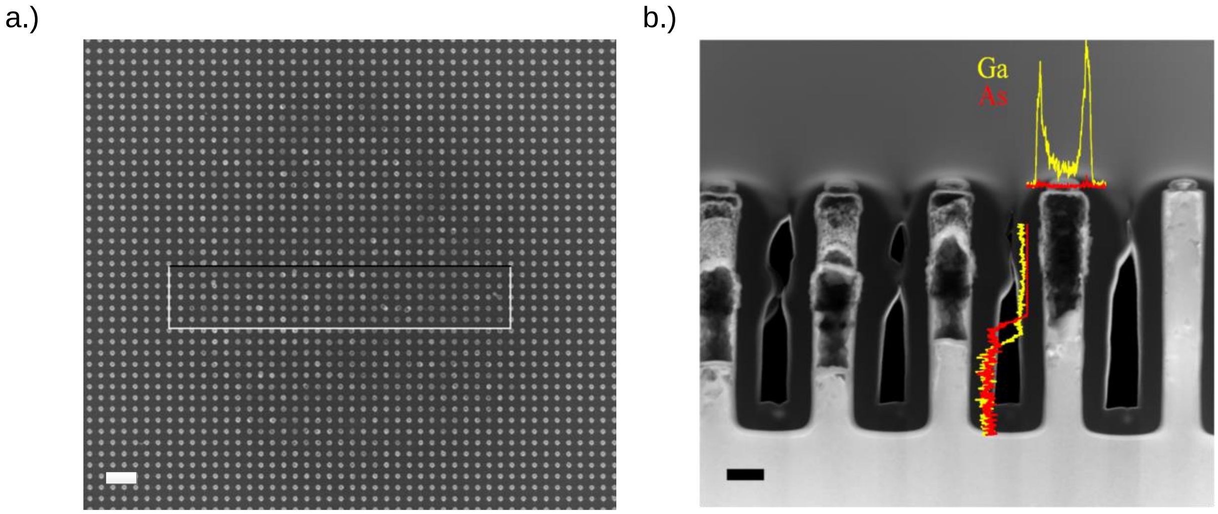

Figure 5.7: HAADF image of the FIB-prepared nanowire cross-section. The nanowires are coated in a protective carbon layer as part of the FIB preparation process. Axial and radial EDX line scans, showing the distribution of Ga and As elements, are also shown in the image for one of the altered nanowires. The decomposed structure consists of a hollow Ga-rich nanotube, and an As-rich region. The lower portion of the nanowire remains intact. The nanowire on the far right of the image was outside of the heated area. The scale bar is 125 nm.

Elemental analysis using EDX spectroscopy along the radial and axial directions for one of the altered nanowires are also shown in Figure 5.7b. The axial line scan reveals that the nanowire consists of three distinct regions; a hollow region where Ga and As species have been removed, an intermediate region As rich region, and a third region where the nanowire remains unaltered. These three areas correspond to regions where the temperatures were quite different. This result is readily understood in terms of the computer simulation presented in the next section, where it is shown that a temperature gradient is formed along the nanowire axis, with the nanowire base remaining at room temperature. The radial line scan across the hollow region of the nanowire reveals that the residual structure consists of a Ga rich nanotube. These results demonstrate that by tuning the laser power it is possible to create hollow nanotubes.

Clearly, heating due to resonant waveguiding reduces the power density which a vertical GaAs nanowire can support by three orders of magnitude relative to horizontal ones before permanent changes to the crystal structure take place. This result is particularly important for those working with III-V nanowires, where these lower laser power levels are commonly used in many spectroscopic characterization techniques.

5.3 Optimizating Photo-Thermal Conversion in GaAs Nanowires for PTE Applications.

In section 5.1, it was experimentally shown that by exciting the HE_{11} mode, a significant amount of heat can be generated for relatively low input power densities. Section 5.2 demonstrated to the reader what the effect of exceeding these limitations can be for GaAs nanowires. The temperature change in the nanowire is the result of the optical mode being absorbed, producing heat. Therefore to gain further insight into GaAs nanowire array design for PTE applications one must first understand over what volume is the mode absorbed, and secondly, what the nanowire temperature profiles look if the volume over which the mode is absorbed acts like heat source. When considering nanowires, there are three parameters which can affect the results; the diameter, length, and spacing between them. The effect of nanowire radius has already been demonstrated in Section 5.1, and also throughout Chapter 4. Specifically, the nanowire radius is chosen such that the strongest excitation of the HE_{11} mode is realized for a given input wavelength to realize maximum absorption. Furthermore, another study has already shown that the spacing between nanowires in a square lattice has little effect on the excitation of the modes. However, it is unclear what the effect of nanowire length will be on how the optical mode is absorbed, and what the resulting temperatures might be. Both of these effects are examined in this section in detail.

5.3.1 Background Physics of Heat Simulations

A brief background into the physics of heat transfer in solids is given. Heat conduction in crystals takes on the form of phonons, which were described in Chapter 2. The equation governing conductive heat transfer is [63]:

$$\rho C_p \frac{\partial T}{\partial t} + \nabla \cdot (\kappa \nabla T) = Q \tag{5.2}$$

where

- ρ is the material density (kg/m^3)
- C_p is the specific heat capacity at constant pressure (J/kg·K)
- T is the temperature (K)
- κ is the thermal conductivity (W/m·K)
- Q is the heat source (W/m^3)

In the steady state, the temperature does not change with time and we have:

$$\kappa \nabla^2 T = Q \tag{5.3}$$

which is the stationary heat equation for a volume that contains a source, Q. This is also referred to as the Poisson equation. In this study the body heat source results from the absorption of the HE_{11} mode. The distribution in the x-y plane is Gaussian with some degree of astigmatism. In other words, the mode is an elliptical Gaussian intensity profile [19]. The absorption of the mode along the nanowire length (z direction) is modelled an as exponential decay. Overall, the body heat source modelling the power in the HE$_{11}$ mode can be written as:

$$Q(x,y,z) = Q_o \frac{\alpha}{\pi\sigma_x\sigma_y} e^{-\mu} e^{-\alpha z} \tag{5.4}$$

with

$$\mu = \frac{x^2}{2\sigma_x^2} + \frac{y^2}{2\sigma_y^2} \tag{5.5}$$

and

- Q_0 is the total power input (W/m^3)
- α is the absorption coefficient (cm^{-1})
- σ_x and σ_y are the standard deviation parameters that are used to define the mode width and astigmatism in the x-y plane.

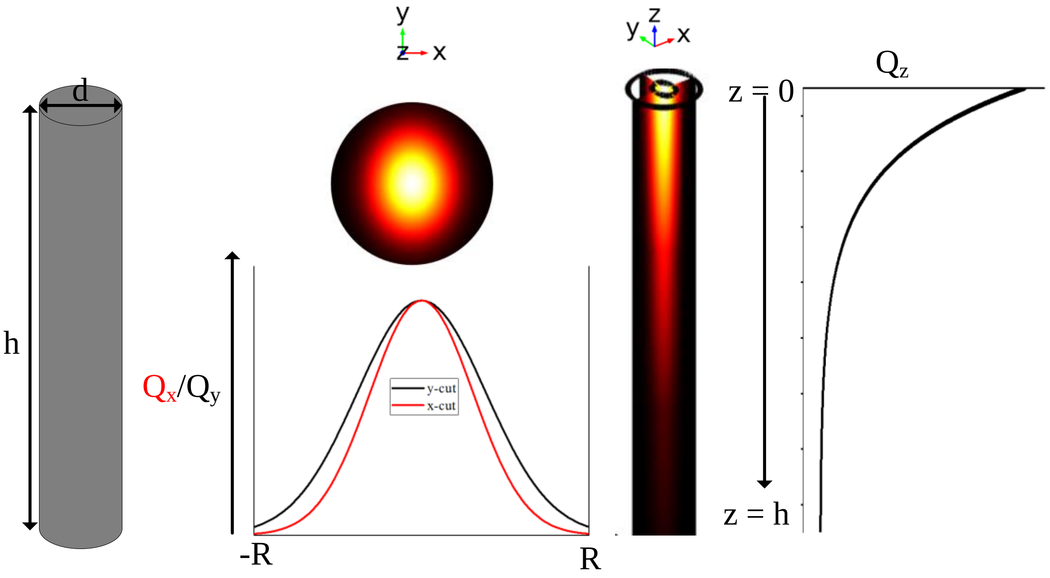

Figure 5.8: Nanowire geometry and body heat source plots of *Q(x,y,z)*, showing the Gaussian profile in x and y directions, and exponential decay in the z direction.

It is instructive to note that α is strictly defined by the input wavelength λ, which will also define the nanowire radius, *R*. The overall differential equation for *T(x,y,z)*, which is solved for using the COMSOL Heat Transfer Module is:

$$\kappa\nabla^2 T = Q_o \frac{\alpha}{\pi\sigma_x\sigma_y} e^{-\mu} e^{-\alpha z} \qquad 5.6$$

Figure 5.8 shows representative 3D and 2D views of the nanowire and the parameters associated with the simulation as well as plots for the power input *Q(x,y,z)*. It should be noted that the nanowire is placed on a 150 μm wide by 15 μm deep square slab of corresponding semiconductor material. The bottom surface of the Slab is held at T= 293 K.

5.3.2 Estimating the Thermal Conductivity of GaAs Nanowires

It is understood that nanowires possess thermal conductivity values that are reduced relative to the bulk. In order proceed with the simulations, one must first estimate the thermal conductivity of the nanowire in question. It has been suggested that smooth GaAs nanowires possess thermal conductivities ~ 10 $Wm^{-1}K^{-1}$ [23]. The etching process used to fabricate the nanowires does introduce surface roughness, the degree of which lowers the nanowire thermal conductivity. It has been theoretically shown that a 115 nm GaAs nanowire with surface roughness rms ranging from 2 Å to 4 nm has a respective thermal conductivity value that can range from 10 $Wm^{-1}K^{-1}$ to 0.1 $Wm^{-1}K^{-1}$ [23]. In comparison, Si nanowires have values which can range from 50 $Wm^{-1}K^{-1}$ to 10 $Wm^{-1}K^{-1}$ over the same range of surface roughness [23].

Another approach is to estimate the thermal conductivity by using computer simulations combined with Raman measurements. The simulations can be used to determine the nanowire temperature over a range of thermal conductivity values. One can then determine the thermal conductivity

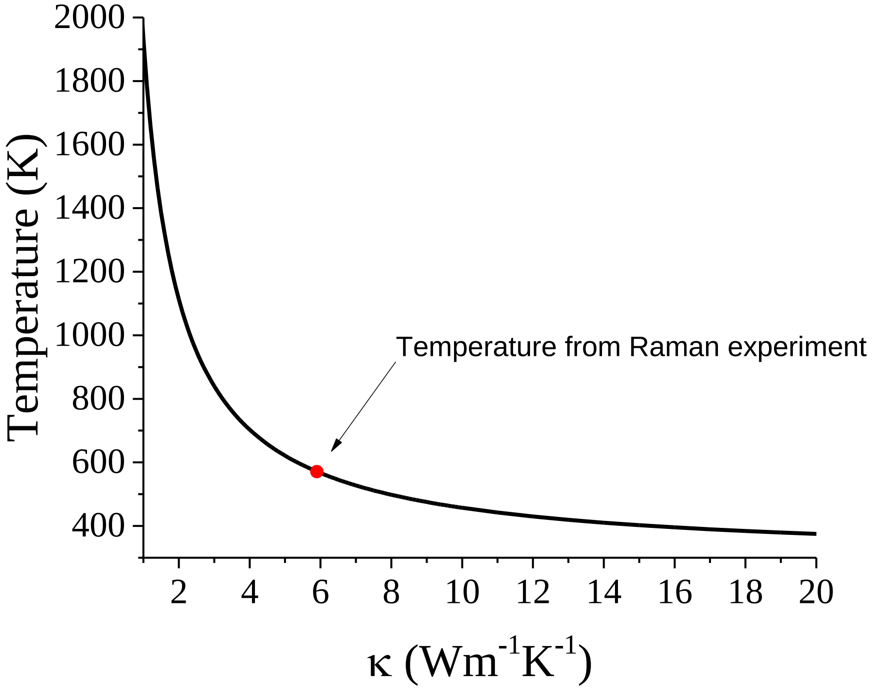

Figure 5.9: Simulated top facet temperature of a 130 nm diameter GaAs nanowire for thermal conductivity values ranging from 1-20 $Wm^{-1}K^{-1}$. A value of 6 $Wm^{-1}K^{-1}$ produces the same temperature as the Raman experiment (570 K).

value which generates a nanowire temperature that matches the temperature calculated from the Raman experiment. As before, temperatures for GaAs nanowires can be determined using equation 5.1. In general temperature is determined by measuring the intensity ratio between the Stokes, and anti-Stokes lines. However, care must be used when determining the temperature using this method since it has been shown that the actual temperature rise from a focused laser beam is twice that determined from measuring the Stokes/Anti-Stokes ratio [64]. Unfortunately, the Raman spectrometer used in this study only measures the Stokes side, and therefore the thermal conductivity of GaAs nanowires is estimated using computer simulations to serve as an example.

To estimate the nanowire thermal conductivity, an effort will be made to match to the top facet temperature of a GaAs nanowire with the experimental data appearing in Figure 5.1. The highest top facet temperature of 571 K occurs for the 1 µm tall 140 nm diameter sample, at an incident wavelength of 633 nm with an irradiance of 20 W/mm^2. Therefore, in the simulation, R = 70 nm, h = 1000 nm, α = 39000 cm^{-1}, and at the top facet Q = 20 W/mm^2. The values for σ_x and σ_y were chosen to be 20 and 25 nm, respectively. Top facet temperatures were simulated for thermal conductivity values ranging from 1-70 Wm^{-1}K^{-1} and the result is plotted in Figure 5.9 for a range of thermal conductivity values from 1-20 Wm^{-1}K^{-1}. A thermal conductivity value of κ ~ 6 Wm^{-1}K^{-1} produces a top facet temperature which matches the Raman experiment, and is within the range of thermal conductivity values seen in the literature. This value is lower than what would be expected for a perfectly smooth GaAs nanowire and is most likely due to surface roughness introduced by the etching process. By using the data from [23], it it is estimated that the surface roughness rms is ~ 1 nm. A TEM image of a GaAs nanowire sidewall is shown in Figure 5.10. From the image one can see that the sidewalls are not perfectly smooth, and shows variations which are on the order of ~ 1 nm. In this connection, one is able to estimate the thermal conductivity of a GaAs nanowire, which in turn provides an estimate of surface roughness, beginning from a single Raman measurement.

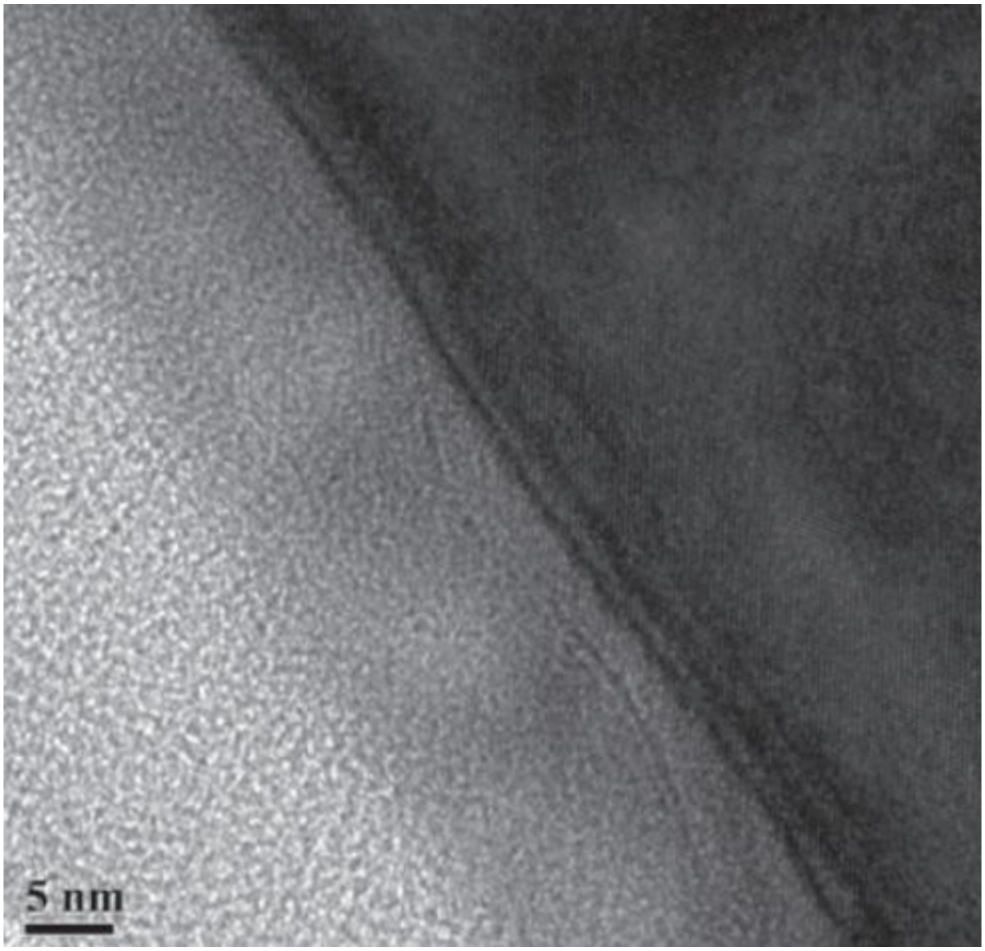

Figure 5.10: TEM image of a GaAs nanowire showing sidewalls which have undulations on the order of 1 nm.

5.3.3 Computational Temperature Profiles

The thermal conductivity of a 130 nm GaAs nanowire is taken to be 6 $Wm^{-1}K^{-1}$. Since we are interested in resonant effects, the radius is fixed, and the absorption coefficient for the resonant wavelength is used. The resonant wavelength for a 130 nm GaAs nanowire is 636 nm. Similarly, the resonant wavelength for a 130 nm diameter Si nanowire is 633 nm. The corresponding absorption coefficients are $\alpha_{GaAs} \sim 39000\ cm^{-1}$, and $\alpha_{Si} = 3890\ cm^{-1}$ [65, 66]. One can see that for an incident wavelength ~ 635 nm, there is an order of magnitude difference between the absorption coefficients of GaAs and Si. Furthermore, there is a wavelength independent order of magnitude difference in thermal conductivities. From the literature, for a surface roughness rms of 1 nm, the thermal conductivity of a 115 nm diameter Si nanowire is estimated to be ~ 40 $Wm^{-1}K^{-1}$ [23]. Along these lines, one can immediately expect to see lower temperatures in Si nanowires when compared to GaAs nanowires for an incident wavelength of ~ 635 nm. To gain an appreciation for the effects of material differences, nanowires consisting of GaAs and Si are examined concurrently at a resonant wavelength of ~ 635 nm.

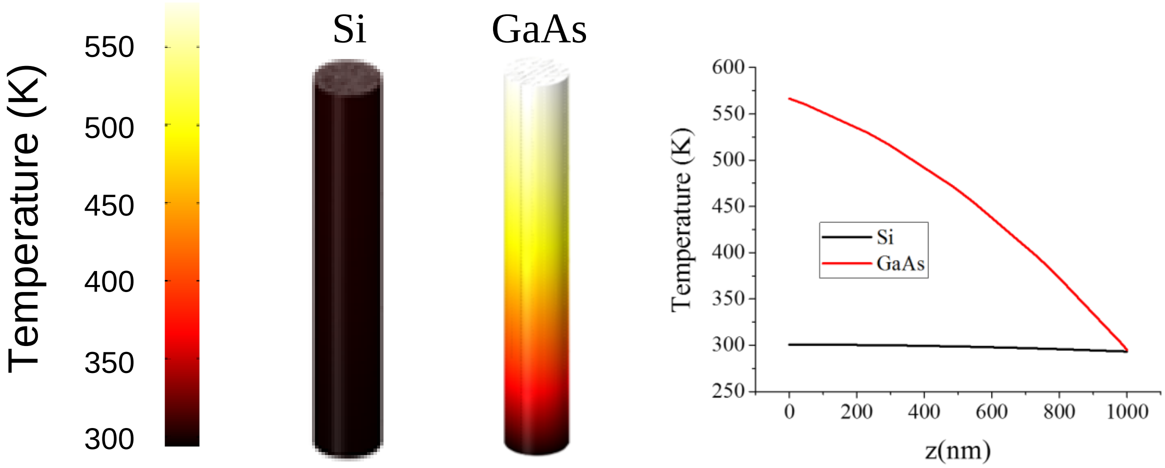

Figure 5.11: Temperature distribution of Si and GaAs nanowire for the same incident energy and resonant conditions. The order magnitude difference of the absorption coefficients and thermal conductivites of the materials are the reason for huge differences in temperature.

The temperature profiles for a nanowire made of Si and GaAs are plotted in Figure 5.11, where the effect of the different materials is readily seen. Most notably, a temperature rise of 271 K at the top facet of the GaAs nanowire exists for a heat source power density of 40 W/mm^2. Under the same conditions, only a 3 K change at the top facet of the Si nanowire is seen. This is consistent with the Si nanowire results presented in Chapter 4, where no broadening or shift of the first order phonon peak was observed. For both materials, temperature gradients exist across the length of the nanowire, but no temperature gradients are observed in the x-y plane. Along the z-direction, in both cases, the temperature varies in a parabolic manner, corresponding to linear temperature gradients. However, the reduced thermal conductivity and increased absorption coefficient of GaAs results in a significant increase in the temperature of the nanowire. It is instructive to note the only material parameters which affect the solutions to the steady state heat equation (Equation 5.3) are α and κ.

The effect of incident laser power was experimentally examined in Section 5.2, where laser power densities of 20 W/mm^2, 40 W/mm^2, and 80 W/mm^2 yielded top facer temperatures of 420 K, 571 K, and 923 K, respectively. The simulated temperatures for the top facet temperature of GaAs nanowires for power densities ranging from 4 W/mm^2 to 80 W/mm^2 are plotted in Figure 5.12 along with the experimental temperatures calculated from the Raman experiments using equation 5.1. There is reasonably good agreement with the simulated temperatures and those calculated from the Raman experiment. The deviations for the higher powers are most likely due to the decomposition of the nanowire (simulations do not account for this), resulting in a decreased thermal conductivity and therefore a higher temperature than expected. The simulations suggest that the relationship between incoming laser power and temperature is linear for both Si and GaAs nanowires. Specifically the linear relationships for the 1µm long, 130 nm GaAs and Si nanowire can be described mathematically as:

$$T = \delta Q_0 + T_{Room} \tag{5.7}$$

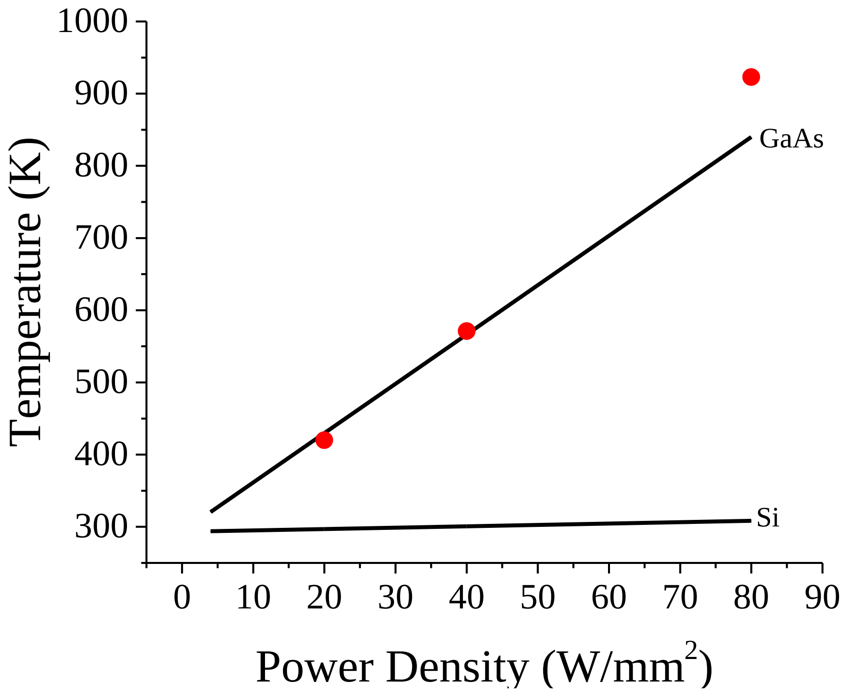

Figure 5.12: Simulated top facet temperatures of a 1 µm long GaAs and Si nanowire versus incident laser power density (solid black lines). The dots represent the experimentally determined top facet temperatures for a 1 µm long GaAs nanowire. There is a reasonably good agreement between the experiments and simulations.

Here, δ represents the temperature increase per unit heat flux ($\mathrm{K \cdot W^{-1} \cdot mm^{-1}}$). The value of δ for GaAs and Si was found to be 6.8 $\mathrm{K \cdot W^{-1} \cdot mm^{-2}}$ and 0.18 $\mathrm{K \cdot W^{-1} \cdot mm^{-2}}$ respectively. Therefore as a nanowire material, GaAs is able to generate a factor ~ 38 times the increase in temperature at the top facet over Si. In other words, to realize the same top facet temperature in Si nanowires and GaAs nanowires, one requires 38 times more laser power. Even though the nanowires have reached the same top facet temperature, the temperature distribution along the nanowire length is not necessarily the same. Figure 5.13 shows the temperature distribution along the z-axis for GaAs nanowires at an irradiance of 40 W/mm2, and for Si nanowires at an irradiance of 1.52 kW/mm2 (38 times more). As expected the temperature distribution across the nanowire is slightly different. The salient feature is that the Si nanowire shows higher temperatures over a longer length, when the nanowires are on a substrate.

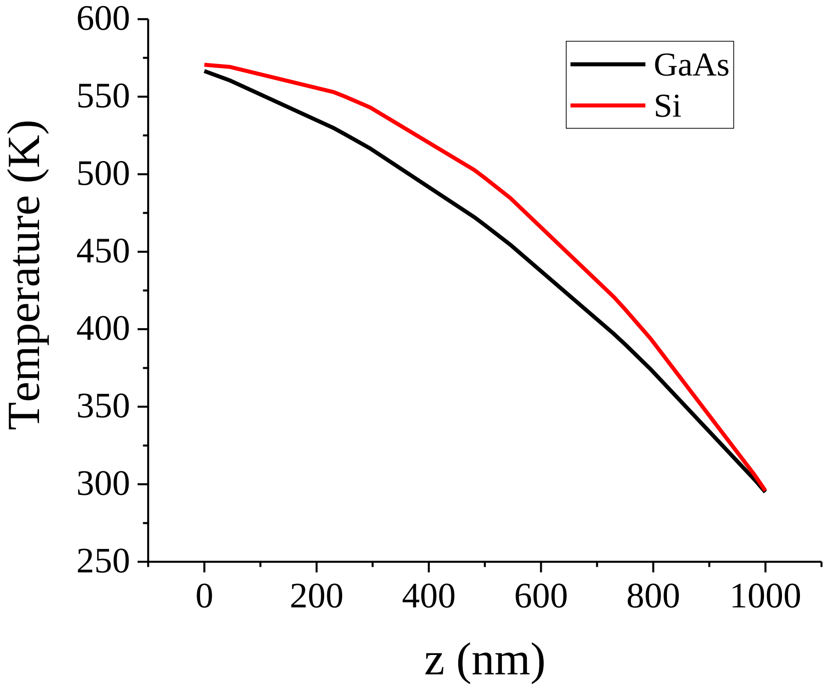

Figure 5.13: Temperature distribution of a GaAs and Si nanowire for two different input powers of 40 W/mm^2 and 1.52 kW/mm^2, respectively. Even though the nanowires have the same temperature difference across their lengths, different temperature profiles are still observed.

At this point it is unclear if α or κ has the larger effect on the temperature profiles. So far, the combined effect has been considered since two different materials were being compared. Strictly, the absorption coefficient of interest depends on the incoming wavelength of light, and the incoming wavelength dictates the nanowire diameter. Therefore, it is not actually possible to understand the effect of varying α alone in an actual material. Fortunately, significant insights can be gained from considering general solutions to Equation 5.6. Let us consider a 1 µm long, 130 nm diameter nanowire which is subject to a body heat source resulting from the absorption of an excited HE_{11} mode. The effect of κ for a specific case has already been seen in Section 5.3.2. The general effect of α and κ can be more easily seen by creating a contour plot as shown in Figure 5.14. From this plot alone it is very clear that nanowires which have thermal conductivities that are greater than 10 $Wm^{-1}K^{-1}$ are rather poor at generating any significant temperature increase for an irradiance of 40 $Wm^{-1}K^{-1}$. More interestingly, there is an optimum value for α which generates maximum temperatures, regardless of the value κ takes on. For the 1 µm long GaAs nanowire this value is ~ 76500 cm^{-1}.

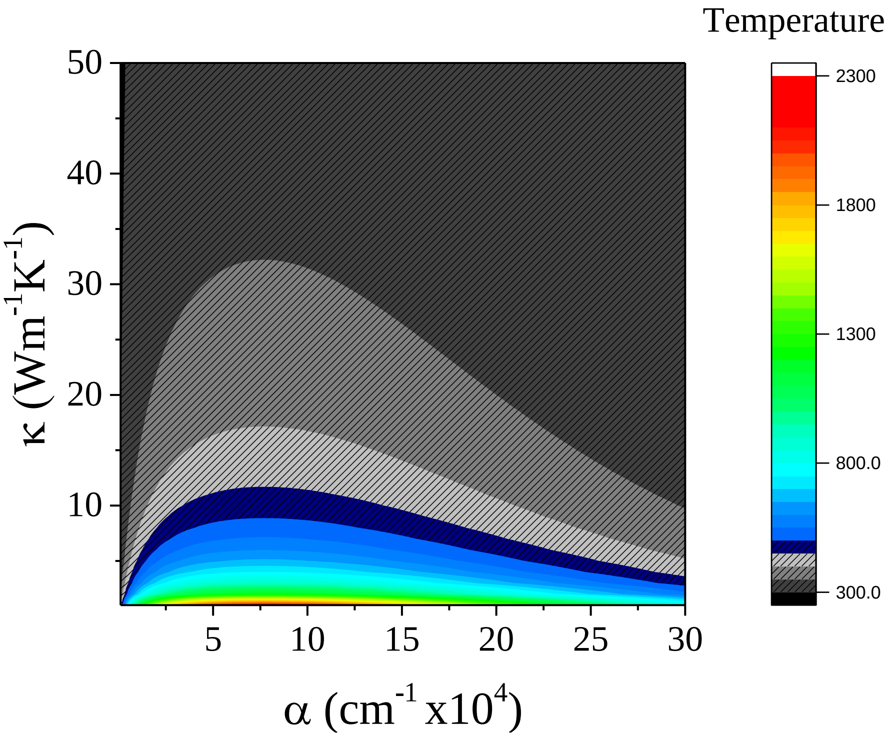

Figure 5.14: Contour plot for the top facet temperature of a 1 μm long, 130 nm diameter nanowire for different of α and κ, and an input power density of 40 W/mm^2. Regardless of the value of α, a reduction in κ leads to an increased top facet temperature. On the other hand, the same optimal value for α leads to the maximum top facet temperature for every value of κ.

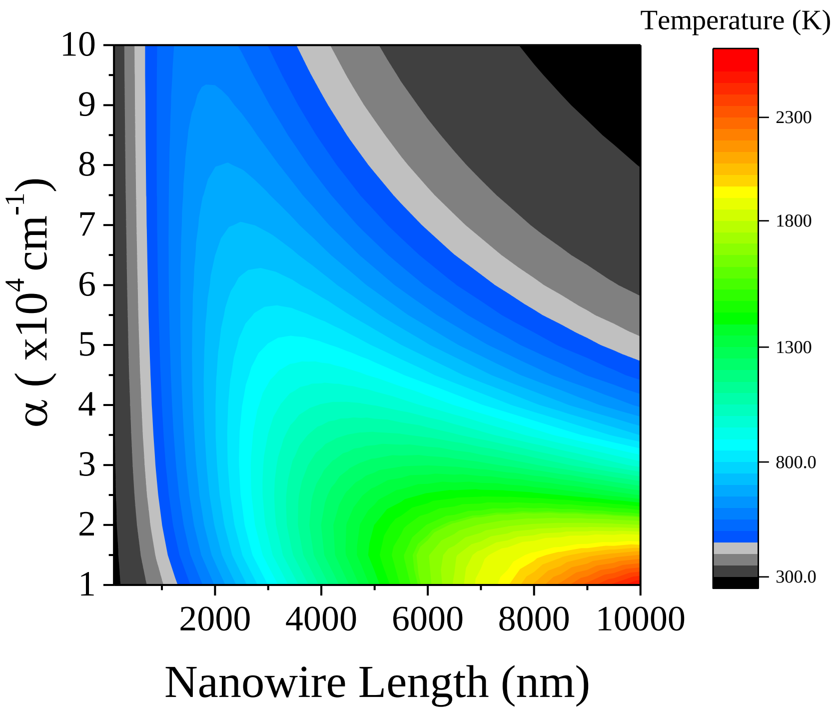

Figure 5.15: Contour plot for the top facet temperature of a 1 μm long, 130 nm diameter nanowire for different of *α* and nanowire length, *L*, and an input power density of 40 W/mm^2. For a given nanowire length, there is an optimal value for α that produces the maximum nanowire temperature.

Since the body heat source acts over a fixed volume defined by the absorption coefficient, it is expected that nanowire length will play a significant factor in determining the overall nanowire temperature. The general effect of nanowire length was investigated for *α* values ranging from 10000 cm^{-1} to 100000 cm^{-1}, the results of which can be seen in the contour plot in Figure 5.15. The simulations suggest that as the length of nanowire is increased, a lower absorption coefficient is required to realize higher and higher temperatures. On the other hand, as the length of the nanowire is decreased, higher values of *α* are required.

Overall, one can now apply these ideas in order to optimize a design for a given photothermal application. In this connection, the incident wavelength and the material involved in the application are the two factors which will ultimately guide the design optimization process. The incoming wavelength, and choice of material will dictate the nanowire diameter. Referring back to Figure 5.14, materials which have thermal conductivities that are larger than ~ 10 $Wm^{-1}K^{-1}$, are very poor at generating any significant temperature increases for an irradiance of 40 W/mm^2. Of course one could use an arbitrarily high input power to realize temperature increases in materials which have high thermal conductivities, however this would not be very practical. Usually when photothermal effects are used, the source is a either a low powered laser (~ 1 W/mm^2) or the Sun (~1 W/mm^2) under concentrated solar conditions), and therefore proper optimization will always be required. The optimization for any material can be done by using Figures 5.14 and 5.15. First, the material and diameter of the nanowire is chosen depending on the incident wavelength of light to be used. Since the absorption coefficient depends on the wavelength, one can then use Figure 5.15 and equation 5.7 to estimate the appropriate length of nanowire required to achieve the desired temperature.

CHAPTER 6

Laser Crystallization of Amorphous Silicon Nanowires

Introduction

Amorphous silicon has established itself as an important semiconductor material. The ability to deposit a-Si onto various substrates, such as glass, metals, and plastics, makes it an attractive material of choice over its crystalline counterpart for applications which involve thin films. In this connection, a-Si is widely used in the production of thin film solar cells. More recently, vertically oriented semiconductor nanowire arrays are gaining attention for their strong optical absorption characteristics. Therefore, it is only natural to consider vertical a-Si nanowire arrays as an effective platform for next generation solar cells, however very little work has been done along these lines. There is one study however which has very nicely demonstrated that a-Si nanocone arrays can be used to achieve maximum optical absorption up to the bandgap of a-Si. The nanocone geometry effectively creates slowly varying refractive index profile between the surrounding air and the nanowire array, which provides impedance matching for a large range of wavelengths.

Recalling from Chapter 2, c-Si is made up of a tetrahedral network of covalent bonds. This is a result of minimizing free energy, and along these lines, the bonds in the a-Si network will always tend towards making tetrahedral bond angles [67]. Since the free energy of c-Si is lower than a-Si, and given an extremely long period of time, a sample of a-Si would eventually crystallize and become c-Si even at room temperature, and raising the temperature speeds up the process [67]. In practice, this in unlikely, and usually a transformation to a polycrystalline state is observed when heating is induced. The optical guiding characteristics of vertically oriented nanowires can generate a significant amount of heat. In particular it was shown in Chapter 5 that when the HE_{11} mode is excited in vertical GaAs nanowires, a laser power density of ~ 10-100 W/mm^2 would create similar local temperatures to when horizontal nanowires were irradiated with power densities that are three orders of magnitude higher. A similar situation will be encountered with vertically oriented a-Si nanowires. This is similar to the concept encountered in the previous chapter for GaAs, but in this case the transformation is from an amorphous state to a crystalline state. Regardless, any changes will result in variations to the complex dielectric constant of the material, which in turn will affect the optical absorption characteristics of the arrays. Therefore, as technologies which take advantage of the strong absorption characteristics of vertical a-Si nanowire arrays emerge, it becomes equally important to understand under what optical conditions a-Si nanowires arrays begin to crystallize.

In Chapter 4, it was shown that Raman spectroscopy is a powerful technique that can be used to characterize both crystalline silicon (c-Si) nanowires as well as amorphous silicon (a-Si) nanowires. Laser heating of a-Si has been known to result in crystallization of the material, and studies have shown that a Raman setup can be used to crystallize and characterize a-Si films, and nanowires. The process of heating a-Si can actually result in different degrees of crystallinity. For example, one could end up with an amorphous material which has tiny nano/micro crystalline domains scattered throughout the disordered matrix. This is commonly referred to as micro-crystalline silicon (µc-Si). As further crystallization is induced, the resulting material tends towards a polycrystalline state. A polycrystalline material consists entirely of randomly oriented crystalline domains, which can be thought as a randomly oriented unit cells of c-Si. Generally it is very difficult to go from an amorphous state to a crystal which possesses long range order.

In this chapter, focus is given to understanding the Raman spectral features of a-Si nanowires on glass that have been irradiated using a 533 laser. The a-Si nanowires presented in Chapter 4, with diameters ranging from 75 nm to 125 nm were investigated using Raman spectroscopy. It is clearly shown that the excitation of the HE_{11} mode leads to a limited formation of c-Si species ~~more rapidly~~ when compared to off resonance conditions. Furthermore it is shown that long range crystalline order is never achieved, regardless of the irradiance conditions used. Lastly it is demonstrated that the optical properties of the nanowire arrays are significantly altered after photo-crystallization takes place. To this end, it is shown that one can use a laser to print a pattern into the array.

6.1 Raman Analysis of Materials Consisting of a-Si and c-Si.

In this section, the analysis of Raman lineshapes that arise from heterogeneous samples of silicon which consist of amorphous and crystalline regions is discussed. The volume fractions of c-Si, as well as the size of the c-Si crystalline domains, will have an influence on the optical absorption characteristics of the material. Along these lines, the techniques used to extract the crystalline volume fraction as well the particle sizes from Raman spectra are briefly discussed.

6.1.1 Estimating Crystalline Volume Fraction

Referring back to Chapter 4, c-Si produces a Lorentzian peak centred at 520 cm^{-1} with a FWHM of about 3-4 cm^{-1}, whereas a-Si produces very broad features (60 cm^{-1} -100 cm^{-1} wide) in the 300-600 cm^{-1} spectral region. Therefore one can expect that a μc-Si sample would generate a Raman lineshape which is a superposition of the spectral lineshapes corresponding to c-Si and a-Si.

However it is not very straightforward to determine the relative amounts of each phase unless some assumptions are made. When considering two-phase mixtures, one can determine the relative amounts of each if one has knowledge of the ratios of the scattering efficiencies. In the most simplest case, the crystalline volume ratio δ_c of a μc-Si sample is given by [49,68-71],

$$\delta_c = \frac{I_c}{I_c + \rho I_\alpha} \qquad 6.1$$

Here, I_c and I_α~~a~~ are the intensities of the crystalline and amorphous spectral features in the Raman spectrum, and ρ is the ratio between Raman efficiencies for a-Si and c-Si. It turns out that ρ depends on the size of the crystallite, and assuming a spherical confinement of phonons in c-Si crystallites with diameter D, ρ assumes an exponential dependence according to [71]:

$$\rho(D) \cong 0.1 + e^{-D/250} \qquad 6.2$$

As the diameter of the crystallite decreases, ρ tends towards unity, and it is generally accepted that there is no difference between the efficiencies for amorphous and crystalline phases when the crystallite size becomes less than ~ 3 nm [71]. Therefore, to accurately estimate the crystalline volume fraction requires as accurate estimate of ρ, which may not always be possible.

6.1.2 Estimating Crystallite Size

The most widely cited model in the literature used to estimate sizes of Si crystals is the correlation length model [71]. Using this model, the dependence of the FWHM and shift of the c-Si one phonon peak on the size of the Si crystallite can be determined. More recently, another model has been developed which is based on bond polarizability. However, the bond polarizability model only correlates the size of the crystallite to the shift of the one phonon peak. It should be pointed out ~~however~~ that using the shift of the c-Si peak in Raman spectra is less prone to error. Determining the FWHM of the c-Si is less straightforward and requires peak fitting, and depending on the process used to fit the spectra, different FWHM values may occur. This is especially true when considering spectra from samples of μc-Si nanowires [49]. Therefore for the purposes of this work, the shift of c-Si peak will be used to estimate crystallite size. According to both the bond polarization, and length correlation models, the dependence of the Raman shift versus Si crystallite diameter is given by [71]:

$$\Delta\omega(D) \sim \left(\frac{a}{D}\right)^{\gamma} \tag{6.3}$$

Here *a* is the distance between neighbouring silicon atoms, which is usually taken to be 0.543 nm. For the bond polarizability model, γ = 1.44, and for the length correlation model γ = 1.39 [71].

6.2 Raman Spectra of Laser Irradiated a-Si nanowires.

The a-Si nanowire samples that were examined in Chapter 4 were irradiated using a 533 nm laser to induce local heating and crystallization of the amorphous material. Table 6.1 lists the measurement parameters that were used to acquire the room temperature spectra after irradiation of the samples. In order to induce crystallization, the samples were irradiated at 480 W/mm^{-2}. Figure 6.1 shows the Raman spectra from the laser irradiated nanowires for diameters ranging from 75 to 125 nm.

Measurement Parameter	**Value**
Laser Wavelength/Power	533 nm / 0.6 W
Laser Power Density	6 W/mm^2
Exposure Time	5 s
Accumulations	15

Table 6.1: Measurement parameters used to acquire Raman spectra from a-Si nanowires that were crystallized.

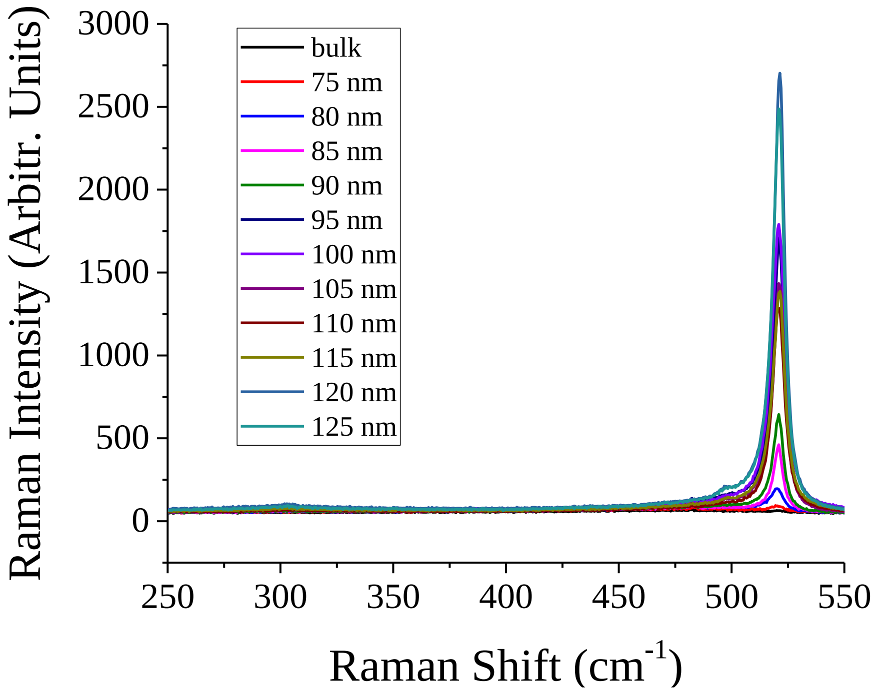

Figure 6.1: Raman scattering from a-Si nanowire arrays after exposure to an irradiance of 480 W/mm2 to promote crystallization. Clear spectral differences are seen relative to Figure 4.10.

The spectra are now dominated by a sharp feature centered at ~520 cm^{-1} which is characteristic of c-Si.

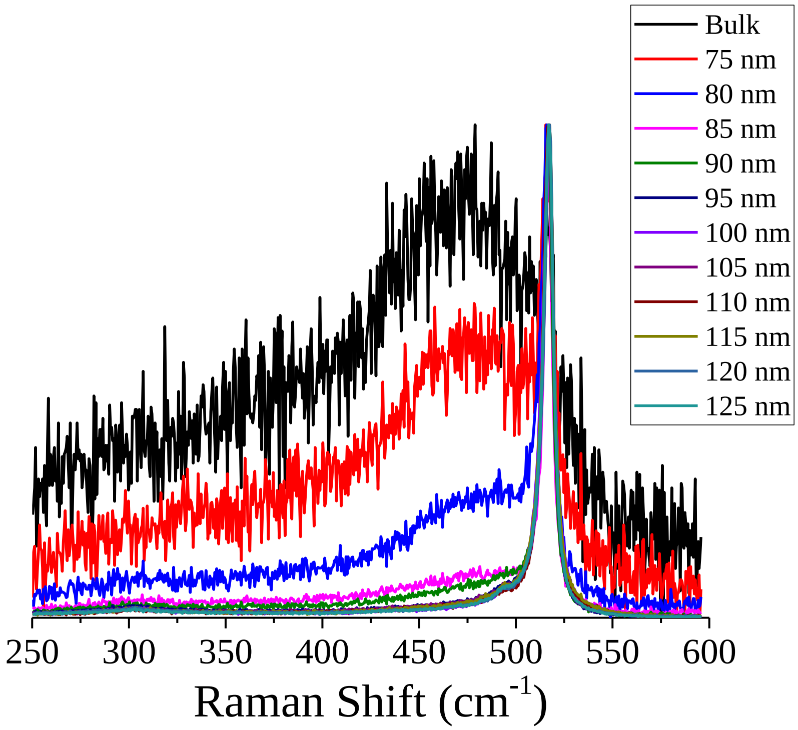

Figure 6.2: Normalized Raman spectra from all of the nanowire samples. Different degrees of crystallinity are observed. As the diameter of the nanowire increases, the amorphous signatures begin to diminish.

The salient feature of Figure 6.1 is that the amorphous signatures have been significantly reduced, and a sharp feature characteristic of c-Si has emerged. In order to see the resulting changes more clearly, normalized spectra [SS1]from the nanowire samples are shown in Figure 6.2. Interestingly, for the smallest nanowire diameter the least amount of crystallization has occurred, and as the diameter increases it appears there is a concomitant decrease in TO scattering from a-Si. It is not apparent in Figure 6.2, but there are other interesting spectral features which vary with diameter. Firstly, as

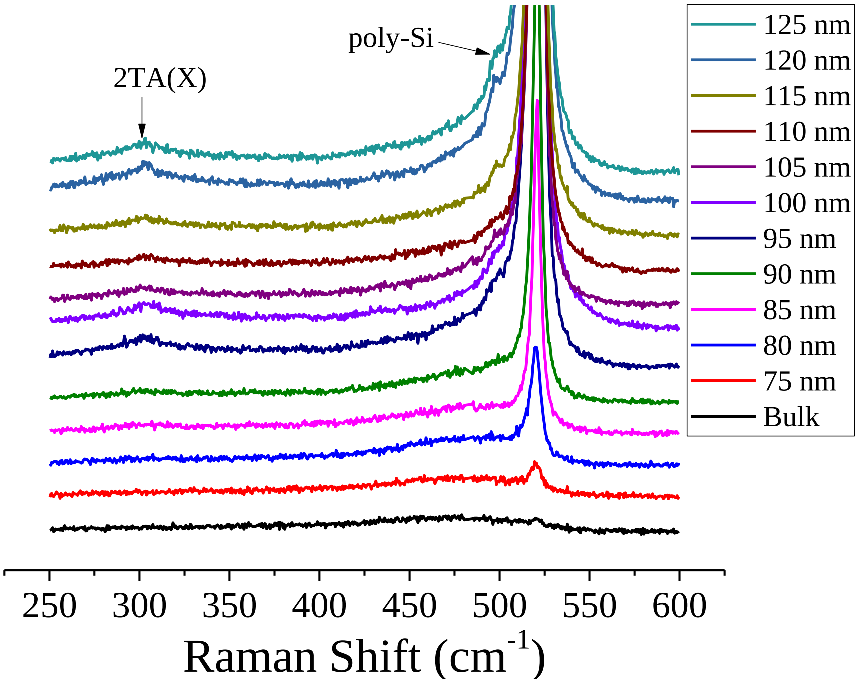

Figure 6.3: Stack plot of all Raman spectra taken showing the emergence of two distinct spectral features at ~ 300 cm^{-1} and ~ 500 cm^{-1} - 510 cm^{-1}.

shown in Figure 6.3, in the ~ 300 cm^{-1} region, a spectral feature which can be assigned to the 2TA(X) mode in c-Si is observed [42-44]. The intensity of the peak varies for different diameters and can be used as indicator that there are crystals domains which have long range order. A second feature appearing near ~ 500 cm^{-1} also begins to form as the diameter is increased beyond ~ 90 nm. The result is that the 520 cm^{-1} line corresponding to c-Si is asymmetrically broadened. This suggests that there are areas in the sample where long range order is not present, however crystallization has taken place, and the feature appearing at 500 cm^{-1} is assigned to scattering from poly-Si. It has been clearly shown that prior to irradiation the a-Si nanowire Raman spectra consisted of three peaks (as seen in Chapter 4). After irradiation, it is generally expected that the nanowires will consist of regions of amorphous material, and regions of material with different sizes of crystallites. Since the spectral feature at 500 cm^{-1} starts to grow beyond this diameter, it is difficult to determine how much amorphous component centered ~ 480 cm^{-1} remains by simply considering the intensity in these regions.

To gain more quantitative information, each spectrum was deconvolved using up to three Gaussian peaks to represent TO, LO, LA scattering from a-Si (see Chapter 4), and two Lorentzian peaks to represent the one phonon spectrum of c-Si, and the other for scattering from smaller crystallites of Si. Using five peaks and arbitrarily fitting the data would not yield meaningful results since one would essentially be overfitting the data. Constraints must be applied on the fitting process if the resulting spectral deconvolution is to be used to gain physical insights into the material. For peaks representing Raman signatures from a-Si, the center positions of the TO, LO, and LA modes were fixed to the values of 480 cm^{-1}, 410 cm^{-1}, and 305 cm^{-1}. The peak representing c-Si was fixed to a center frequency of 520 cm^{-1}, and the width was allowed to vary. The peak representing poly-Si was fixed between 500 cm^{-1} and 510 cm^{-1}. Furthermore, only the 75 nm and 80 nm diameter samples show any significant amorphous signatures, and no evidence of 2TA(X) scattering, and use all five peaks in the fitting process. For, the other samples, the fitting was constrained to the 400 cm^{-1} to 600 cm^{-1} region since there was no evidence of any LO or LA scattering from a-Si. Representative fits for the 75 nm , 85 nm, 100 nm, and 125 nm diameter samples are shown in Figure 6.4. The spectra are well fit using the fitting procedure described, and now one can more accurately determine the crystalline volume fraction, and crystallite sizes that are in the sample.

The total crystalline volume fraction was calculated using equation 6.1. In this case the spectral contributions at 500-510 cm^{-1} and 520 cm^{-1} contribute to overall crystalline volume fraction.

Therefore, given the fitting model is correct, one can extract how much of the crystalline volume fraction consists of c-Si which possesses long range order. Table 6.2 shows the calculated crystalline volume fraction for all diameters. It is instructive to note that for diameters larger than 95 nm, a significant portion (> 85 %) of the spectral area is from crystallized a-Si.

Diameter (nm)	**Total**	**% c-Si**	**% poly-Si**
75	20	20	0
80	47	42	5
85	67	65	1.6
90	68	66	2
95	84	79	4.8
100	96	90	5.7
105	89	82	7
110	91	86	9
115	95	86	9.3
120	96	86	11
125	93	84	8.6

Table 6.2: Calculated crystalline volume fractions of c-Si and poly-Si after irradiation of the nanowire samples. The total is the sume of c-Si and poly-Si fractions. The fractions were calculated using equation 6.1.

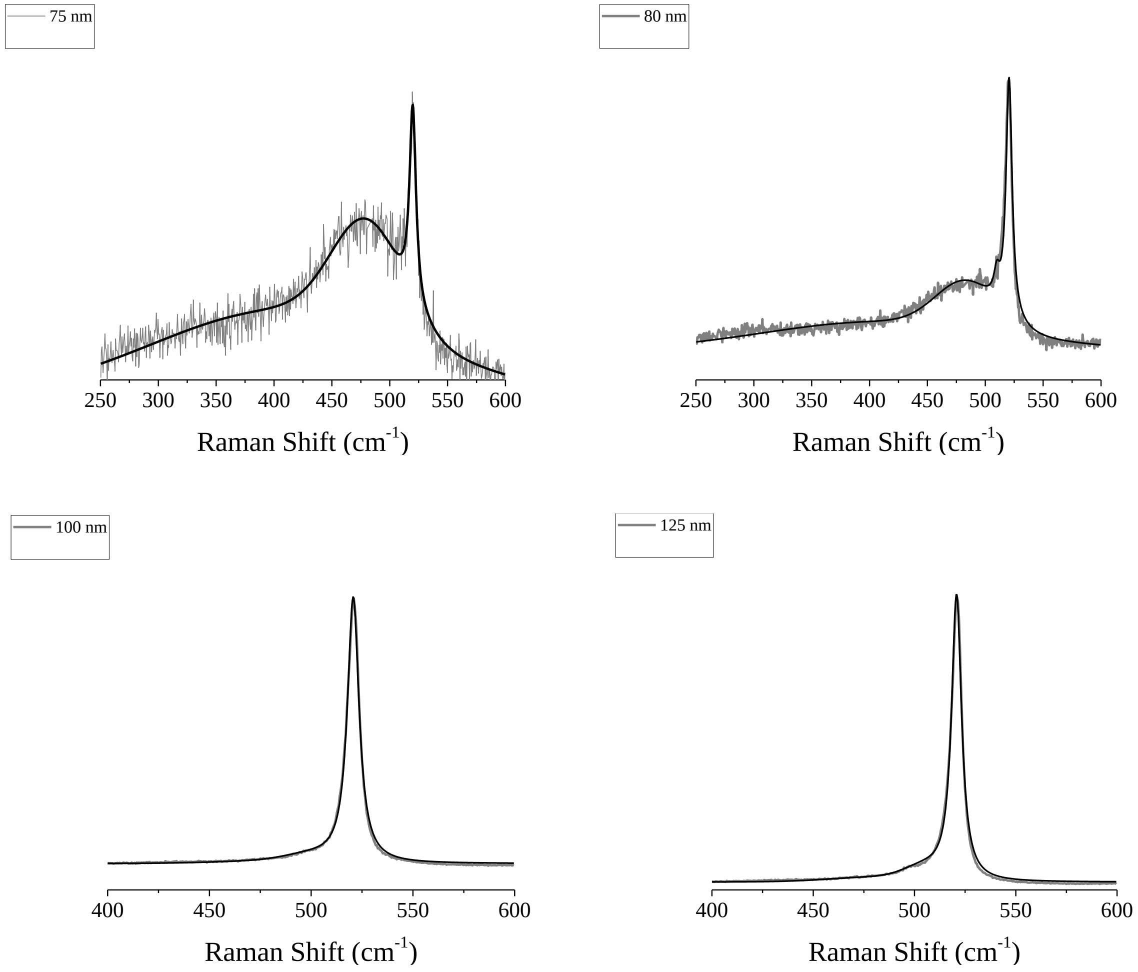

Figure 6.4: Representative fits for 75 nm, 80 nm, 100 nm, and 125 nm diameter nanowires.

The quality of the silicon crystals formed after irradiation can most easily be determined by examining the FWHM of the resonance at 520 cm^{-1}. For every sample, the center position of the peak was 520 ± 0.3 cm^{-1}. The width of the resonance at 520 cm^{-1} versus nanowire diameter is plotted in Figure 6.5. High quality silicon crystals exhibit a linewidth of 3-4 cm^{-1} [42], and none of the nanowires after irradiation have a linewidth within this range. There is however a minimum linewidth which occurs for the 85 nm diameter sample. This suggests that the silicon crystals

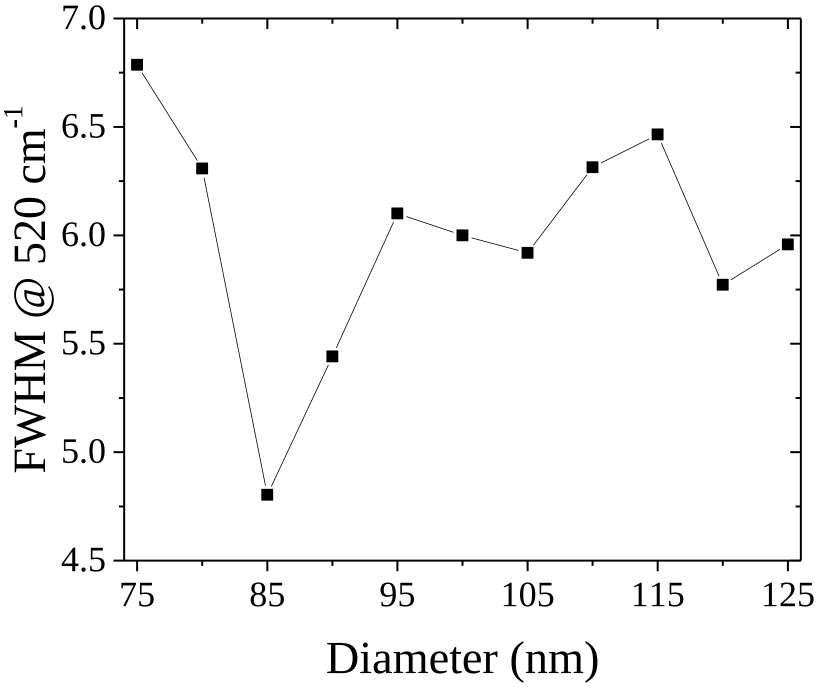

Figure 6.5: FWHM of the 520 cm^{-1} peak of c-Si. The 85 nm diameter sample exhibits the smallest linewidth, and therefore the highest quality silicon crystals.

formed in this sample have very long range order. Furthermore, the 85 nm diameter sample has the lowest amount (1.6 %) poly-Si that has formed. Referring back to Chapter 4, the resonant diameter for a-Si nanowires for an incident wavelength of 533 nm was 85 nm. As was shown with GaAs nanowires in the previous chapter, heating due to resonant excitation resulted in the nanowires essentially decomposing from the inside out. For the case of a-Si nanowires presented here, it appears that resonant excitation of the HE_{11} mode leads to the formation of higher quality silicon species relative to other diameters. This being said, this sample still only has a crystalline volume fraction of 67 %, whereas the larger diameter samples consistently have crystalline volume fractions as high as 96%.

To explain why the 85 nm diameter did not fully crystallize one must consider that for a fixed wavelength, the diameter at which a certain material will generate resonant excitation of the HE_{11} mode depends on the materials refractive index [47]. The refractive indices of a-Si and c-Si at 533 nm are 4.8 and 4.1 respectively. As the nanowires being to crystallize, the refractive index is going to change, and therefore the resonant diameter will shift towards 100 nm. For c-Si, the resonant diameter for an incoming wavelength of 533 nm is 100 nm . Figure 6.6 plots the RIV for the c-Si phonon peak at 520 cm^{-1}, as well as the RIV for the TO phonon frequency of a-Si at 480 cm^{-1} for all diameters. A clear shift in the resonant diameter from 85 nm to 100 nm is observed, which is consistent with the Raman spectra suggesting that the nanowires now consist mostly of c-Si. Equally as important, it was shown in Chapter 5 that nanowire diameters which are smaller than the resonant diameter generate very little to no temperature increases, however larger diameters still generate some local heating due to weak excitation of the HE_{11} mode, as well as higher order modes. Therefore, as the 85 nm diameter nanowires crystallized, no further heat was being generated since the diameter was now below resonance, thus limiting the formation of any more c-Si. In fact it has been shown that crystallization occurs on the nanosecond timescale [67], which implies that the optical properties of the nanowires were instantly altered. In this connection, for the 85 nm diameter sample, the time that the nanowire was exposed to elevated temperatures was limited by this process, and can explain why the 85 nm diameter nanowires still have a significant amorphous component.

There is a sudden jump in the crystalline volume fraction as the nanowire diameter increases beyond 95 nm. From the data shown in Figure 6.2, it is clear that all of the larger diameter nanowires generated enough heat to induce to crystallization. The increased crystal volume fraction for the larger diameters can be understood by considering the change in the resonant

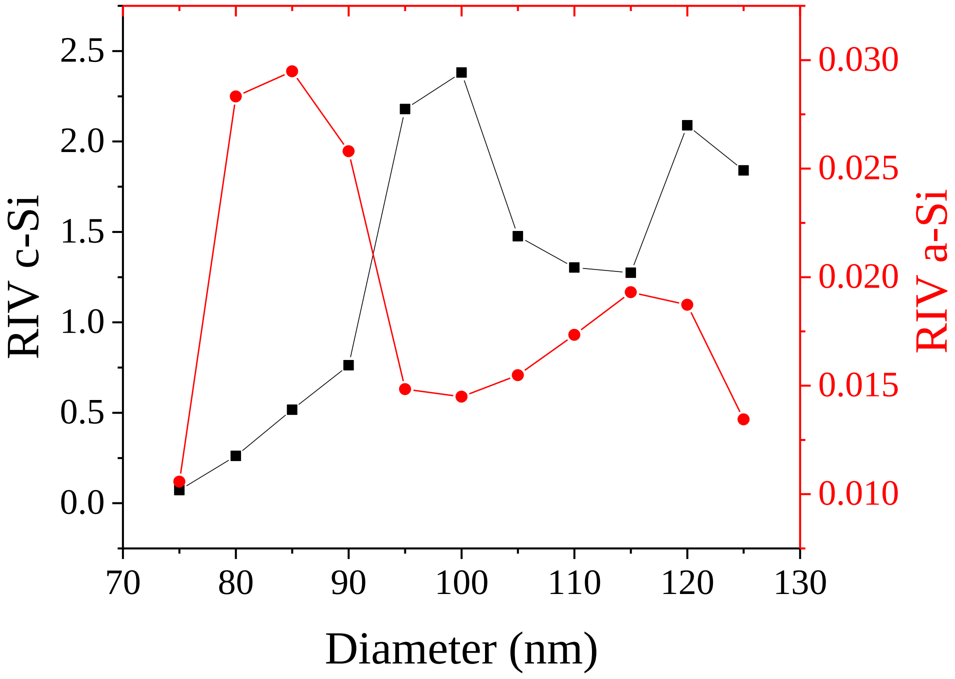

Figure 6.6: RIV for the c-Si phonon peak at 520 cm^{-1}, as well as the RIV for the TO phonon frequency of a-Si at 480 cm^{-1} for all diameters.

diameter that occurs as crystallization is taking place. For example, as the 100 nm diameter nanowire begins to crystallize, it will resonate more and more with the incoming light field. Therefore, unlike the 85 nm diameter sample which experiences a significant drop in the amount of heat being generated, the 100 nm diameter sample is able to generate more and more heat, and thus is able continue crystallizing. This concept is also similar for the larger diameter nanowires. Even though less increase in resonance is expected, the larger diameter nanowires are able to maintain a high enough temperature to allow crystallization to proceed.

In summary, the degree of crystallization in vertical a-Si nanowires depends on the diameter. Smaller a-Si nanowires that resonate with an incoming field, which begin to crystallize, experience significant decreases in local temperature within a short timeframe since their diameters now lie below the resonant value of 100 nm. As crystallization is induced in the larger dimeter samples, the temperature can be maintained due to increased resonance with the incoming light field as c-Si is formed. More interestingly, the 85 nm diameter sample exhibited the narrowest linewidth for the 520 cm^{-1} peak of c-Si, suggesting that the instantaneous resonant heating and equally rapid cooling produce very high quality c-Si domains. Given the hallow morphology realized in GaAs nanowires from heating due to excitation of the HE_{11} mode, it is proposed that the resulting structure of the 85 nm diameter sample is a core-shell c-Si-a-Si nanowire. For the larger diameter nanowires, where the initial heat generated was not purely due to a guided mode and was not limited to a nano second timescale, it is expected that the nanowire will essentially consist entirely of Si with some residual a-Si near the bottom surfaces. Determining the validity of this proposal would require TEM analysis and remains a topic of future interest.

In this section it was shown that laser induced solid-solid phase changes results in a variation to the complex dielectric constant of the material, which in turn will affects the optical absorption characteristics of the arrays. Therefore, as technologies which take advantage of the strong absorption characteristics of vertical a-Si nanowire arrays emerge, it is equally important to understand under what optical conditions vertical a-Si nanowires arrays begin to crystallize.

CHAPTER 7

Colourimetric Applications Involving Vertical Nanowires

Introduction

Prior to performing each Raman measurement, alignment of the sample in the field of view was required. It was quickly realized that different nanowire arrays produced different structural colours depending on the geometry of the array. Colour generation was first demonstrated in a single horizontal SiNW and was attributed to strong Mie scattering of light [72], and the generated colours were also found to be dependent on the diameter of a given nanowire. Vertical silicon nanowires, arranged in square lattices, also produce structural colours resulting from guided modes within the SiNWs coupling selectively with various substrate modes [7]. Specifically, the colour generation was attributed to the SiNWs acting as individual waveguides, and once again the observed colours depended on the diameter of the nanowires.

In this chapter, two different applications of structural color generation are discussed. Firstly, it is shown that diffraction can be used to determine the spacing of a nanowire, and can also be used to tune the structural colour observed. Along these lines, a linear refractive index sensor based on diffraction from Si nanowires is presented. The second application involves using photo-thermal modification to demonstrate high resolution nanowire laser printing. It was shown in Chapters 5 and 6 that a laser can be used to alter the structural properties of vertical GaAs and a-Si nanowire arrays. It turns out that the structural changes result in very obvious changes to the colours which are generated, and are limited to only the focal spot of the laser.

7.1 Meaurement of Nanowire Pitch and Refractive Index Sensing using Diffraction

In our previous work, colour generation was extended by strongly coupling neighboring SiNWs in the near field, and a refractive index sensor based on measuring colour changes was realized [8]. The sensor measures changes in the red, green, and blue (RGB) colour content due to changes in the local refractive index. In the aforementioned studies, the waveguiding properties of SiNWs were used for generating the structural colours, and it was not straightforward to link the colour seen to any geometrical parameter of the array in a general sense.

In this section, it is shown that Si nanowires arranged in periodic lattices can also act as a two-dimensional diffractive grating and various colours spanning the entire visible spectrum can be generated using diffraction. Colours are generated by diffraction, and are nearly independent of the SiNW diameter, but highly dependent on the spacing between the nanowires and are adequately described by simple Bragg theory. In keeping with this, the spacing of a nanowire array can be determined when generated colours are measured using a spectrometer. The colour observed for a given lattice spacing can also be tuned by simply changing the angle of the incident light. The generated colour is also dependent on the refractive index of the medium surrounding the nanowires. The ease of colour tuning through simple diffraction theory is applied and demonstrated for use as a linear refractive index sensor, which measures the colour change in a RGB trichromatic decomposition resulting from a change in refractive index. A maximum refractive index resolution of ~$5x10^{-4}$ was achieved with a linear response to changes in refractive index. The sensor performs without the need for a spectrometer to detect the changes. To achieve this goal, the sensor is designed to only allow one of the components of the colour (G) to change as the refractive index of the surrounding medium changed, and results in a highly linear and predictive response.

7.1.1 Diffraction from Periodic Structures

A brief introduction to simple Bragg diffraction theory is given. When light of a specific wavelength, λ, hits a periodic structure with spacing *d*, diffraction will occur if the light is incident along one of the lattice directions. The light is sent into various discrete directions, and when light is reflected from these periodic structures, with path length differences which are an integer multiples of the incident wavelength, λ, constructive interference occurs. Figure 7.1. serves to illustrate geometrically the diffraction effect. The incident and diffracted angles, θ_i and θ_r, are measured from the grating normal. The path difference between light from adjacent grooves spaced *d* nm apart is given by

$$\mathrm{d}(n_1 \sin\theta_i \pm n_1 \sin\theta_r) \qquad 7.1$$

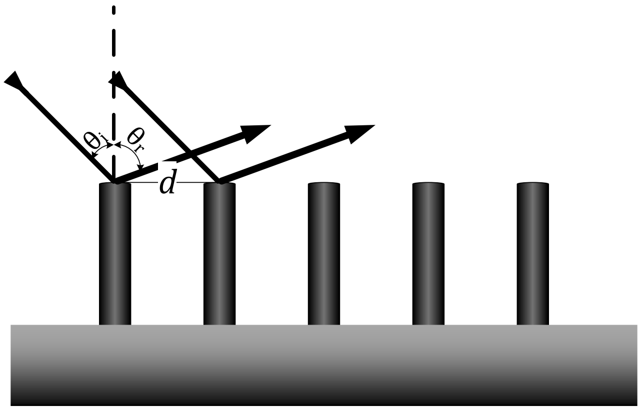

Figure 7.1: Geometric illustration of the diffraction effect, and the variables appearing in equation 7.1.

yielding the well-known grating equation [73],

$$\mathrm{n}_1(\sin\theta_i \pm \sin\theta_r) = \frac{\mathrm{m}\lambda}{\mathrm{d}} \tag{7.2}$$

which in the case of normal detection angle reduces to,

$$\mathrm{n}_1 \sin\theta_i = \frac{\mathrm{m}\lambda}{\mathrm{d}} \tag{7.3}$$

where n_1 is the refractive index of the surrounding medium and m is the order of the diffraction. Diffraction only occurs for values where $m\lambda/n_1d \leq 1$, and for wavelengths of light in the visible range (390 – 750 nm), a lower limit on the groove spacing is established. The total dispersion angle of the grating for radiation between wavelengths λ and $\lambda+\Delta\lambda$ is easily determined, and is generally linear for wavelengths below ~ 600 nm, with the dispersion angle decreasing for higher lattice spacing.

7.1.2 Experimental Setup for Diffraction Measurements

A schematic of the experimental setup is shown in Fig. 7.2. An off-the-shelf white LED light source, with a collimating lens, was used for illuminating the nanowires. The angle of the incidence of the light was varied to generate different colours. Diffracted light was captured with a simple microscope objective using a 0.25 N.A. 5× objective. The light was either sent to a built in 5 MP digital camera providing an image resolution of 3560 × 2860, or was coupled to an Ocean optics USB-4000 spectrometer to measure the spectral features of the generated colours. The objective of the microscope provided spatial filtering of light to only capture the diffracted elements within a small angle. For the sensing experiments, refractive index fluids obtained from Cargille (USA), ranging from n = 1.30 to 1.38 [74], were introduced onto the SiNW arrays by placing 2 mL drops of each fluid near the arrays on the silicon wafer. The fluid is oil based and therefore easily flows over the silicon surface.

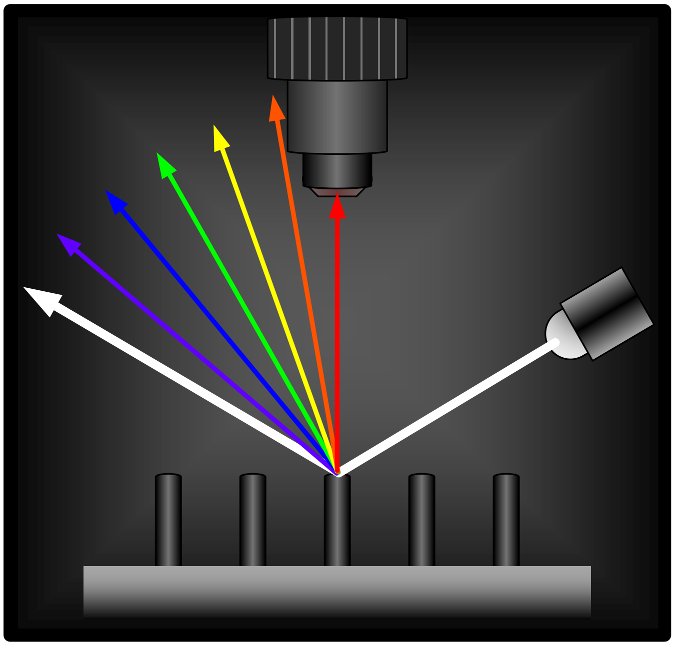

Figure 7.2: Diagram of the experimental setup to observe and measure diffracted colours from silicon nanowire arrays.

7.1.3 Colour Generation and Measurement of Nanowire Pitch Using Diffraction

A brightfield image of the SiNW arrays is shown in Figure 7.3, demonstrating the colour generation due to the waveguiding properties of the nano structure [7,8]. In a bright field setup, the images are taken with the incident light normal to the sample. In all of arrays, the diameter of each SiNW is 135 nm, while the lattice constant varies from 200 nm to 1700 nm. It is instructive to see that the colours change significantly for lattice spacing values between 200 nm to 1000 nm, and do not change much after that. As the lattice spacing is increased, the Silicon nanowires begin acting like individual waveguides, and the results can be understood in terms of the discussion presented previously in the literature [7]. As the spacing between the wires is decreased, strong electromagnetic near field coupling can occur which alters the mode properties of the array [8]. Since this is a resonant effect, there is dependence on the spacing between the nanowires and explains the strong dependency of colour on spacing, but makes it difficult predicting what the colour will be. To contrast these results, Figure 7.4 shows the same arrays imaged with the light source incident at a 40 degree angle to the Si nanowire arrays. The images were taken at normal to the sample as shown in Figure 7.1. Since light does not diffract off the surface where nanowires are not present, the background looks completely black as opposed to Figure 7.3. Very sharp, easily tuned metallic like colours are observed, which depend on the spacing between the nanowires. Further, as the spacing is increased, the colour shifts from blue to red and for spacings of 1200 nm and 1300 nm, has moved out of the visible range resulting in no lighting up of the arrays. Colours generated by the diffractive method contain a narrowband of wavelengths whereas in the brightfield images, the colours are generated by mixing of different wavelength components. As such, while colours like brown could be generated in the brightfield, the same cannot be generated in diffractive method. However, because only single wavelengths are diffracted at a particular angle, predictive modeling is very easy.

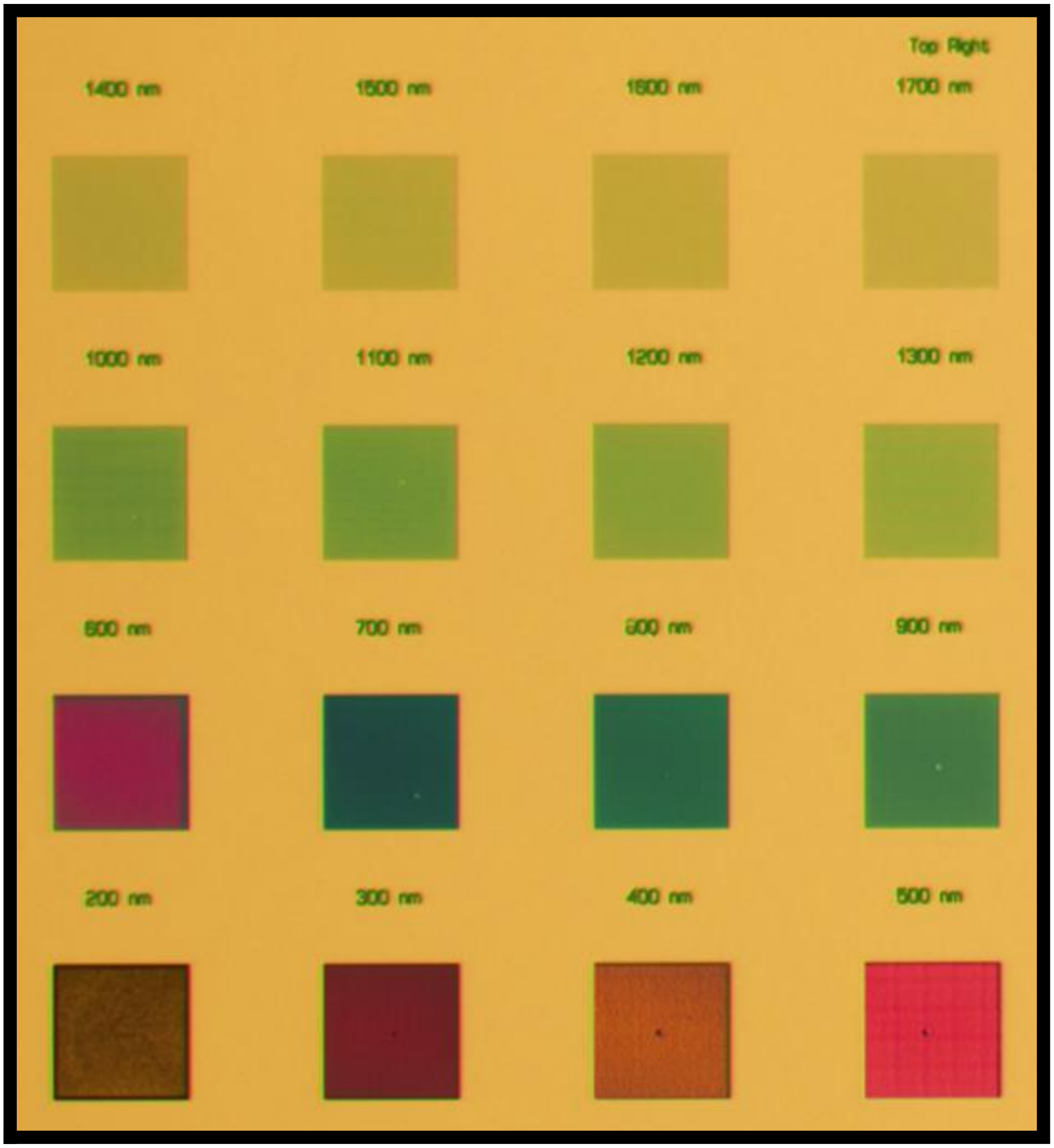

Figure 7.3: Brightfield images of SiNW arrays, with lattice spacing varying from 200 nm to 1700 nm. Vivid colour are observed especially for lattices with smaller spacing, where resonant coupling becomes important.

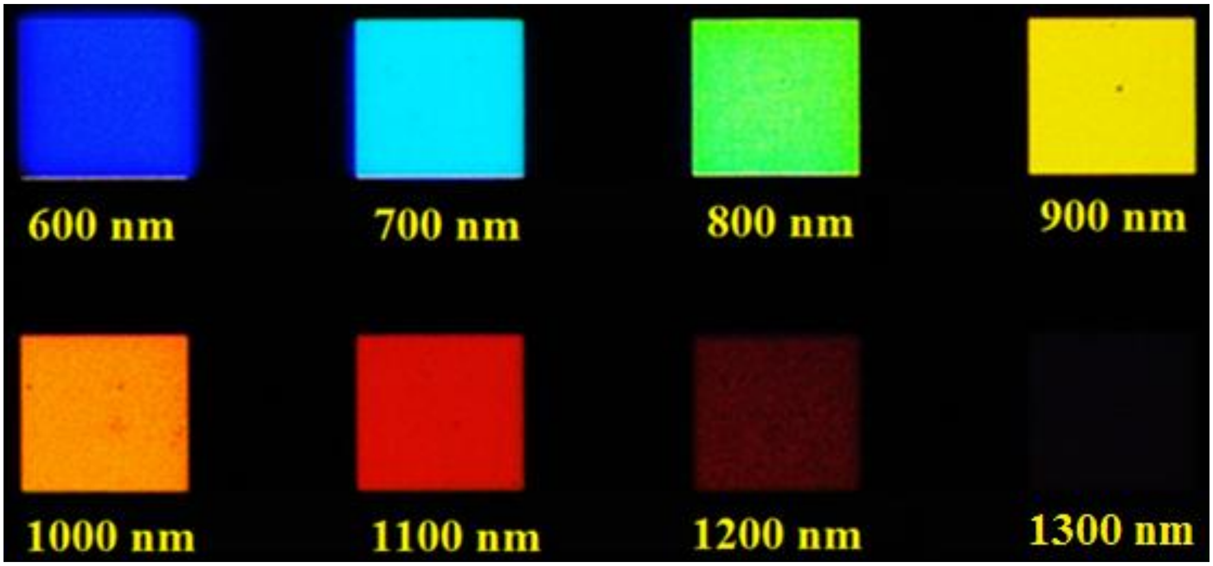

Figure 7.4: Colour generation from SiNWs with lattice spacing ranging from 600 nm to 1300 nm when imaged with a white LED light source incident at a grazing angle. Vivid primary colours are observed, which so far, have been difficult to generate in a bright field setup.

In order to confirm the idea that the generated colours are due to the diffractive properties of the array structure, a spectral measurement was performed using the same experimental setup diagrammed in Figure 7.2. A different sample consisting of three arrays with lattice spacings of 600 nm, 700 nm, and 800 nm was used. The three arrays were spaced 1 mm apart so that at any one time, only one array contributes to the diffracted signal unlike the previous sample where 12 samples are within the field of view of the microscope. The measurement was performed at an angle of incidence equal to approximately 50º. The normalized diffracted spectra from the three different NW arrays are shown in Figure 7.5, demonstrating that the peak intensity of diffracted light occurs at three distinct wavelengths. The results are summarized in Table 7.1 and are compared to the expected first-order diffracted wavelengths for each array. A very good agreement between the experimentally observed values, and those predicted by simple Bragg theory can be seen, demonstrating that diffraction is mainly responsible for the narrow band colour reflections and vivid colours achieved. Moreover, one clearly can see that this simple spectral method using diffractive could be used to measure nanowire spacing.

Spectral broadening is also observed as the spacing between the NWs increases, and is readily understood in terms of the angular dispersion associated with each grating. In the context of simple Bragg theory, the angular dispersion is readily obtained by differentiating equation 7.1,

$$\frac{\mathrm{d}\theta}{\mathrm{d}\lambda} = \frac{\mathrm{m}}{\mathrm{d}\cos\theta} \qquad 7.4$$

As the lattice spacing increases, the total dispersion angle of the grating decreases, allowing a larger distribution of diffracted wavelengths to enter the microscope objective. This leads to the observed increased spectral broadening as the array spacing is increased.

Table 7.1. Measured diffracted wavelengths versus lattice spacing.

Lattice Spacing (nm)	Peak Wavelength (nm)	Predicted Peak Wavelength (nm)
600	455	453
700	526	528
800	596	603

Further, for the results shown in Figure 7.5, the incidence angle was close to 50º, while for Figure 7.4, it was close to 40º. Very good agreement is also achieved with this change of angle. For example, for 800 nm at 50º incidence, the reflected peak is at ~ 600 nm. If the angle of incidence is changed to 40º, then the expected reflected peak should be at 514 nm which is fluorescent green colour. This is exactly what is seen in Figure 7.4. In order to further confirm this, colour generated from SiNW array a lattice spacing of 700 nm was measured for three different incident angles of 35, 50 and 65 degrees and the generated colours are shown in Figure 7.6. Visibly pure red, green, and blue colour generation is achieved from the same array. The colour generated also matched well with the spectral measurements for the 700 nm lattice spacing at 50 degrees, providing confirmation that the colour generated by changing the angle of incidence is well described by Bragg theory. It is well accepted that human vision is based on a trichromatic response system, in which red, green, and blue are the primary colours. As such, the tunable red, green, and blue response from the SiNWs can be used to create colour pixels for various imaging and display technologies.

The Bragg diffraction equation does not have a diameter dependence of the periodic structure, and in keeping with this similar colour should be observed from nanowires with the same lattice constant and different diameters. This is verified in the image in Figure 7.7, where green is seen for two different SiNW diameters of 85 nm and 200 nm, arranged in square lattices, spaced 600 nm apart. The observed colours from each array have the same hue, and do not display the sharp changes in colour generation resulting from a change in lattice constant as seen in Figure 7.4, again confirming the idea that the simple Bragg diffraction describes the colours well. Further, as demonstrated previously, this is not the case in the brightfield images, where the observed colour

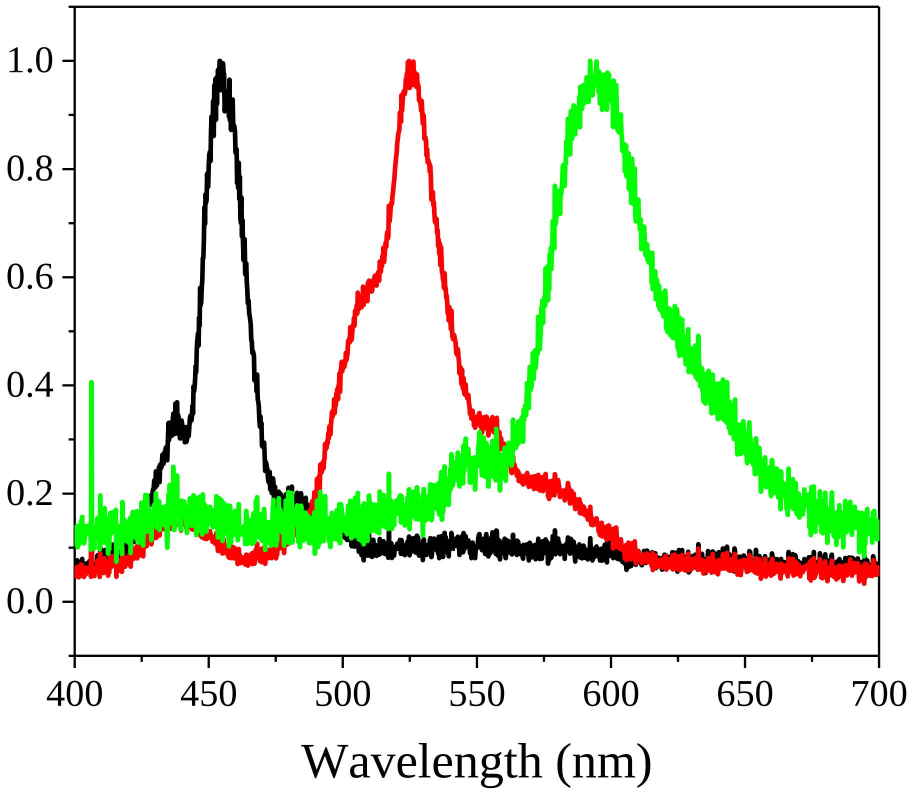

Figure 7.5 Spectral measurement of diffracted wavelengths for three different lattice spacings of 600 nm (blue), 700 nm (green) , and 800 nm (oranges) for an incident angle of 50̊. All spectra have been normalized to unity intensity.

is not easily predicted, and strong diameter dependence is observed. Colours generated by silicon nanowires in diffraction and brightfield images can be used for quality control in a foundry as these devices become commercial. Looking at the colours generated in diffraction, one can ascertain whether the pitch of the arrays is within specifications. Then using the colour generated in brightfield imaging, one can ascertain the accuracy of the diameter [7,8]. Thus, simple optical image based quality control system can be built for in-line inspection without the use of expensive and time consuming SEM imaging.

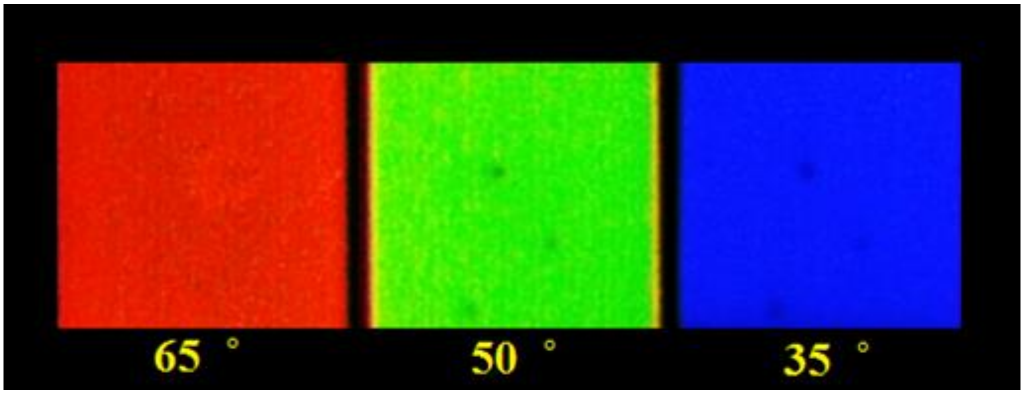

Figure 7.6: Diffracted colour vs incident angles of 35°, 50°, and 60° from a SiNW array with a 700 nm lattice spacing. All three RGB primaries are easily generated and are understood using Bragg theory.

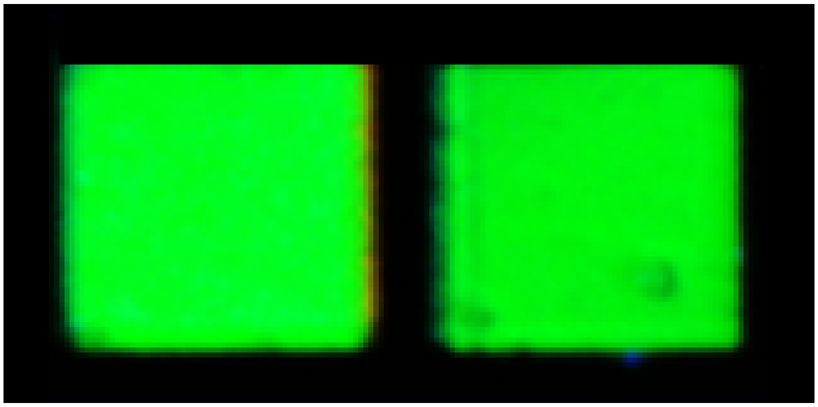

Figure 7.7: Diffracted colour vs SiNW diameter for a constant lattice spacing of 600 nm, for different diameters of 80 nm and 200 nm. The same hue (colour) is observed in both cases, supporting the Bragg interpretation for colour generation in the current experimental setup, this is not the case for nanowires illuminated in a bright field configuration.

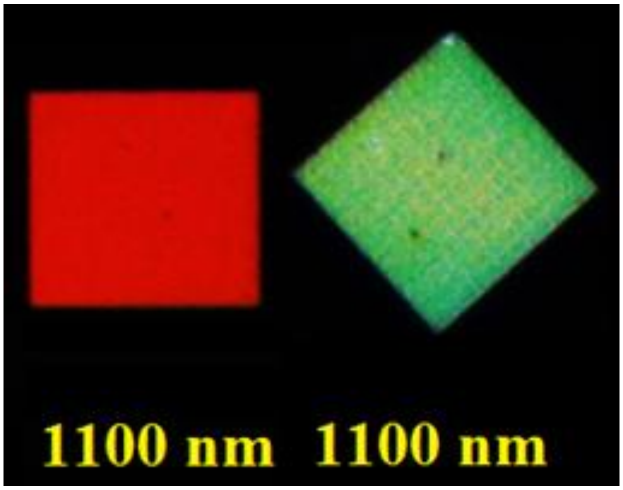

Figure 7.8: Two orientations of SiNW nanowire arrays with respect to the incident beam (45° and 90°). For 45°, a new set of Bragg planes emerges, resulting a √2 decrease in the lattice spacing as compared to the case where light is incident normal to the array edge, and thus different colours can be generated from the arrays in this fashion as well.

Since, $m\lambda/n_1d \leq 1$ for the diffraction equations to hold, it suggests colours will not be produced for spacing's smaller than the wavelength. This was confirmed by using nanowires spaced 200 nm apart and no colours could be generated. As the spacing was increased to 400 nm, only a faint blue colour could be generated at very sharp grazing angles of incidence. Thus, if different colours, spanning the visible range are to be generated from one array by changing the incident angle of incidence, the spacing between the nanowires has to be greater than ~600 nm.

When nanowires are arranged in a square lattice, additional Bragg planes are formed along the diagonal directions, with different interplane separation distances. In keeping with this, changes in the colour which appears should change when the light is incident along one of these Bragg planes. If one imagines illuminating the arrays from the corner, which is at 45 degrees, the spacing effectively decreases by a factor of √2, and the colour diffracted should blueshift accordingly. This effect is shown in Figure 7.8 where SiNWs spaced of 1100 nm apart are able to generate both red and green colours. Once again the results are close to what is expected, and suggest that one can fabricate a simple optical alignment sensor. For many optical applications, alignment of components and chips along a certain direction is required. By using the fact the SiNW arrays only light up when the Bragg planes formed by the wires are aligned to the source, an alignment sensor can be achieved. For example, two dimensional grating have been used to demonstrate accurate measurement of orthogonality with a standard error of 0.28 arcsec [75]. The same should be achievable by colour imaging and is under further study. Further distinction between orientations can be made possible by changing the lattice type to a rectangular lattice for example, or by the placing nanowire arrays on different rotational axis.

To summarize, the various images confirm that the colours are indeed coming through only the diffractive properties of the silicon nanowires. The colours generated are more easily tuned and more vivid than those observed in a brightfield setup. Additionally, the ability to create different colours from the same array was demonstrated, including red, green, and blue, which are the primary colours in displays. The efficiency of the light diffracting effect produced by the square lattice arrangement of nanowires is still currently unknown and could be a topic of a future study.

7.1.4 Linear Refractive Index Sensing

Diffracted colours from the SiNWs can be used to demonstrate a simple colourimetric refractive index sensor. The main advantage for using cylindrical nanowires arranged in square lattices as opposed to grooved types of structures is to ensure that fluid introduction upon the grating is able to enter the channels irrespective of the orientation of the sample with respect to the direction of fluid flow. This becomes especially important when thin films fluids are being studied, and for a one-dimensional groove structure, this would require that all of the channels are well filled, which might not be feasible. Isotropic filling is easily achieved in the square lattice of cylindrical nanowires, which have no preferential orientation for efficient fluid filling.

Refractive index sensing is generally realized by measuring a change in the resonance condition resulting from changes in the refractive index. The diffracted wavelength and hence, the colour reflected by the 2-dimensional SiNW gratings is dependent on the refractive index of the surrounding medium. When the refractive index changes from n to $n+\Delta n$, and the incident and detection angles are left constant in the experimental setup, the change in wavelength of light appearing at the detector is independent of lattice spacing and is given by

$$\Delta\lambda = \frac{\lambda_1 \Delta n}{n} \tag{4.5}$$

where λ_1 is the diffracted wavelength for a refractive index n. It can be seen that the sensitivity increases for larger values of λ_1. If a spectral measurement is to be done, it is better to set up the experiment for as long a diffracted wavelength as the detector and source will allow for. In contrast, if the diffracted colour is to be used as a sensing mechanism, without a spectrometer, one must choose a starting wavelength, or colour, which would subsequently result in a visible colour change, and hence larger changes in the RGB triad values. The most perceptible colour changes happen in the wavelength range spanning from 550 nm to 600 nm. For example, if the experiment is set so that yellow (~ 590 nm) is seen in the images for an initial refractive index n. Then for an index change of $\Delta n = 0.08$, the colour corresponding to 633 nm will be observed, which is red, and thus high changes in the RGB can be achieved. In contrast, if λ_1 were 650 nm, which is also red, then refractive index changes will result in a final wavelength of 690 nm, which is still again red, and consequently minimal changes in the RGB values will be observed. Thus, by appropriately choosing the initial diffracted wavelength, a refractive index sensor can be achieved by measuring changes in colour. One significant advantage of using the grating effect is that as seen by equation 7.5, the response to changes in refractive index is linear, and the colour changes are predictable. This scenario is not the case for the sensing applications operating in a bright field setup, where the ability to tune the colour for versus index changes becomes more difficult, and is also the case in proposed applications in which sub-wavelength gratings have been designed for colour generation [76-78].

By choosing the initial wavelength of 590 nm, R and B values can be held constant and G values changed, leading to simple image processing and data analysis. For design optimization, the wavelength range which spans from 580 nm to 700 nm can in fact be modelled by using the RGB colour space in which only the green value is linearly varied, and the R and B values are held at 255 and 0, respectively.

$$\begin{cases} R = 255 \\ G = -3.9\lambda + 2529 \quad for\ 580nm \leq \lambda \leq 700\ nm \\ B = 0 \end{cases} \qquad 7.6$$

This design idea was tested using one SiNW array under the experimental conditions described in the previous section, and controlled refractive index fluids were introduced onto the array. The corresponding images were taken using a 5 MP camera attached to a microscope. Nanowire array with spacing of 700 nm were used for the demonstration. The incident angle was tuned such that after the introduction of the $n = 1.30$ index fluid, yellow was achieved in the diffracted image. Different index fluids of 1.32, 1.34, 1.36 and 1.38 index fluids were each subsequently introduced and images were taken. The comparison between the RGB values predicted by the design described above, and those from the experiment, for the range of refractive indices studied, are shown in Figure 7.9a. Shown also are both the predicted and experimental colours observed for each refractive index. The agreement between the experimental data and the proposed design is clear. By starting in the yellow, in order to minimize blue contribution, one is able to isolate the change in refractive index to changes only in the green colour content. Furthermore, changes in refractive index around yellow did result in visible colour changes allowing the human eye to act as the detector. The results clearly show that linear sensing of refractive index changes is possible, with a theoretical refractive index detection limit of ~ 5×10^{-4} ,assuming a change of 1 in the value of G is a distinct colour. The excellent agreement between the experimentally observed and predicted colours validates that a simple approach to the design, can allow for the fabrication of a linear sensor with large sensitivities to changes in the refractive index of the local fluid environment, without the need for a spectrometer or expensive optics.

It should be pointed out that certain colours, or hues, can show significant changes in RGB values simply due to changes in luminosity. For example, the luminosity may change due to different thickness of fluids in the experiments. In order to make sure, the colour changes with different refractive indices were indeed due to diffraction and not experimental variations like changes in saturation or luminosity of a given colour, the corresponding RGB values obtained were mapped to another colour space which uses Hue, Saturation, and Luminosity as the basis to form what is known as the HSL colour space. The results in Figure 7.9b demonstrate the stability of the luminosity and saturation values for the experimentally observed colours, and shows that only the hue is changing, confirming that only colour changes are taking place. By using the HSL colour space, it is easily determined whether or not decomposed images are indeed changing only in colour, thereby eliminating false positives caused by changes in fluid height and poor fluid geometries (droplets etc.).

Besides doing the simple colour measurements to achieve sensing, spectral measurements can also be used with a higher sensitivity of measurements. Diffracted spectra are shown in Figure 7.10, when the nanowires are surrounded by air (black), and fluids of refractive indices 1.300 (red) and 1.305 (blue). The sample had a pitch of 800 nm and was illuminated at an incident angle of ~ 50º. Fits to the data are also plotted. Clear shifts in spectrum are observed as the refractive index of the surrounding medium changes by 0.05. The refractive index of 1.300, produces a peak wavelength of 608.9 nm and shifts to 611.0 nm for a refractive index change of +0.005. The results match well with equation 7.4 which predicts a wavelength shift of 2.3 nm instead of the 2.1 nm achieved experimentally. This results in a sensitivity of 400 nm/RIU. The sensitivity is better than photonic integrated circuits [79] and uses very simple coupling optics. As seen by equation 7.4, we can increase the sensitivity by operating at a higher wavelength as in this measurement we are not limited to visual colour changes. For example, if the operating wavelength was increased to 800 nm, then a sensitivity of 533 nm/RIU can be expected. With a wavelength resolution of 1 pm, this can allow for a refractive index resolution of 2×10^{-6}, similar to those achieved in surface plasmonic sensors [80,81]. However, unlike surface plasmons which require critical coupling conditions normally using prisms, the diffractive silicon nanowire sensor uses very simple off-the shelf microscope objectives.

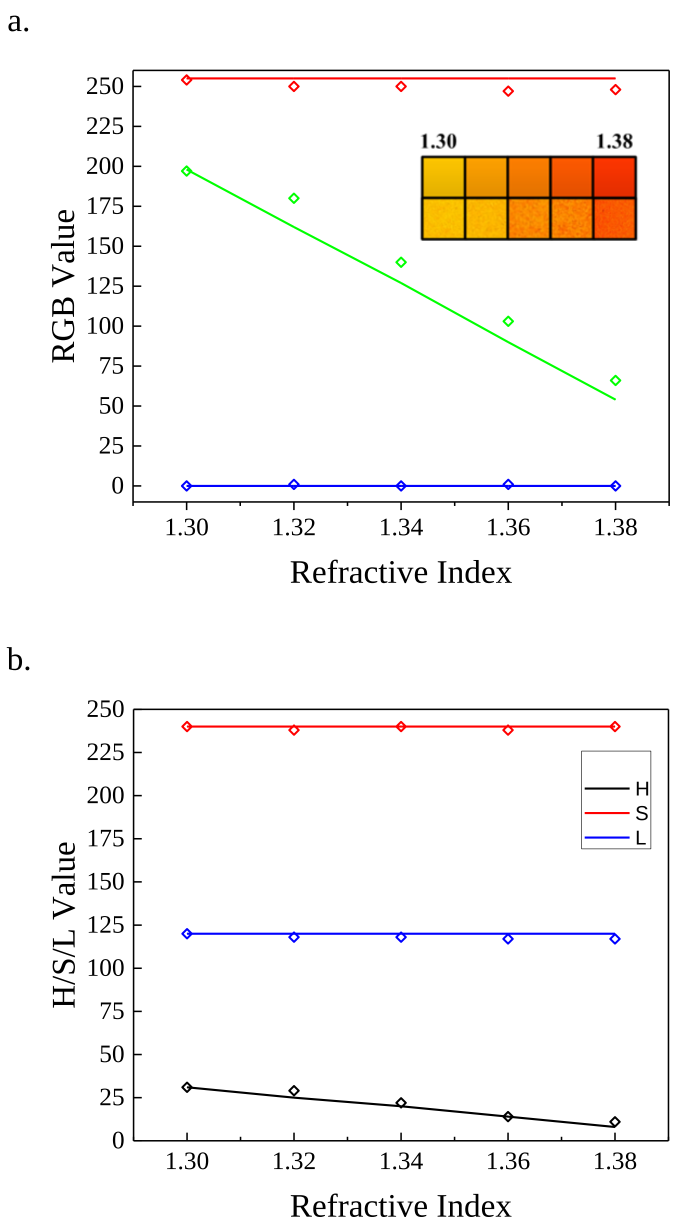

Figure 7.9: Comparison between the experimental RGB (a) and HSL(b) values, and theoretical values predicted (solid lines) by the design, and (c) the experimentally observed colour versus the colours that were expected to be seen.

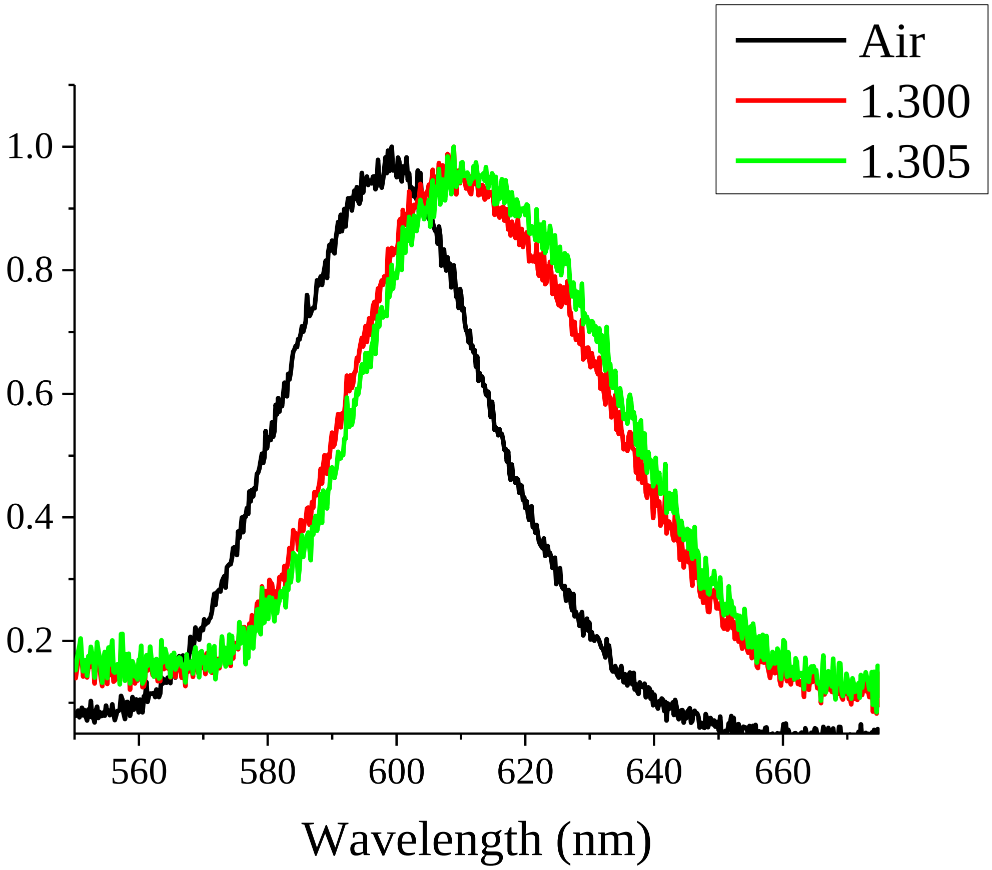

Figure 7.10: A spectral measurement for two different refractive index fluids of 1.300 (open red circles) and 1.305 (open blue circles). Air is shown for reference (open black circles) as well as the fits to the data (solid lines).

Controlled and predictable colour generation from 135 nm diameter SiNWs, arranged in square lattices with lattice constants varying from 400-1700 nm has been demonstrated using simple Bragg theory to guide the design. The colours which are generated are well defined and do not appear dull or faded, and span the entire visible range from deep blue, to bright red. The vivid colours produced demonstrate the capability of SiNWs to be used as a monochromator-on-a-chip. The controlled colour generation also allows for a possible CMOS compatible display application, without the use of pigments. In addition, by taking advantage of the relatively simple physics which causes the colour generation, a refractive index sensor was designed which produces a linear response to the change in refractive index, and the capability to resolve index changes on the order of 5×10^{-4} has been demonstrated by measuring simply the colour changes. Furthermore, this sensing has been achieved without the use of a spectrometer or expensive optics, and requires a white LED source and less than $100 of optics, which includes a digital camera, and a computer to analyze the images. The sensitivity can be increased to 2×10^{-6} if spectral measurements are conducted. Again low cost and alignment insensitive optics was used even with the spectral measurements.

7.2 Nanowire Colour Laser Printing

Strucutral colour generation using nanostructures presents an attractive alternative to dye. Nanostructures allow for the realization of colours that won't fade over time [35]. Additionally, the use of nanostructures can allow for reduced pixel areas, and sub-wavelength resolutions [40,35] and have been demonstrated in gratings, nanowires, and plasmonic nanostrucutres [8,9,40,35]. Colour patterns are generally created by varying the geometrical properties of the nanostructures within an array, usually by EBL. This technique is neither cost effective nor suitable for large scale processes. In this connection, it was demonstrated very recently that transient laser heating of an array of plasmonic nanostructures can be used to print colour patterns into the array [35]. The changes in the generated structural colour result from various degrees of melting of the plasmonic disk. In Chapters 5 and 6 it was shown that laser heating of vertical nanowires alters the chemical nature of GaAs and a-Si nanowires. This taken with the fact that nanowires generate vivid colours as seen in the previous section, one would expect that the decomposition of GaAs nanowires would result in changes to the structural colours seen in the modified areas.

Here it is demonstrated that the structural colour generation properties of vertical GaAs and a-Si nanowire arrays can be spatially modified using a focused laser beam. Unlike plasmonic structures, vertical semiconductor nanowires find important applications in solar energy harvesting [3-6]. More recently, there has been interest in colourful solar cells that can be integrated into buildings for aesthetically pleasing solutions. Naturally, an array of a-Si and c-Si arranged to produce various structural colour patterns would be of interest. The nanowires consist of semiconductor material, and unlike metals used in plasmonics, Raman analysis of the structural changes is possible, allowing for an overall understanding of the process (see Chapters 5 and 6). In this connection, photo-thermal printing of a-Si nanowire arrays allows for c-Si and a-Si nanowires, on the same substrate, with minimal fabrication steps. More generally, the fact that the vertical nature is maintained is attractive for researchers looking to make use of the any properties of both c-Si and a-Si on the same substrate.

Figure 7.11 shows a brightfield image of an array of 125 nm diameter GaAs nanowires that were modified using a 633 nm laser at 80 W/mm^2. Shown also is an SEM image of part of the modified area. Due to the limitations of the equipment the laser patterns seen had to written by hand and therefore the results presented should be considered only a proof of concept. The widths of the lines that were imprinted into the GaAs nanowire array are 2.5-3 µm. The same effect is seen from vertical a-Si nanowires in Figure 7.12. Here, an array of 105 nm diameter a-Si nanowires were modified using a 533 nm laser at ~ 480 W/mm^2, and the letters UW corresponding to the University of Waterloo clearly appear in the optical image and were formed by creating a dot

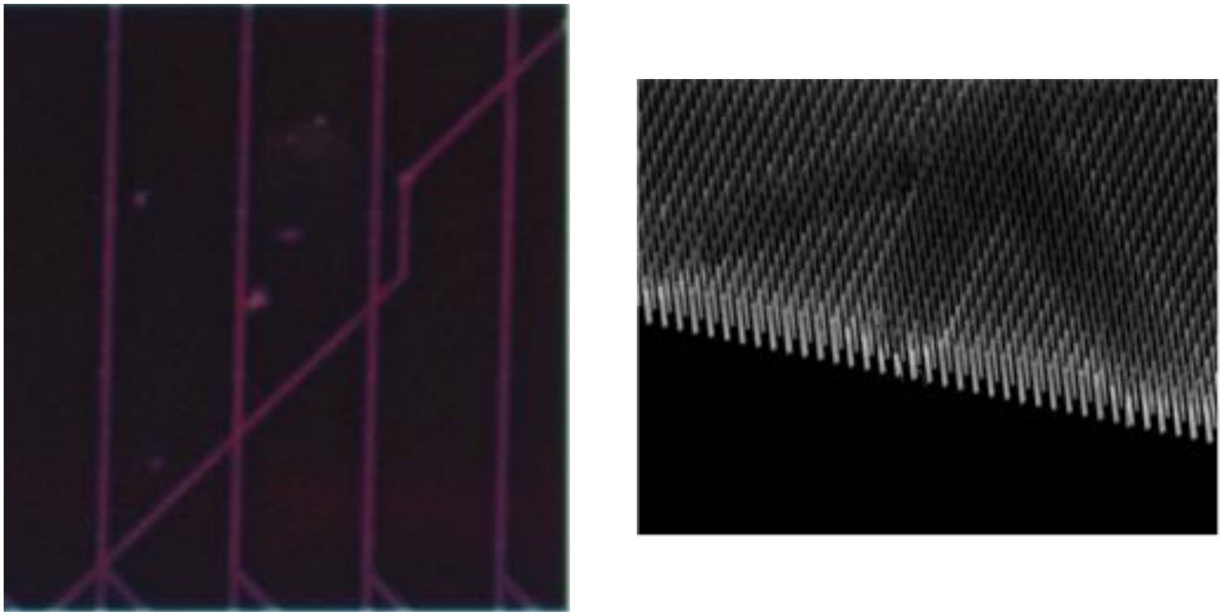

Figure 7.11: A brightfield image of the GaAs nanowire array showing the demonstrating photo-thermal laser printing at 10000 DPI. An SEM image of a section of the modified area is also shown.

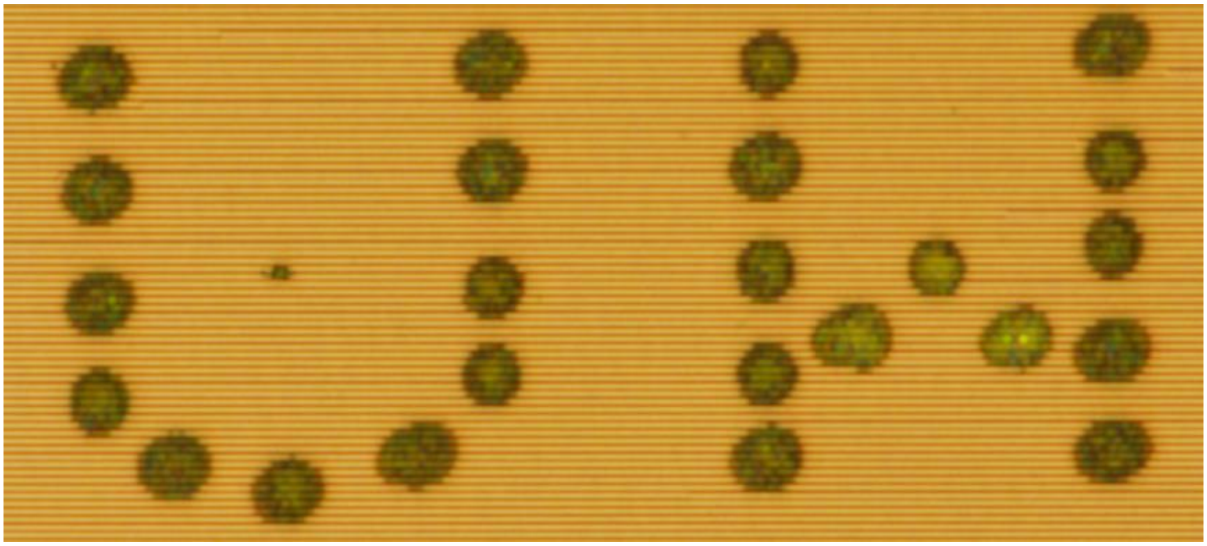

Figure 7.12: The letters UW written into an a-Si nanowire array using a laser. The dots consist of c-Si and were realized using photo-thermal modification as discussed in Chapter 6.

pattern. As we know from the previous chapter, the dots making up the letters consist of c-Si, and background is a-Si.

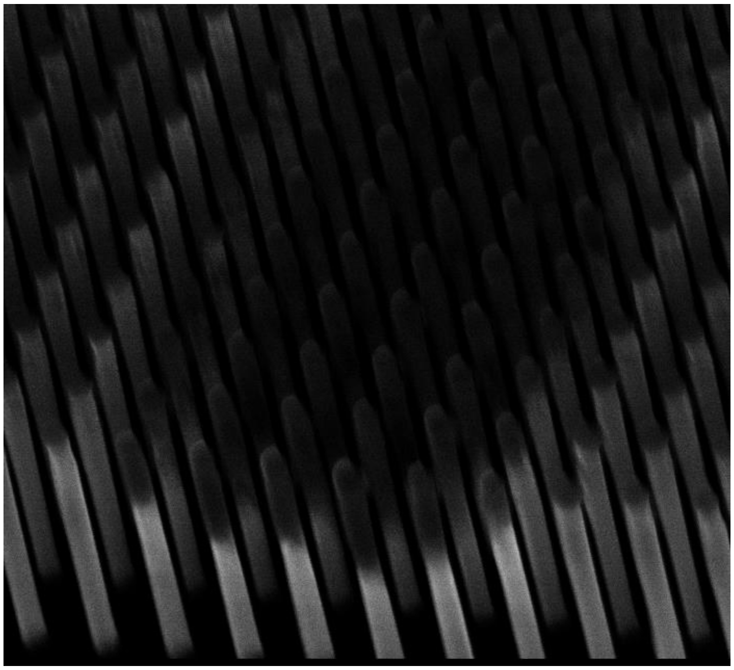

Figure 7.13: A higher magnification SEM image of the edge of the modified nanowires from Figure 7.11.

This technique allows for printing in a resolution of up to 10000 dots per inch (DPI). It should be possible to decrease this linewidth and restrict modification to a single row of nanowires, and increase the resolution. A higher magnification SEM image showing the edge of one of the modified lines in the GaAs nanowire array is shown in Figure 7.13. The maximum depth to which the nanowires are modified is at the centre of the spot, and falls off rapidly towards the edges. Thus, by lowering the laser power, one can modify a smaller area of nanowires. Beyond this, by using just the right amount of power so there is enough energy in the center of the laser spot to induce changes in GaAs or a-Si would allow for the modification of a single nanowire, and up to

~ 125000 DPI if the nanostructures were spaced 200 nm apart [35]. More importantly, the process can be monitored in real time using Raman spectroscopy, which is not possible with plasmonic laser printing. Demonstrating this concept, and how modification depth changes the structural colours observed is a topic of future interest. Additionally, understanding the optical absorption properties from arrays of nanowires that have been modified warrants a full study.

CHAPTER 8

Summary and Future Work

Before this work was concluded, the Raman spectral features of Si, GaAs, and a-Si nanowires were limited to cases involving horizontal nanowires. Significant progress was made towards understanding phonon confinement, thermal effects, and crystalline quality of samples.

In this work, it is shown that Raman spectroscopy can be used to characterize the optical waveguiding nature of vertical Si, GaAs, and a-Si nanowire arrays. The results have shown that the resonant diameter for an incoming light field can be determined by measuring the RIV for each material. The enhanced intensities are the result of strong coupling into the HE_{11} mode.

Some interesting aspects on how the excitation of HE_{11} mode and Raman spectroscopy can be applied to vertical nanowires have been brought into light. Firstly, it was demonstrated that Raman spectroscopy and waveguiding can be used to realize and measure significant temperature increases in GaAs nanowires. Through proper choice of diameter for an incoming wavelength, the highest temperatures were realized.

Secondly, Raman spectroscopy was used to monitor structural evolution in GaAs nanowire arrays resulting from overheating. It was shown that Raman spectroscopy can be used to measure the formation of c-As in real time. Furthermore, it was demonstrated that the power required to induce structural degradation in vertical nanowires is reduced by three orders of magnitude relative to horizontal ones when the HE_{11} mode is excited.

Thirdly, how excitation of the HE_{11} mode affects crystallization of a-Si nanowires was investigated. It was observed that the highest quality silicon crystals were formed due to the initial excitation of the HE_{11} mode in a-Si, but the lowest crystalline volume fraction. For the larger diameter nanowire samples, the crystalline volume fraction was almost 100 %. This can be explained by the shift in resonance condition that occurs as the samples begin to crystallize.

Lastly, during the course of the Raman measurements it was observed that nanowire arrays generate structural colours. A diffractive method for measuring the spacing between nanowires was introduced, and was extended to realize a linear refractive index sensor capable of a resolution of 400 nm/RIU. Also the preliminary aspects of photo-thermal colour laser printing using nanowire arrays was presented.

Recommendations for future work include the following:

- Experimentally verifying that length plays a significant role in generating heat from an incoming light field.
- Experimentally measuring photo-thermal activity in other Semiconductor materials such as InAs
- Making an effort to experimentally measure the thermopower of vertical nanowires.
- Correlating the structural changes seen in the Raman spectra with colour changes observed in the microscope to further the idea of photo-thermal printing optical properties into nanowire arrays.

BIBLIOGRAPHY

[1] Johnson, J. C., Choi, H. J., Knutsen, K. P., Schaller, R. D., Yang, P., & Saykally, R. J. (2002). Single gallium nitride nanowire lasers. *Nature materials*,*1*(2), 106-110.

[2] Duan, X., Huang, Y., Agarwal, R., & Lieber, C. M. (2003). Single-nanowire electrically driven lasers. *Nature*, *421*(6920), 241-245.

[3] Garnett, E. C., Brongersma, M. L., Cui, Y., & McGehee, M. D. (2011). Nanowire solar cells. *Annual Review of Materials Research*, *41*, 269-295.

[4] Garnett, E., & Yang, P. (2010). Light trapping in silicon nanowire solar cells.*Nano letters*, *10*(3), 1082-1087.

[5] Tsakalakos, L., Balch, J., Fronheiser, J., Korevaar, B. A., Sulima, O., & Rand, J. (2007). Silicon nanowire solar cells. *Applied Physics Letters*, *91*(23), 233117.

[6] Law, M., Greene, L. E., Johnson, J. C., Saykally, R., & Yang, P. (2005). Nanowire dye-sensitized solar cells. *Nature materials*, *4*(6), 455-459.

[7] Seo, K., Wober, M., Steinvurzel, P., Schonbrun, E., Dan, Y., Ellenbogen, T., & Crozier, K. B. (2011). Multicolored vertical silicon nanowires. *Nano letters*,*11*(4), 1851-1856.

[8] Khorasaninejad, M., Abedzadeh, N., Walia, J., Patchett, S., & Saini, S. S. (2012). Color matrix refractive index sensors using coupled vertical silicon nanowire arrays. *Nano letters*, *12*(8), 4228-4234.

[9] Walia, J., Dhindsa, N., Khorasaninejad, M., & Saini, S. S. (2014). Color Generation and Refractive Index Sensing Using Diffraction from 2D Silicon Nanowire Arrays. *Small*, *10*(1), 144-151.

[10] Park, H., & Crozier, K. B. (2013). Multispectral imaging with vertical silicon nanowires. *Scientific reports*, *3*.

[11] Patolsky, F., & Lieber, C. M. (2005). Nanowire nanosensors. *Materials today*,*8*(4), 20-28.

[12] Patolsky, F., Zheng, G., & Lieber, C. M. (2006). Nanowire sensors for medicine and the life sciences.

[13] Wan, Q., Li, Q. H., Chen, Y. J., Wang, T. H., He, X. L., Li, J. P., & Lin, C. L. (2004). Fabrication and ethanol sensing characteristics of ZnO nanowire gas sensors. *Applied Physics Letters*, *84*(18), 3654-3656.

[14] Hu, S., Chi, C. Y., Fountaine, K. T., Yao, M., Atwater, H. A., Dapkus, P. D., ... & Zhou, C. (2013). Optical, electrical, and solar energy-conversion properties of gallium arsenide nanowire-array photoanodes. *Energy & Environmental Science, 6*(6), 1879-1890.

[15] Boukai, A. I., Bunimovich, Y., Tahir-Kheli, J., Yu, J. K., Goddard Iii, W. A., & Heath, J. R. (2008). Silicon nanowires as efficient thermoelectric materials.*Nature*, *451*(7175), 168-171.

[16] Hochbaum, A. I., Chen, R., Delgado, R. D., Liang, W., Garnett, E. C., Najarian, M., ... & Yang, P. (2008). Enhanced thermoelectric performance of rough silicon nanowires. *Nature*, *451*(7175), 163-167.

[17] Li, D., Wu, Y., Kim, P., Shi, L., Yang, P., & Majumdar, A. (2003). Thermal conductivity of individual silicon nanowires. *Applied Physics Letters*, *83*(14), 2934-2936.

[18] Soini, M., Zardo, I., Uccelli, E., Funk, S., Koblmüller, G., i Morral, A. F., & Abstreiter, G. (2010). Thermal conductivity of GaAs nanowires studied by micro-Raman spectroscopy combined with laser heating. *Applied Physics Letters*,*97*(26), 263107.

[19] Walia, J., Dhindsa, N., Flannery, J., Khodabad, I., Forrest, J., LaPierre, R., & Saini, S. S. (2014). Enhanced Photothermal Conversion in Vertically Oriented Gallium Arsenide Nanowire Arrays. *Nano letters*, *14*(10), 5820-5826.

[20] Yazji, S., Zardo, I., Soini, M., Postorino, P., i Morral, A. F., & Abstreiter, G. (2011). Local modification of GaAs nanowires induced by laser heating.*Nanotechnology*, *22*(32), 325701.

[21] Śliwa, C., & Dietl, T. (2011). Thermodynamic and thermoelectric properties of (Ga, Mn) As and related compounds. *Physical Review B*, *83*(24), 245210.

[22] Warren, M. V., Wood, A. W., Canniff, J. C., Naab, F., Uher, C., & Goldman, R. S. (2012). Evolution of structural and thermoelectric properties of indium-ion-implanted epitaxial GaAs. *Applied Physics Letters*, *100*(10), 102101.

[23] Martin, P. N., Aksamija, Z., Pop, E., & Ravaioli, U. (2010). Reduced thermal conductivity in nanoengineered rough Ge and GaAs nanowires. *Nano letters*,*10*(4), 1120-1124.

[24] Da Silva, S. W., Galzerani, J. C., Lubyshev, D. I., & Basmaji, P. (1998). Surface phonon observed in GaAs wire crystals grown on porous Si. *Journal of Physics: Condensed Matter*, *10*(43), 9687.

[25] Besson, J. M., Itié, J. P., Polian, A., Weill, G., Mansot, J. L., & Gonzalez, J. (1991). High-pressure phase transition and phase diagram of gallium arsenide. *Physical Review B, 44*(9), 4214.

[26] Khorasaninejad, M., Walia, J., & Saini, S. S. (2012). Enhanced first-order Raman scattering from arrays of vertical silicon nanowires. *Nanotechnology*,*23*(27), 275706.

[27] Khorasaninejad, M., Dhindsa, N., Walia, J., Patchett, S., & Saini, S. S. (2012). Highly enhanced Raman scattering from coupled vertical silicon nanowire arrays. *Applied Physics Letters*, *101*(17), 173114

[28] Adu, K. W., Gutierrez, H. R., Kim, U. J., Sumanasekera, G. U., & Eklund, P. C. (2005). Confined phonons in Si nanowires. Nano letters, 5(3), 409-414.

[29] Campbell, I. H., & Fauchet, P. M. (1986). The effects of microcrystal size and shape on the one phonon Raman spectra of crystalline semiconductors. *Solid State Communications, 58*(10), 739-741.

[30] Fauchet, P. M., & Campbell, I. H. (1988). Raman spectroscopy of low-dimensional semiconductors. *Critical Reviews in Solid State and Material Sciences*, *14*(S1), s79-s101.

[31] B. Li, D. Yu and S. L. Zhang, “Raman spectral study of silicon nanowires” Phys. Rev., B 59, 1999.

[32] R. Wang, G. Zhou, Y. Liu, S. Pan, H. Zhang, D. Yu, Z. Zhang, “Raman spectral study of silicon nanowires: High-order scattering and phonon confinement effects” Phys. Rev. B, 61, 16827-16832, 2000.

[33] Z. Su, J. Sha, G. Pan, J. Liu, D. Yang, C. Dickinson, and W. Zhou, Temperature-Dependant Raman Scattering of Silicon Nanowires” J. Phys. Chem. B, 110, 1229-1234, 2006.

[34] Förster, J., & Vogt, H. (2011). Excimer Laser-Annealing of Amorphous Silicon Layers. *Simulation*, *88,* 90.

[35] Zhu, X., Vannahme, C., Højlund-Nielsen, E., Mortensen, N. A., & Kristensen, A. (2015). Plasmonic colour laser printing. *Nature nanotechnology*

[36] Gupta, R., Xiong, Q., Adu, C. K., Kim, U. J., & Eklund, P. C. (2003). Laser-induced Fano resonance scattering in silicon nanowires. *Nano Letters*, *3*(5), 627-631.

[37] Stroscio, M. A., & Dutta, M. (2001). *Phonons in nanostructures*. Cambridge University Press.

[38] Stroscio, M. A., Kim, K. W., Littlejohn, M. A., & Chuang, H. (1990). Polarization eigenvectors of surface-optical phonon modes in a rectangular quantum wire. *Physical Review B*, *42*(2), 1488.

[39] Ashcroft, N. W., & Mermin, N. D. (2005). Solid State Physics (Holt, Rinehart and Winston, New York, 1976).

[40] Cardona, M., & Merlin, R. (2007). *Light scattering in solids IX* (pp. 1-14). Springer Berlin Heidelberg.

[41] Dhindsa, N., Walia, J., Pathirane, M., Khodadad, I., Wong, W., Saini, S. (2016) Adjustable Optical Response of Amorphous Silicon Nanowires Integrated with Thin Films *Nanotechnology* Article reference: NANO-108792.R1 (in press)

[42] Temple, P. A., & Hathaway, C. E. (1973). Multiphonon Raman spectrum of silicon. *Physical Review B*, *7*(8), 3685.

[43] Uchinokura, K., Sekine, T., & Matsuura, E. (1972). Raman scattering by silicon. *Solid State Communications, 11*(1), 47-49.

[44] Uchinokura, K., Sekine, T., & Matsuura, E. (1974). Critical-point analysis of the two-phonon Raman spectrum of silicon. *Journal of Physics and Chemistry of Solids*, *35*(2), 171-180.

[45] Piscanec, S., Cantoro, M., Ferrari, A. C., Zapien, J. A., Lifshitz, Y., Lee, S. T., ... & Robertson, J. (2003). Raman spectroscopy of silicon nanowires. *Physical Review B*, *68*(24), 241312.

[46] Doerk, G. S., Carraro, C., & Maboudian, R. (2012). Raman Spectroscopy for Characterization of Semiconducting Nanowires. In *Raman Spectroscopy for Nanomaterials Characterization* (pp. 477-506). Springer Berlin Heidelberg.

[47] Fountaine, K. T., Whitney, W. S., & Atwater, H. A. (2014). Resonant absorption in semiconductor nanowires and nanowire arrays: Relating leaky waveguide modes to Bloch photonic crystal modes. *Journal of Applied Physics*, *116*(15), 153106.

[48] Huang, J. A., Zhao, Y. Q., Zhang, X. J., Luo, L. B., Liu, Y. K., Zapien, J. A., ... & Lee, S. T. (2011). Enhanced Raman scattering from vertical silicon nanowires array. *Applied Physics Letters*, *98*(18), 183108-183108.

[49] Smit, C., Van Swaaij, R. A. C. M. M., Donker, H., Petit, A. M. H. N., Kessels, W. M. M., & Van de Sanden, M. C. M. (2003). Determining the material structure of microcrystalline silicon from Raman spectra. *Journal of applied physics*, *94*(5), 3582-3588.

[50] Beeman, D., Tsu, R., & Thorpe, M. F. (1985). Structural information from the Raman spectrum of amorphous silicon. *Physical Review B, 32*(2), 874.

[51] Kraemer, D., Poudel, B., Feng, H. P., Caylor, J. C., Yu, B., Yan, X., Ma, Y., Wang, X., Wang, D., Muto, A., McEnaney, K., Chisea, M., Ren, Z., Chen, G. (2011). High-performance flat-panel solar thermoelectric generators with high thermal concentration. *Nature materials*, *10*(7), 532-538.

[52] Miyako, E., Nagata, H., Funahashi, R., Hirano, K., & Hirotsu, T. (2009). Light-Driven Thermoelectric Conversion Based on a Carbon Nanotube–Ionic Liquid Gel Composite. *ChemSusChem*, *2*(8), 740-742.

[53] Chen, Y., Chen, K., Bai, H., Li, L. (2012). Electrochemically reduced graphene porous material as light absorber for light-driven thermoelectric generator. *Journal of Materials Chemistry*, *22*(34), 17800-17804.

[54] Miyako, E., Hosokawa, C., Kojima, M., Yudasaka, M., Funahashi, R., Oishi, I., Hagihara, Y., Shichiri, M., Takashima, M., Nishio, K., Yoshida, Y. (2011). A Photo-Thermal-Electrical Converter Based On Carbon Nanotubes for Bioelectronic Applications. *Angewandte Chemie*, *123*(51), 12474-12478.

[55] Miyako, E., Nagata, H., Hirano, K., Makita, Y., Nakayama, K. I., Hirotsu, T. (2007). Near-infrared laser-triggered carbon nanohorns for selective elimination of microbes. *Nanotechnology*, *18*(47), 475103.

[56] Wang, S., Bai, Z., Yan, G., Zhang, H., Wang, J., Yu, W., & Fu, G. (2013). The enhancement of photo-thermo-electric conversion in tilted $Bi_2Sr_2Co_2O_y$ thin films through coating a layer of single-wall carbon nanotubes light absorber. *Optics Express*, *21*(15), 18336-18343.

[57] Wood, C. E. C., Singer, K., Ohashi, T., Dawson, L. R., & Noreika, A. J. (1983). A pragmatic approach to adatom-induced surface reconstruction of III-V compounds. Journal of Applied Physics, 54(5), 2732-2737.

[58] He, J., Chen, P., Lu, W., Dai, N., & Zhu, D. M. (2012). Laser induced modification and ablation of InAs nanowires. Journal of Applied Physics, 111(9), 094316.

[59] Pal, S., Aggarwal, R., Gupta, V. K., & Ingale, A. (2014). Time evolution studies of laser induced chemical changes in InAs nanowire using Raman spectroscopy. *Applied Physics Letters*, *105*(1), 012110.

[60] Schwartz, G. P., Schwartz, B., DiStefano, D., Gualtieri, G. J., & Griffiths, J. E. (1979). Raman scattering from anodic oxide-GaAs interfaces. *Applied Physics Letters*, *34*(3), 205-207.

[61] Campbell, I. H., & Fauchet, P. M. (1990). CW laser irradiation of GaAs: Arsenic formation and photoluminescence degradation. *Applied physics letters*, *57*(1), 10-12.

[62] Wiberg, E., Wiberg, N., & Holleman, A. F. *Inorganic Chemistry*; Academic Press: Berlin, 2001; p.742.

[63] H. S., & Jaeger, J. C. (1959). Conduction of heat in solids. *Oxford: Clarendon Press, 1959, 2nd ed.*

[64] Herman, I. P. (2011). Peak temperatures from Raman Stokes/anti-Stokes ratios during laser heating by a Gaussian beam. *Journal of Applied Physics*,*109*(1), 016103.

[65] Aspnes, D. E., Kelso, S. M., Logan, R. A., & Bhat, R. (1986). Optical properties of AlxGa1−x As. *Journal of applied physics*, *60*(2), 754-767.

[66] Palik, E. D. (1998). *Handbook of optical constants of solids* (Vol. 3). Academic press.

[67] Olson, G. L., & Roth, J. A. (1988). Kinetics of solid phase crystallization in amorphous silicon. *Materials Science Reports*, *3*(1), 1-77.

[68] Chang, C. C., Chen, H., Chen, C. C., Hung, W. H., Hsu, I. K., Theiss, J., ... & Cronin, S. B. (2011). Tailoring the crystal structure of individual silicon nanowires by polarized laser annealing. *Nanotechnology*, *22*(30), 305709.

[69] Bustarret, E., Hachicha, M. A., & Brunel, M. (1988). Experimental determination of the nanocrystalline volume fraction in silicon thin films from Raman spectroscopy. *Applied Physics Letters*, *52*(20), 1675-1677.

[70] Droz, C., Vallat-Sauvain, E., Bailat, J., Feitknecht, L., Meier, J., & Shah, A. (2004). Relationship between Raman crystallinity and open-circuit voltage in microcrystalline silicon solar cells. *Solar Energy Materials and Solar Cells,81*(1), 61-71.

[71] Viera, G., Huet, S., & Boufendi, L. (2001). Crystal size and temperature measurements in nanostructured silicon using Raman spectroscopy. *Journal of Applied Physics*, *90*(8), 4175-4183.

[72] Cao, L., Fan, P., Barnard, E. S., Brown, A. M., & Brongersma, M. L. (2010). Tuning the color of silicon nanostructures. *Nano letters*, *10*(7), 2649-2654.

[73] Hecht, E. (1998). Hecht optics. *Addison Wesley*, *997*, 213-214.

[74] Cargille Labs. http://www.cargille.com (accessed Dec. 12, 2012).

[75] Feng, C., Kajima, M., Gonda, S., Minoshima, K., Fujimoto, H., & Zeng, L. (2012). Accurate measurement of orthogonality of equal-period, two-dimensional gratings by an interferometric method. *Metrologia*, *49*(3), 236.

[76] Lochbihler, H. (2009). Colored images generated by metallic sub-wavelength gratings. *Optics express*, *17*(14), 12189-12196.

[77] Cheong, B. H., Prudnikov, O. N., Cho, E., Kim, H. S., Yu, J., Cho, Y. S., ... & Shin, S. T. (2009). High angular tolerant color filter using subwavelength grating. *Applied Physics Letters*, *94*(21), 3104.

[78] Lee, H. S., Yoon, Y. T., Lee, S. S., Kim, S. H., & Lee, K. D. (2007). Color filter based on a subwavelength patterned metal grating. *Optics express*, *15*(23), 15457-15463.

[79] Claes, T., Molera, J. G., De Vos, K., Schacht, E., Baets, R., & Bienstman, P. (2009). Label-free biosensing with a slot-waveguide-based ring resonator in silicon on insulator. *Photonics Journal, IEEE*, *1*(3), 197-204.

[80] Stewart, M. E., Anderton, C. R., Thompson, L. B., Maria, J., Gray, S. K., Rogers, J. A., & Nuzzo, R. G. (2008). Nanostructured plasmonic sensors.*Chemical reviews*, *108*(2), 494-521

[81] Homola, J., Yee, S. S., & Gauglitz, G. (1999). Surface plasmon resonance sensors: review. *Sensors and Actuators B: Chemical*, *54*(1), 3-15.